Czech Technical University in Prague
Faculty of Nuclear Science and Physical Engineering

DIPLOMA THESIS

EARLY PHYSICS AT LHC WITH THE DETECTOR ATLAS

Bc. Pavel Jež

Supervisor: Václav Vrba, CSc.

Acknowledgemets

I would like to thank my supervisor Václav Vrba for introducing me to CERN and ATLAS in particular without whome this thesis would never come into being. I am very grateful for all the support I got from him during this entire work. My big thanks belongs to whole ATLAS collaboration, but especially to my colleagues that I cooperated with on various parts of this thesis: I thank Marián Zdražil for giving the initial idea and starting the whole study of cosmic muons, Nathan Triplett for introducing me to the monitoring software, Michal Marčišovský for co-developing the simulation software and various computing and physical advices and Martin Zeman for his enthusiasm and big help with the final part of the study of cosmic muons.

The theoretic part of this thesis was greatly inspired by the lectures and discussions I attended at the Durham University and at European High-energy Physics Summer School in Třešť. I greatly benefited from it and used it a lot in this thesis. The part on data analysis was influenced by many sources, but the largest influence came from the b-tagging group in CPPM, Marseille.

I am also grateful to the Institute of Physics of the Academy of Sciences of the Czech Republic and especially to Jiří Popule for the material and organizational support during my whole work.

Last but not least, I would like to thank my family and friends for their patient support at all times.

This thesis was written with kind support of research programmes MŠMT VZ 3407391, 1P04LA212 and LA08032 by the Ministry of Education, Youth and Sports of the Czech Republic.

Declaration

I declare that I wrote my diploma thesis independently and exclusively with the use of cited bibliography.

Praha, 8.5.2008

Pavel Jež

Název práce:
První fáze fyzikálního výzkumu na LHC pomocí detektoru ATLAS

Autor: Bc. Pavel Jež

Obor: Matematické inženýrství

Druh práce: Diplomová práce

Vedoucí práce: Václav Vrba, CSc. Katedra fyziky, Fakulta jaderná a fyzikálně inženýrská, České vysoké učení technické v Praze

Abstrakt: V první kapitole je stručný přehled principů Standardního modelu, společně s několika teoriemi sahajícími za Standardní model. Druhá kapitola je zaměřena na otázky hledání Higgsova bosonu. Speciální pozornost je věnována metodice měření parametrů Higgsova bosonu a rozdílům Higgsova sektoru podle Standardního modelu a supersymetrických modelů. V třetí kapitole je popsán urychlovač LHC a plánované experimenty na něm. Podrobněji je zde popsán detektor ATLAS. Zbytek kapitoly je věnován výpočetnímu systému na ATLAS. Nacházejí se zde principy a užití offline softwarového prostředí Athena. Poslední část třetí kapitoly popisuje monitorovací software, který byl spoluvyvinut diplomantem. Čtvrtá kapitola pokrývá autorův vlastní výzkum: účinek kosmického záření na pixelový detektor. Ten je zkoumán pomocí kompletního softwarového řetězce. Nakonec je diskutovaná možnost kalibrace pixelového detektoru kosmickým zářením.

Klíčová slova: Standardní model, ATLAS, kosmické záření, pixelové detektory, Athena.

Title: **Early Physics at LHC with the detector ATLAS**

Author: Pavel Jež

Abstract: In the first chapter, there is a brief overview of the Standard Model together with several Beyond Standard Model theories. Second chapter is dedicated to the strategy of the search for the Higgs boson. Special attention is paid to the measurement of the Higgs properties and the differences between SM and supersymmetric Higgs. Third chapter describes experiments that operate at LHC accelerator. The ATLAS apparatus is described in more details. The rest of the chapter is devoted to the ATLAS computing. It includes description of the Athena - the ATLAS official software framework and also monitoring software co-developed by the author of the thesis. Fourth chapter covers author's own research activity: the effect of cosmic rays on the Pixel Detector using full Athena software chain. Finally, the possibility of calibration of the Pixel Detector by cosmic rays is discussed.

Key words: Standard Model, ATLAS, pixel detector, cosmic rays, Athena.

Contents

Chapter 1

Standard Model and Beyond

1.1 Success of the Standard Model

For about 40 years, our best theory for description of the behaviour of elementary particles has been the Standard Model. It is a renormalizable quantum field theory (QFT) with an internal symmetry group $SU(3) \otimes SU(2) \otimes U(1)$. Several beautiful books exist on this subject: construction of the quantum field theories and their renormalization are described in [1] or [2]. Electroweak part of the Standard Model is discussed in detail in [3], while the strong interactions are the subject of [4] and [5].

Standard Model (SM) incorporated all then-known particles and predicted several new: according to SM, elementary fermions come in three structurally identical families. Each of them contains two quarks and two leptons (for more details see Table 1.1). They interact via 12 intermediate vector (i.e. spin 1) bosons. Photon is responsible for electromagnetic interaction, $W^{\pm}$ and Z for the weak interaction, while eight gluons (each with different color charge) mediate strong interaction. For more details consult Table 1.2. Note that all above mentioned particles have been discovered and their properties are listed in [6].

According to the QFT (cf. [1], [2]), particles which we can see in the experiment are described by the excitations of quantum fields.

This fields transform under the SM internal symmetry in a straightforward way. Because the gauge group is a tensor product of three simple groups, we can act by each of them separately. Let D be an n-dimensional vector representation of the group $SU(3)$ or $SU(2)$ or $U(1)$ and let Φ be n-plet of quantum fields. Then the transformation looks like

$$\Phi'_i = D(g)_{ij}\Phi_j \ , \tag{1.1}$$

where we assume Einstein summation convention and g is the element of the group. Because all groups in tensor product $SU(3) \otimes SU(2) \otimes U(1)$ are Lie groups, we can rewrite matrix $D(G)$ from the previous equation in a more user friendly way:

$$D(g) = e^{i\Lambda_j T_j} \ , \tag{1.2}$$

where T_j are group generators and Λ_j are unambiguous parameters, i.e. each g has its own set of Λ's. Note that in case of abelian group $U(1)$, previous relations become much simpler as it has only one irreducible representation. It is one dimensional, so that $D(g)$ is just complex number on a unit circle and can be rewritten as $D(g) = e^{i\Lambda Y}$ where Y is (generally) arbitrary parameter, whose meaning will be described later.

The most peculiar thing about the Standard Model is that its particles are not in a single representation, but rather in 5 distinct representations of $SU(3) \otimes SU(2) \otimes U(1)$. The schematic picture is on Fig. 1.1. Left-handed up-type and down-type quarks form $SU(3)$ triplet and

		First generation	Second generation	Third generation	Electrical charge	Interaction
fermions	quarks	u-up	c-charm	t-top	+2/3	electromagnetic weak, strong
		d-down	s-strange	b-bottom	-1/3	
	leptons	e-electron	μ-muon	τ-tauon	-1	elmag., weak
		ν_e - e-neutrino	ν_μ - μ-neutrino	ν_τ - τ-neutrino	0	weak

Table 1.1: Elementary fermions.

	Interaction mediated	Name	Spin	Electrical charge	Mass	Count
bosons	electroweak	$W^{\pm}$	1	± 1	80.4 GeV	2
		Z	1	0	91.2 GeV	1
		γ	1	0	0	1
	strong	g	1	0	0	8
	Higgs	H	0	0	$\geq$ 114.4 GeV	1

Table 1.2: Elementary bosons. Masses from [6].

$SU(2)$ doublet, left-handed charged lepton and neutrino form $SU(3)$ singlet and $SU(2)$ doublet, right-handed up-type quarks form $SU(3)$ triplet and $SU(2)$ singlet, the same is true for down-type quarks. The fifth representation contains righthanded charged lepton and is $SU(3)$ and $SU(2)$ singlet. As the Fig. 1.1 suggests, all representations have also different hypercharges, i.e. transform properties under $U(1)$. The hypercharge assignment may seem somehow haphazard, but it gives correct electrical charges and, moreover, leaves the SM anomaly free[1].

From the organization of the multiplets we can clearly see how particles interact. For example, left-handed quarks interact via both strong interaction ($SU(3)$ triplet) and weak interaction ($SU(2)$ doublet), while right-handed quarks interact only strongly ($SU(2)$ singlets). We can also see that weak interaction violates parity (only left-handed particles interact weakly), which was discovered long before SM was formulated. Careful reader might have also noticed that there is no right-handed neutrino in the SM, implicating that neutrino is *exactly* massless. However 10 years ago, Super-Kamiokande discovered that this is not true [10]. There are several theoretical proposals, how to amend SM to accommodate neutrino mass that will be presented in subsequent sections.

So far we have seen that SM is a good way to classify elementary particles and predict very basic phenomenology. However, SM has also very rich dynamical content which can be formulated in an extremely economical way.

The general gauge transformation looks like (1.1). It can be viewed as a *global* gauge transformation, because it is identical in all space-time points. However, SM states that the gauge invariance is not global, but rather local, i.e. the transformation looks like (using (1.2) and dropping vector indices)

$$\Phi'(x) = e^{i\Lambda_j(x)T_j}\Phi(x) \tag{1.3}$$

---

[1] Anomaly is a failure of theory to restore the symmetry when the symmetry breaking parameter goes to zero. For example QED posses exact chiral symmetry (conservation of helicity) if we set mass of electron to be 0. In SM the anomaly is caused by triangular Feynman diagram (Fig. 1.2). If we want this anomaly to cancel identically, we obtain strict restriction on the hypercharges: only one of them can be chosen arbitrarily and others are then fixed [8, 9].

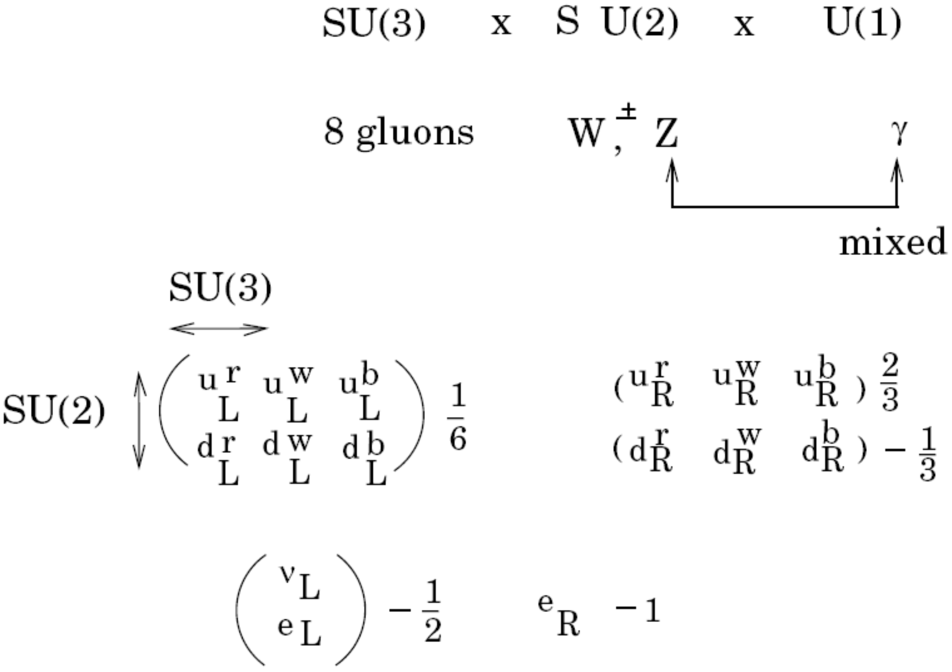

Figure 1.1: Scheme of the Standard Model. Picture shows 3 gauge groups of the SM together with respective gauge particles. It also shows 5 multiplets of the SM fermions together with their hypercharge. Arrows indicate in which direction the gauge groups $SU(2)$ and $SU(3)$ act. Figure taken from [7].

This simple principle has tremendous consequences. Suppose, we have Dirac Lagrangian

$$\mathscr{L}_0 = i\bar{\psi}\gamma^\mu\partial_\mu\psi - m\bar{\psi}\psi \; . \tag{1.4}$$

We immediately see, that it is has global $U(1)$ invariance because Dirac conjugate ($\overline{\psi} = \psi^\dagger\gamma_0$) transforms as

$$\overline{\psi}' = \overline{\psi}e^{-i\Lambda} \; . \tag{1.5}$$

However, when we demand that $\Lambda = \Lambda(x)$, the Lagrangian (1.4) loses the symmetry, because the differentiation of the composite function in the first term ("kinetic term") produces another term which was not in the original Lagrangian. In order to restore symmetry, we are forced to introduce a term whose transformation properties will cancel those of the kinetic term. In practice this means that we are introducing a new field (particle) A_μ which will transform like

$$A'_\mu(x) = A_\mu(x) + \frac{1}{g}\partial_\mu\Lambda(x) \; , \tag{1.6}$$

and the new term in Lagrangian will be $\mathscr{L}_{int} = g\bar{\psi}\gamma^\mu\psi A_\mu$ where g is arbitrary real number. It is straightforward to show that $\mathscr{L}_0 + \mathscr{L}_{int}$ is indeed local gauge invariant. From the mathematical point of view we have come from ordinary derivative to covariant derivative defined as

$$D_\mu = \partial_\mu - igA_\mu \; . \tag{1.7}$$

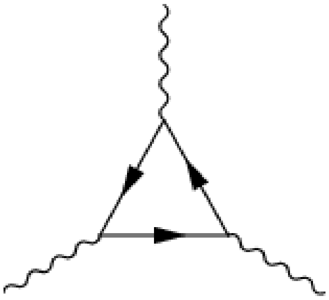

Figure 1.2: Feynman diagram of 3-point photon interaction via electron loop. By choosing hypercharges of SM appropriately the contribution from this diagram would be zero.

which in turn allows us to write new Lagrangian in a very aesthetically plausible way

$$\mathscr{L} = i\bar{\psi}\gamma^\mu D_\mu \psi - m\bar{\psi}\psi \ . \tag{1.8}$$

What is the physical meaning of the newly added term? It is nothing else than the interaction between electron, positron and photon: basic vertex of the QED. Therefore, local gauge invariance brings interaction to the static theory.

The same procedure (properly modified for non-abelian groups) is applied also to case of $SU(2)$ and $SU(3)$. Because of non-commutative nature of these two groups we obtain (apart from ordinary fermion-antifermion-boson vertex) also vector boson cubic and quartic self-interaction. Strangely enough, all of this vertices have been experimentally confirmed and no other have been seen[2].

However, our choice of representations of the SM gauge group have serious phenomenological problem: because of the different transformation properties of left- and right-handed fermions, we cannot have any mass terms ($\sim m(\overline{\psi}_R\psi_L + \overline{\psi}_L\psi_R)$) in the Lagrangian as they explicitly break the local gauge invariance. Also, we cannot have any gauge boson mass terms, because they spoil unitarity (i.e. if we introduce gauge boson mass terms, probability of particular process depends on when the process will take place).

From many solutions to this problem, spontaneous symmetry breaking (SSB) is by far the simplest way how to give masses to the elementary fermions and vector bosons. The basic idea is that first we add to the Lagrangian a term with scalar field which has all space-time and gauge symmetries of the theory.

Second, this term should have form of "Mexican hat potential", i.e. something like $\partial_\mu\phi\partial^\mu\phi^* - \mu^2\phi\phi^* + \lambda(\phi\phi^*)^2$, in case of complex scalar field. For $\lambda = 0$ we would get ordinary Klein-Gordon equation with reversed sign for the mass term. So let's suppose $\lambda > 0$. In this case, the potential is bounded from below and its ground state is infinitely degenerate (complex circle) and has a value of $\mu/\sqrt{2\lambda} = v/\sqrt{2}$. So that in ground state we have broken the original $U(1)$ symmetry of the Lagrangian. Next, we naturally factorize the original field

$$\phi(x) = \rho(x)\exp\left(i\frac{\pi(x)}{v}\right)$$

where both ρ and π are real fields. As a next step we can choose the minimum value ("vacuum expectation value") as a reference point and regard the original field as a small oscillations around this value:

$$\rho = v + \sigma$$

---

[2] One-loop corrections allow many other vertices, but these are highly suppressed.

If we put all this into the original Lagrangian we obtain something like

$$\mathscr{L} = \frac{1}{2}\partial_\mu \sigma \partial^\mu \sigma + \frac{1}{2}\partial_\mu \pi \partial^\mu \pi - \lambda v^2 \sigma^2 + \text{interaction terms} \tag{1.9}$$

where "interaction terms" are cubic or quartic in σ. Notice, that we obtained a mass term for field σ with mass $\sqrt{2\lambda}v$ and no mass term for field π, indicating it is unphysical. It can be shown that this is a general property of spontaneous symmetry breaking. For each broken continuous symmetry we obtain one massless boson (called Goldstone boson). Also, at least one massive scalar boson always survives this procedure (Higgs boson).

In case of SM, the original $SU(2) \otimes U(1)$ symmetry is spontaneously broken into $U(1)$ symmetry. So that we are breaking 3 continuous symmetries ($SU(2)$ has 3 generators) meaning we need to add at least 4 real scalar field, locally invariant under $SU(2) \otimes U(1)$. The easiest way to satisfy this is to introduce complex $SU(2)$ doublet Φ instead of one complex field in the previous example.

Next steps are the same: we factorize and shift the zero to the ground state value. However, because we still have $U(1)$ symmetry, we can choose the gauge in which the complex phase of our field is 1, so that we can get rid of the unphysical Goldstone bosons.

What remains is the mass term for the Higgs boson (as in previous case) but also other term which were not present before. Because all the derivatives in Lagrangian are covariant, Higgs boson automatically couples to the vector bosons and moreover, the same does the vacuum expectation value v. But terms of type v^2-boson-boson are just mass terms for the particular boson we were looking for. This also means that the Higgs-vector boson coupling is proportional to the mass of the vector boson.

Even more surprising is that if we rewrite the SSB Lagrangian in term of physical fields representing photon and weak intermediate bosons, we obtain only 3 mass terms for W's and Z and no mass term for photon.

The elementary fermions obtain masses by Yukawa mechanism. This means, that we add to the Lagrangian terms where complex Higgs doublet couples to doublet of left-handed fermions L and to one right-handed fermion:

$$\mathscr{L}_{Yukawa} = -h_e \bar{L} \Phi e_R - h_e \overline{\bar{L} \Phi e_R} \tag{1.10}$$

Such a combination is singlet under all gauge groups.

Then we do the same as in the previous case, so that complex doublet turns into field of form $\binom{0}{v+\sigma}$. When we work out the matrix multiplication, we obtain fermion mass terms and also fermion-Higgs interaction. Important thing is that the coupling constants of this interactions are proportional to the respective fermion masses.

Because SSB is able to give masses to all elementary particles, it is integral part of the SM. However, because the Higgs boson has not been discovered yet, we cannot tell if SSB exists in reality[3].

Previous paragraphs showed the core of the SM, which is remarkably simple and *principled*. Standard Model is a renormalizable quantum field theory with local $SU(3) \otimes SU(2) \otimes U(1)$ gauge invariance. This symmetry is spontaneously broken, giving rise to particle masses. This means that the SM predictions are unambiguous and that (in general) cannot be modified "a bit" to fit the results. Some tests of the electroweak sector of the SM are summarized in Table 1.3. We can see the remarkable agreement of the theory and experiment.

The same is true also for the strong sector of the SM: Quantum Chromodynamics (QCD). The basic parameter of the strong interaction is the strong coupling constant. Its measurements

---

[3] In the next sections we will see that even if we would have found Higgs boson, it would not be enough to prove SSB.

	Measurement with Total Error	Systematic Error	Standard Model Fit	Pull
m_Z[GeV]	91.1975 ± 0.0021	0.0017	91.1875	0.0
Γ_Z[GeV]	2.4952 ± 0.023	0.0012	2.4957	-0.2
m_W[GeV]	80.392 ± 0.029	N/A	80.372	0.7
Γ_W[GeV]	2.147 ± 0.060	N/A	2.091	0.9
m_t[GeV]	171.4 ± 2.1	1.8	171.7	-0.2

Table 1.3: Several results from electroweak sector of the SM obtained at LEP and Tevatron. Total errors (column 2) include systematic errors (column 3). Pull is difference between measurement and fit in units of the total measurement error. Numbers from [11].

are summarized in the Figure 1.3. Each point in the plot is result of hundreds of independent measurements, with different techniques and particles, yet the agreement with the theory is astonishing. Figure 1.3 shows also other remarkable fact: the coupling constant is ”running”, i.e. the strength of interaction depends on its energy scale. This property of QCD is called asymptotic freedom and allows SM to be extrapolated far beyond the energies of the current accelerators.

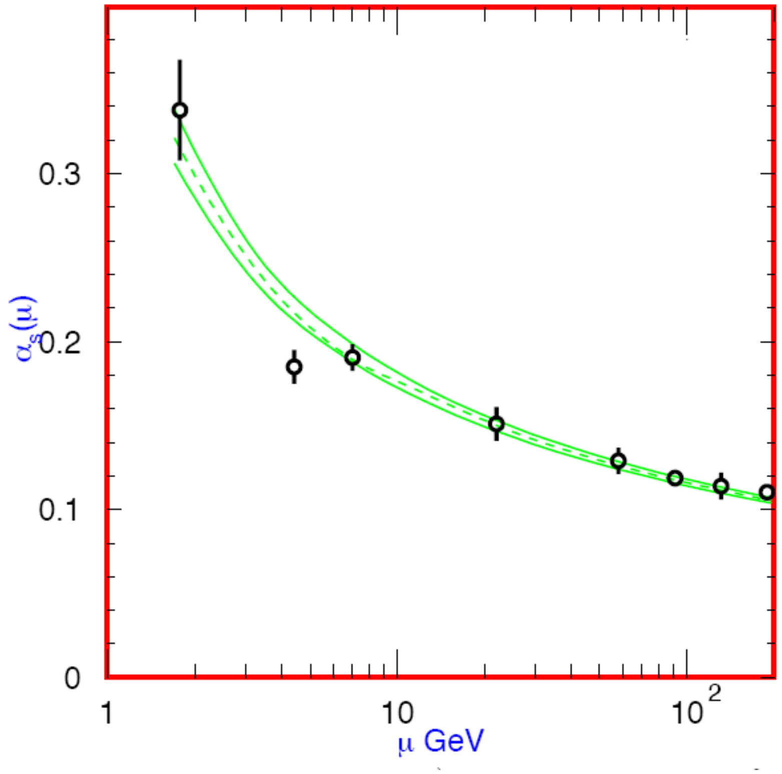

Figure 1.3: Summary of the values of strong coupling $\alpha_S(\mu)$. Dashed line is the theoretical value (note the decrease with μ), solid lines are 1 σ uncertainty. Circles with error bars are experimental results. Figure from [6].

1.2 Towards GUT

Previous section showed that the Standard Model provides economic packaging for all particle phenomenology we have observed on accelerators. It is a mature theory, coming from several basic principles and as a result its predictions are precise and unambiguous. The SM has also withstood all the experimental tests with extraordinary success. All this means that the SM is a good theory and will be used as a effective theory for low energies even after some of the theories Beyond the Standard Model (BSM) will be proven experimentally.

However, we have also seen that there are several disturbing things about the SM. The first of them are very peculiar representations of the gauge group. Why there are five different multiplets? Is it possible to have all particles of the SM in one (or two at most) representation of the gauge group? Answer is yes and the theories which have all particles in one or two representations are called Grand Unification Theories (GUTs).

First thing we have to do when constructing a GUT is to find some suitable gauge group. The requirements are quite obvious: it should in some way contain $SU(3) \otimes SU(2) \otimes U(1)$, it should be simple (to allow irreducible representations made from all particles) and it should be as small as possible. Given these demands, group theory gives us the answer: group $SU(5)$.

Or we can take another approach. In SM we have 3 strong colors (R,W,B) and 2 weak "colors" (G,P). So that if we want unified theory which contains SM, it must have 5 colors, so that we are again coming to the $SU(5)$.

Nevertheless, the most important question is if there is some representation (or representations) of $SU(5)$ which can accommodate *all* Standard Model fermions. This questions was studied long before by Georgi and Glashow [12] and they found that all SM fermions could be organized in two representations of $SU(5)$. The schematic picture is on Fig. 1.4. The first is 10-dimensional antisymmetric 5×5 tensor representation. It contains particles which can be labeled by all possible combinations of different colors. Second representation is 5 dimensional and contains all anticolors.

The most interesting thing is, that if we introduce hypercharge by equation

$$Y = -\frac{1}{3}(R + W + B) + \frac{1}{2}(G + P) \ .$$

we obtain exactly the same hypercharge assignment as in the SM. The fact that whole SM structure is reproduced by a simple set of rules for manipulating symmetrical symbols is really astonishing [7].

So we have seen that $SU(5)$ GUT can serve as a nice classification of SM particles. Another thing are the dynamical consequences of such a theory. Following the same way as in the case of the SM we find that there must be some unified coupling for the unified $SU(5)$ interaction. However, measurements show that the strong, weak and electroweak couplings are rather different at the accessible energies. This means that if there is GUT, it is spontaneously broken at some high, unaccessible scale, and we can see only remnants of this symmetry.

Nevertheless, as we have seen in the previous section, the couplings run with the energy scale. So that if the couplings are unified at some energy scale and from there on they evolve independently, the strong coupling will rise, while the other two will decrease, resulting in a pattern we can see on our accelerators. Figure 1.5 show the evolution of coupling constants together with error bands based on precision measurements and calculations. We can see that the couplings very approximately unify at the scale of 10^{15} GeV. This is the difference to the original calculation of Georgi, Quinn, and Weinberg [13] who supposed that these couplings unify exactly.

Consequently since baryons and leptons are contained in the same multiplet, the theory explicitly violates the conservation of lepton and baryon number, ultimately leading to prediction

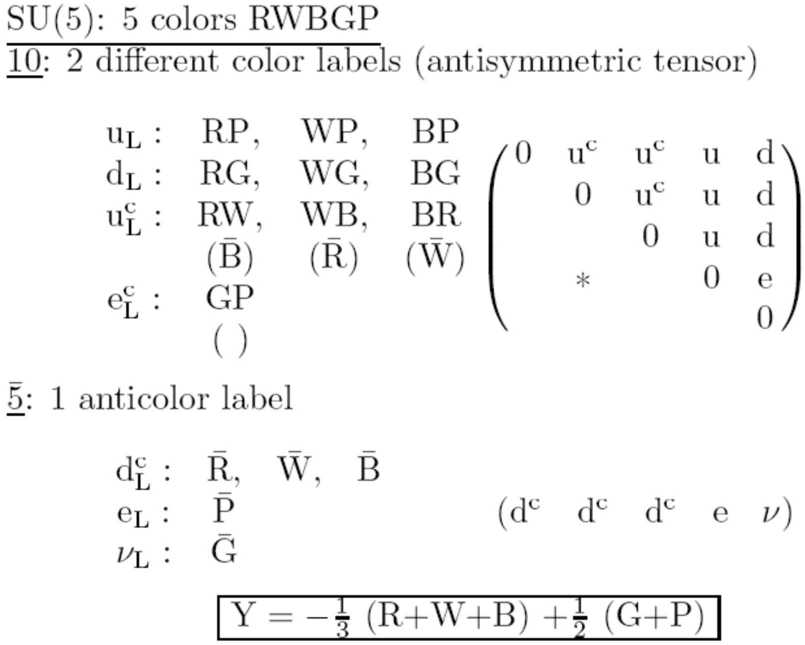

SU(5): 5 colors RWBGP

<u>10</u>: 2 different color labels (antisymmetric tensor)

$$\begin{array}{llll} \mathrm{u_L}: & \mathrm{RP}, & \mathrm{WP}, & \mathrm{BP} \\ \mathrm{d_L}: & \mathrm{RG}, & \mathrm{WG}, & \mathrm{BG} \\ \mathrm{u^c_L}: & \mathrm{RW}, & \mathrm{WB}, & \mathrm{BR} \\ & (\bar{\mathrm{B}}) & (\bar{\mathrm{R}}) & (\bar{\mathrm{W}}) \\ \mathrm{e^c_L}: & \mathrm{GP} & & \\ & (\ ) & & \end{array} \quad \begin{pmatrix} 0 & \mathrm{u^c} & \mathrm{u^c} & \mathrm{u} & \mathrm{d} \\ & 0 & \mathrm{u^c} & \mathrm{u} & \mathrm{d} \\ & & 0 & \mathrm{u} & \mathrm{d} \\ & * & & 0 & \mathrm{e} \\ & & & & 0 \end{pmatrix}$$

<u>$\bar{5}$</u>: 1 anticolor label

$$\begin{array}{llll} \mathrm{d^c_L}: & \bar{\mathrm{R}}, & \bar{\mathrm{W}}, & \bar{\mathrm{B}} \\ \mathrm{e_L}: & \bar{\mathrm{P}} & & \\ \nu_{\mathrm{L}}: & \bar{\mathrm{G}} & & \end{array} \quad (\mathrm{d^c} \quad \mathrm{d^c} \quad \mathrm{d^c} \quad \mathrm{e} \quad \nu)$$

$$\boxed{\mathrm{Y} = -\tfrac{1}{3}\ (\mathrm{R+W+B}) + \tfrac{1}{2}\ (\mathrm{G+P})}$$

Figure 1.4: Organization of SM fermions into two representations of $SU(5)$. We are using ordinary three colours of SM (red, white, blue) and two weak "colors": purple and green. Hypercharge may be calculated using the formula in the box. Figure from [7].

of proton decay. On the other hand, the interaction between leptons and baryons is mediated by particles with mass in the order of the GUT breaking (analogically - weak interaction is mediated by particles with mass in the order of electroweak (EW) symmetry breaking). And because decay rate goes as the fourth inverse power of mass of the intermediate boson, the proton decay is highly suppressed.

However, also at this point precision tests showed problem of $SU(5)$ GUT . Calculation reveals that proton lifetime should in the order of 10^{31} years. This value has been already experimentally excluded by 2 orders of magnitude [6].

Another problem of this minimal GUT is so-called hierarchy problem. It puts forward why the ratio of GUT and EW symmetry-breaking scale is so small (10^{-13}), and whether it is stable.

With all this problems, it seems that minimal GUT is doomed, however, it can be saved by low-energy Supersymmetry (SUSY - see next section). Indeed, if we introduce SUSY, all the couplings unify at the unification scale which is somewhat larger (O(10^{16} GeV), see Fig. 1.5), meaning that also the predicted proton lifetime is larger and in accord with experiment. Last, low-energy SUSY also addresses hierarchy problem by canceling quadratic divergences in the Higgs potential.

One last thing to say is that this is certainly not the only possible GUT. There is very nice extension which takes as its gauge group only a bit larger group $SO(10)$. It has two advantages: all particles can be in one 16-dimensional representation and it accommodates right-handed neutrino, as the 16th particle.

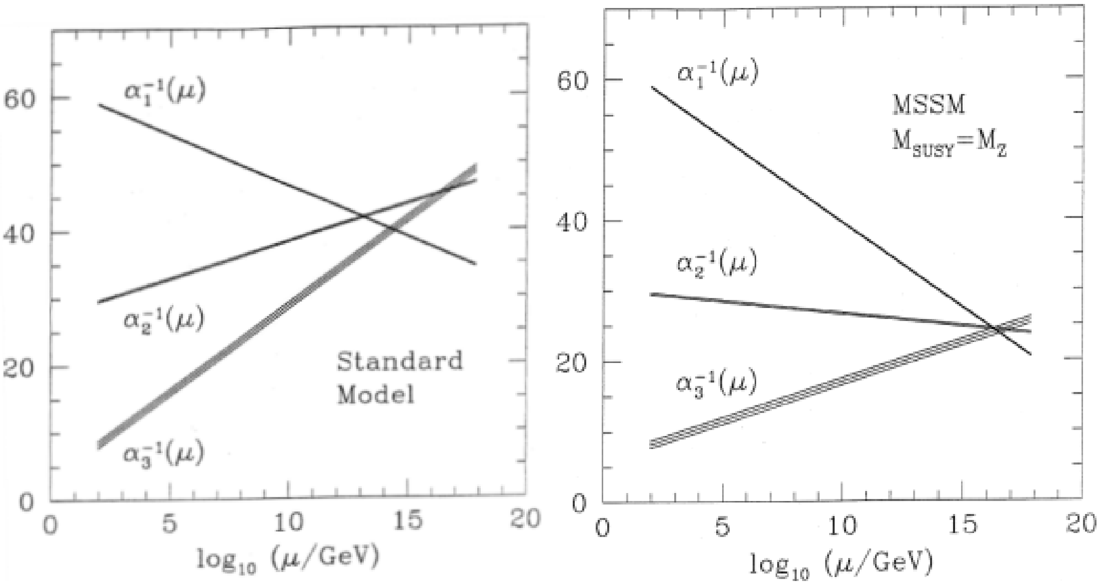

(a) Standard GUT

(b) SUSY GUT

Figure 1.5: Running of the SM coupling constants with the energy. Note the logarithmic scale for the energies. Thickness of lines reflects the uncertainty for given parameter. Plot (a) is for standard GUT calculation, plot (b) shows the same with the addition of SUSY. Note higher unification scale in case (b). Figures from [7].

1.3 Supersymmetry

1.3.1 Introduction

Last section showed that Supersymmetry can be the savior of the minimal GUT. However, that was not its original purpose. In the beginning the SUSY was invented to prevent quadratic divergence in the Higgs self-potential. So that the following section will present a brief introduction to SUSY based on lectures of Georg Weiglein at Durham University [14] and on [15].

Consider at first photon self-energy (Fig. 1.6). The contribution to the 2-point function from this diagram is divergent (as all one-loop diagrams in QED). However, after doing a dimensional regularization, the contribution vanishes identically. The reason is *exact* $U(1)$ gauge symmetry which "protects" the mass of the photon - it is massless in all orders of perturbation theory.

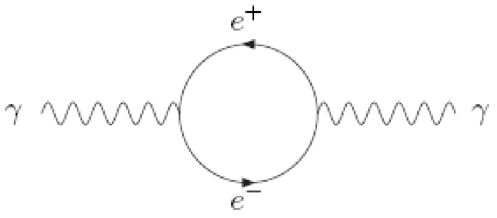

Figure 1.6: Feynman diagram for photon self-energy. Figure from [15].

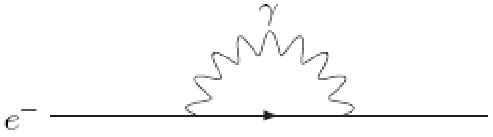

Figure 1.7: Feynman diagram for electron self-energy. Figure from [15].

Slightly different situation is in case of electron self-energy (Fig. 1.7). This diagram is also quadratically divergent, and unlike the previous case, the divergence is not canceled by renormalization. It is rather replaced by logarithmic divergence resulting in the correction which is proportional to the electron mass. This can be understood in terms of approximate chiral symmetry - it is exact only for massless particle - and indeed, adjusting electron mass to zero will cancel the contribution from diagram 1.7.

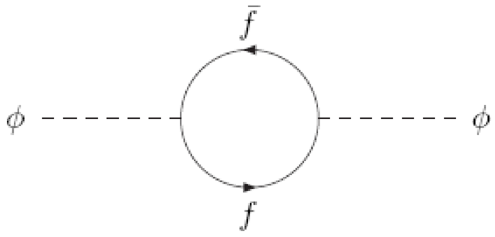

Figure 1.8: Fermion and antifermion contribution to Higgs self-energy. Figure from [15].

But for the Higgs boson (Fig. 1.8) the situation is much worse. In this case there is no symmetry (exact or approximate) to protect it, so the divergence remains quadratic, leading to corrections which are about 30 orders of magnitude larger than the Higgs mass. This is very disturbing because it would require very fine tuning to cancel the inevitably large bare mass against the large loop corrections to obtain (comparatively) very small Higgs mass. Moreover, this fine tuning would have to be different in every order of perturbation theory.

Because it would be very difficult to find some plausible explanation of the origin of this fine tuning, another solution was proposed - addition of the new symmetry which will protect Higgs mass as it does in case of photons and electrons. This new symmetry was called Supersymmetry and it is the symmetry between fermions and bosons. Indeed, if we suppose that SUSY is exact, the contributions from bosons to the Higgs self-energy cancel these of fermions so that the divergence vanishes identically.

However, we know that the Supersymmetry is not exact, because there are no sparticles (SUSY partners of ordinary particles) in the currently reachable energies. So the SUSY must be somehow broken at an energy scale which is larger than the current experimental reach. There is no reason that this breaking scale should be anywhere close to actual energy frontier, but if the SUSY SSB occurs too much high above electroweak scale, than we again have the problem with Higgs self-energy. So if we want SUSY to address Higgs quadratic divergences, the breaking must not occur at higher scales than $O(1\text{ TeV})$.

How to accommodate this new symmetry in our theory? All space-time symmetries are contained in the Poincare group. Ten generators of space-time symmetries form Poincare algebra which is defined by commutation relations between them. The natural approach would be to find generators of SUSY and define commutators with other space-time symmetries. However, Coleman-Mandula theorem [16] states that it is impossible to add to Poincare algebra a new symmetry in any but trivial way. This is the case of SM which has, in addition to space-time symmetries, also a gauge symmetry, which commutes with all space-time symmetries, so that the resulting symmetry group is a tensor product of the Poincare group and a gauge group.

Therefore, we have to use anticommutators if we want to add SUSY generators to our existing symmetries. Because SUSY generators connect fermionic and bosonic states, they themselves have fermionic character, which is in good accord with the previously announced use of anticommutators.

There can be many SUSY generators, but this mostly brings only technical complications, so in the following we will stick to just one generator Q and its conjugate $\overline{Q}$. Note that because of fermionic character these operators are 2-component Weyl spinors. Now we can set the anticommutators which define the superalgebra:

$$\{Q_\alpha, Q_\beta\} = \{\overline{Q}_{\dot\alpha}, \overline{Q}_{\dot\beta}\} = 0 \qquad \{Q_\alpha, \overline{Q}_{\dot\beta}\} = 2\sigma^{\mu}_{\alpha\dot\beta} P_\mu$$

Spinor indices are denoted α and β, dotted in the case of spinor conjugate. They can take values 1 or 2. P_μ is momentum generator, σ^0 is identity matrix and σ^i are Pauli matrices. The commutator $[Q_\alpha, P_\mu]$ is zero, as previously stated.

Now, that we have SUSY algebra, we would like to know how does a SUSY transformation look like. It is convenient to introduce new space-time coordinates on which SUSY will act. It will be fermionic Grassmann (anticommuting) variables θ and $\overline{\theta}$. The anticommutativity means this:

$$\{\theta,\theta\} = \{\overline{\theta},\theta\} = \{\overline{\theta},\overline{\theta}\} = 0$$

Variables, dependent on this anticommuting coordinates, as well as on the normal space-time coordinates, are called superfields. Note, that because each θ has 2 degrees of freedom, we have effectively doubled the dimensions of space-time.

Then, in accord with our previous experience with the symmetry generators, we can write a SUSY transformation matrix as

$$S(y,\xi,\overline{\xi}) = \exp[i(\xi Q + \overline{Q\xi} - y_\mu P^\mu)]$$

Obviously, S is an element of a group corresponding to the SUSY algebra. Let's multiply two elements of this group to find the explicit form of SUSY action:

$$S(0,\xi,\overline{\xi})G(x^\mu,\theta,\overline{\theta}) = G(x^\mu + i\theta\sigma^\mu\overline{\xi} - i\xi\sigma^\mu\overline{\theta}, \theta+\xi, \overline{\theta}+\overline{\xi}) \tag{1.11}$$

We have used Hausdorff's formula $e^A e^B = e^{A+B+\frac{1}{2}[A,B]+\cdots}$ and the fact, that SUSY algebra can be rewritten in terms of commutators, when we use also Grassmann variables:

$$[\theta Q, \overline{\theta Q}] = 2\theta\sigma^\mu\overline{\theta}P_\mu$$

All other commutators are zero. Notice also, that in this case the Hausdorff's formula is exact, because all terms with product of three and more θ's vanish. The group multiplication (1.11) induces following action on the parameter space:

$$g(\xi,\overline{\xi}) : (x^\mu,\theta,\overline{\theta}) \to (x^\mu + i\theta\sigma^\mu\overline{\xi} - i\xi\sigma^\mu\overline{\theta}, \theta+\xi, \overline{\theta}+\overline{\xi})$$

This now allows us to write infinitesimal SUSY transformation

$$\delta_S(0,\xi,\overline{\xi})\Phi(x^\mu,\theta,\overline{\theta}) = \left[\xi\frac{\partial}{\partial\theta} + \overline{\xi}\frac{\partial}{\partial\overline{\theta}} - i(\xi\sigma_\mu\overline{\theta} - \theta\sigma_\mu\overline{\xi})\frac{\partial}{\partial x_\mu}\right]\Phi(x^\mu,\theta,\overline{\theta})$$

Now we can immediately write explicit representation of the SUSY operators, which will allow us to find SUSY invariant action useful in construction of SUSY Lagrangian.

$$Q_\alpha = \frac{\partial}{\partial\theta^\alpha} - i\sigma^\mu_{\alpha\dot{\beta}}\overline{\theta}^{\dot{\beta}}\partial_\mu\ ; \qquad \overline{Q}_{\dot{\alpha}} = -\frac{\partial}{\partial\overline{\theta}^{\dot{\alpha}}} + i\theta^\beta\sigma^\mu_{\beta\dot{\alpha}}\partial_\mu$$

We can see that they contain "translation" in SUSY space together with part coming from the anticommutativity. We can also observe, that this operators mix with the ordinary space-time derivatives, so it is convenient to introduce SUSY-covariant derivatives which commute with SUSY transformations and are therefore SUSY invariant:

$$D_\alpha = \frac{\partial}{\partial\theta^\alpha} + i\sigma^\mu_{\alpha\dot{\beta}}\overline{\theta}^{\dot{\beta}}\partial_\mu\ ; \qquad \overline{D}_{\dot{\alpha}} = -\frac{\partial}{\partial\overline{\theta}^{\dot{\alpha}}} - i\theta^\beta\sigma^\mu_{\beta\dot{\alpha}}\partial_\mu$$

1.3.2 Chiral superfields

Construction of SM showed us the importance of the appropriate choice of representation. The same is true in this case. For further study of SUSY it is better to use chiral representations which treat Grassmann variables on different footing. So we get L-representation:

$$\delta_S \Phi_L = \left(\xi \frac{\partial}{\partial \theta} + \bar{\xi} \frac{\partial}{\partial \bar{\theta}} + 2i\theta\sigma^\mu \bar{\xi} \partial_\mu \right) \Phi_L \; ; \qquad D_L = \frac{\partial}{\partial \theta} + 2i\sigma^\mu \bar{\theta} \partial_\mu \; ; \qquad \overline{D}_L = -\frac{\partial}{\partial \bar{\theta}} \; , \tag{1.12}$$

and R-representation:

$$\delta_S \Phi_R = \left(\xi \frac{\partial}{\partial \theta} + \bar{\xi} \frac{\partial}{\partial \bar{\theta}} - 2i\xi\sigma^\mu \bar{\theta} \partial_\mu \right) \Phi_R \; ; \qquad \overline{D}_R = -\frac{\partial}{\partial \bar{\theta}} - 2i\theta\sigma^\mu \partial_\mu \; ; \qquad D_R = \frac{\partial}{\partial \theta} \; . \tag{1.13}$$

Finally, we need irreducible representations. The simplest way to achieve this is to demand

$$\overline{D}\Phi_L = 0 \qquad \text{and} \qquad D\Phi_R = 0 \; .$$

Comparing with (1.12) and (1.13), we find that in the first case the field is independent of $\bar{\theta}$ while in the second case is independent of θ. This allows us to write an expansion of the superfields in terms of Grassmann variables:

$$\Phi_L(x, \theta) = \phi(x) + \sqrt{2}\theta^\alpha \psi_\alpha(x) + \theta^\alpha \theta^\beta \varepsilon_{\alpha\beta} F(x) \; . \tag{1.14}$$

This expansion is exact, because any combination of more than 2 θ's is automatically zero because in this case there must be two same components and so $\theta^\alpha\theta^\alpha = \theta^\beta\theta^\beta = 0$ as a simple consequence of anticommutativity. Fields ϕ and F are scalars, while ψ is spinor. So we can see the first sign of SUSY: bosonic and fermionic fields are combined in one representation. On the other hand we have 4 bosonic and only 2 fermionic degrees of freedom, but it will be shown that not all of them are physical, so the symmetry between fermions and bosons is exact.

Now it is time to look how the field (1.14) transforms under infinitesimal SUSY (1.12):

$$\begin{aligned} \delta_S \Phi_L &= \sqrt{2}\xi^\alpha \psi_\alpha(x) + 2\xi^\alpha \theta^\beta \varepsilon_{\alpha\beta} F(x) \\ &\quad + 2i\theta^\alpha \sigma^\mu_{\alpha\dot{\beta}} \bar{\xi}^{\dot{\beta}} \partial_\mu \phi(x) + 2\sqrt{2} i \theta^\alpha \sigma^\mu_{\alpha\dot{\beta}} \bar{\xi}^{\dot{\beta}} \theta^\beta \partial_\mu \psi_\beta + 2i\theta^\alpha \sigma^\mu_{\alpha\dot{\beta}} \bar{\xi}^{\dot{\beta}} \theta^\alpha \theta^\beta \varepsilon_{\alpha\beta} F(x) \\ &\equiv \delta_S \phi + \sqrt{2}\theta \delta_S \psi + \theta\theta \delta_S F \; . \end{aligned} \tag{1.15}$$

The last term on the second line is zero, because of three θ's and on the last line I dropped spinor indices and introduced SUSY "dot product": $\theta\theta = \varepsilon_{\alpha\beta}\theta^\alpha\theta^\beta$. We can see that SUSY transformation of L-chiral superfield is again L-chiral superfield.

Finally, let's examine the form of the component fields after the transform:

$$\delta_S \phi = \sqrt{2}\xi\psi \tag{1.16}$$

$$\delta_S \psi = \sqrt{2}\xi F + i\sqrt{2}\sigma^\mu \bar{\xi} \partial_\phi \tag{1.17}$$

$$\delta_S F = -i\sqrt{2}\partial_\mu(\psi\sigma^\mu\bar{\xi}) \tag{1.18}$$

This means that boson field is transformed to fermion field, fermion is transformed to boson and the field F is transformed to total derivative. Now we have shown that SUSY works in the way we wanted it to. Extremely important is the equation (1.18), because it shows how we should construct SUSY invariant Lagrangian: the addition of total derivatives does not change the action.

1.3.3 Vector Superfields

So far we have found representation for scalars (spin-0 bosons, e.g. Higgs) and spin-1/2 fermions (e.g. leptons and quarks). However, SM contains also spin-1 vector bosons: these are all gauge bosons. So that we must find some representation for them.

For that reason we will introduce another irreducible representation of SUSY algebra: Vector superfields. The condition is

$$V(x,\theta,\overline{\theta}) = V^{\dagger}(x,\theta,\overline{\theta}) \ .$$

This means that vector superfields are self-conjugate. The general form of this field is a bit lengthy, but it is instructive to show it.

$$\begin{aligned} V(x,\theta,\overline{\theta}) &= C(x) + i\theta\chi(x) - i\overline{\theta}\overline{\chi}(x) + \frac{i}{2}\theta\theta\left[M(x) + iN(x)\right] - \frac{i}{2}\overline{\theta}\overline{\theta}\left[M(x) - iN(x)\right] \\ &- \theta\sigma^{\mu}\overline{\theta}A_{\mu}(x) + i\theta\theta\overline{\theta}\left[\overline{\lambda}(x) - \frac{i}{2}\overline{\sigma}^{\mu}\partial_{\mu}\chi(x)\right] - i\overline{\theta}\overline{\theta}\theta\left[\lambda(x) + \frac{i}{2}\sigma^{\mu}\partial_{\mu}\overline{\chi}(x)\right] \\ &+ \frac{1}{2}\theta\theta\overline{\theta}\overline{\theta}\left[D(x) + \frac{1}{2}\Box C(x)\right] \end{aligned} \tag{1.19}$$

In this case, fields C, M, N, and D are real scalars (spin-0 bosons), χ and λ are Weyl spinors (spin-1/2 fermions) and field A^{μ} is a spin-1 vector field. This is of course not the only possible choice of coefficients in the θ,$\overline{\theta}$ expansion. This one was inspired by the hermitian field which was constructed from chiral fields (1.14). Because in vector superfields there are both θ and $\overline{\theta}$ it is good to write L-chiral field in R-representation and vice versa. For that we can use simple trick allowing transition between representations:

$$\Phi(x_{\mu},\theta,\overline{\theta}) = \Phi_L(x_{\mu} + i\theta\sigma_{\mu}\overline{\theta},\theta,\overline{\theta}) = \Phi_R(x_{\mu} - i\theta\sigma_{\mu}\overline{\theta},\theta,\overline{\theta}) \ .$$

So that the L-chiral field (1.14) in R-representation is:

$$\begin{aligned} \Phi &= \phi(x) + i\theta\sigma^{\mu}\overline{\theta}\partial_{\mu}\phi(x) + \frac{1}{4}\theta\theta\overline{\theta}\overline{\theta}\Box\phi(x) \\ &+ \sqrt{2}\theta\psi(x) - \frac{i}{\sqrt{2}}\theta\theta\partial_{\mu}\psi(x)\sigma^{\mu}\overline{\theta} + \theta\theta F(x) \ . \end{aligned} \tag{1.20}$$

When working out this expression, Taylor expansion in x^{μ} and also spinor algebra is used (for more details see [17]). Now we can write hermitian field which can be constructed by adding a chiral field and its conjugate

$$\begin{aligned} \Phi + \Phi^{\dagger} &= \phi + \phi^* + \sqrt{2}(\theta\psi + \overline{\theta}\overline{\psi}) + \theta\theta F + \overline{\theta}\overline{\theta}F^* + i\theta\sigma^{\mu}\overline{\theta}\partial_{\mu}(\phi - \phi^*) \\ &+ \frac{i}{\sqrt{2}}\theta\theta\overline{\theta}\sigma^{\mu}\partial_{\mu}\psi + \frac{i}{\sqrt{2}}\overline{\theta}\overline{\theta}\theta\sigma^{\mu}\partial_{\mu}\overline{\psi} + \frac{1}{4}\theta\theta\overline{\theta}\overline{\theta}\Box(\phi + \phi^*) \ . \end{aligned} \tag{1.21}$$

In the case of vector field (1.19) the vector boson field A^{μ} is the coefficient of $\theta\sigma^{\mu}\overline{\theta}$. In hermitian field $\Phi + \Phi^{\dagger}$ the coefficient standing at this combination is $i\partial_{\mu}(\phi - \phi^*)$, i.e. gradient of a real scalar, something very similar to the gauge transformation in the ordinary $U(1)$ gauge theory. So that let's define SUSY generalization of a gauge transformation:

$$V \to V + \Phi + \Phi^*$$

Under this transformation the bosonic and fermionic fields do

$$\begin{aligned} C &\to C + \phi + \phi^* \\ \chi &\to \chi - i\sqrt{2}\psi \\ M + iN &\to M + iN - 2iF \\ A_\mu &\to A_\mu - i\partial_\mu(\phi - \phi^*) \\ \lambda &\to \lambda \\ D &\to D \end{aligned}$$

We observe, that λ and D are gauge invariant - this will be important in constructing Lagrangian. Next, remembering that a chiral superfield has 4 bosonic and 2 fermionic degrees of freedom, we can choose the gauge (i.e. the transforming chiral superfield) in such a way that C, χ, M and N are identically zero and still has one "ordinary" gauge degree of freedom remaining. This gauge is called Wess-Zumino (WZ) gauge.

Applying WZ gauge greatly simplifies the form of vector superfield, making it easier to calculate infinitesimal SUSY transformation. Nevertheless, the calculation and results are still not particularly enlightening, so I will only quote one important conclusion: as in the case of chiral superfield, the coefficient at $\theta\theta\overline{\theta}\overline{\theta}$ (i.e. the largest number of θ's) transform itself into total derivative, making itself useful in constructing Lagrangian.

1.3.4 SUSY Lagrangian

If we want to turn SUSY into a regular theory, we must construct its Lagrangian. The natural demand is the invariance of the action under all symmetries, including SUSY. The space-time invariance is already solved, so our demand on the Lagrangian is

$$\delta_S \int \mathrm{d}^4 x \mathscr{L}(x) = 0 ,$$

where δ_S is infinitesimal SUSY transformation. In the previous sections we discovered that this is the property of F-terms in chiral superfields and D-terms in vector superfields. Because they both are the coefficients standing at the highest number of θ's ($\theta\theta$ and $\theta\theta\overline{\theta}\overline{\theta}$, respectively), we can write the action as

$$S = \int \mathrm{d}^4 \left(\int \mathrm{d}^2\theta \mathscr{L}_F + \int \mathrm{d}^2\theta \mathrm{d}^2\overline{\theta} \mathscr{L}_D \right) .$$

The integration over Grassmann variables ensures that only coefficients of $\theta\theta$ and $\theta\theta\overline{\theta}\overline{\theta}$ survive and all other vanish. For details about the integration of Grassmann variables see for example [18] or any other QFT textbook.

Our basic blocks are chiral and vector superfields. What can we construct from them? First notice, that if Φ_1 and Φ_2 are chiral superfields, $\Phi_1\Phi_2$ is also a superfield of the same chirality. So we can construct new terms as a product of chiral superfields. Let's have a look on the F-term of the product of the two superfields (I am skipping all other terms, as they will vanish in integration):

$$\Phi_1\Phi_2 \mid_{\theta\theta} = \phi_1 F_2 + \phi_2 F_1 - \psi_1\psi_2 . \tag{1.22}$$

Now we can start to see some physics in SUSY: the last term in previous equation looks like the fermion mass term. We can also make a product of three chiral superfields:

$$\Phi_1\Phi_2\Phi_3 \mid_{\theta\theta} = \phi_1\phi_2 F_3 + \phi_1 F_2 \phi_3 + \phi_1\phi_2 F_3 - \psi_1\phi_2\psi_3 - \phi_1\psi_2\psi_3 - \psi_1\psi_2\phi_3 . \tag{1.23}$$

It is easy to see that the last three terms are in fact scalar-fermion-fermion interaction. Now we would like to continue in this fashion, but it would not do any good, because in product of 4 superfields we would get terms with the mass dimension higher than 4 and then the Lagrangian would lose its renormalizability.

Instead, we can construct something else: product of chiral superfield and its conjugate. In this case the result would not be chiral but a vector superfield. We need L-chiral field in R-representation (eq. (1.20)). Making product of this expression with its conjugate we can easily check, that the D-term is

$$\Phi\Phi^\dagger\mid_{\theta\theta\overline{\theta\theta}} = FF^* - \phi\Box\phi^* - i\overline{\psi}\sigma_\mu\partial^\mu\psi \ . \tag{1.24}$$

Here we can clearly identify the kinetic term for both scalar and fermionic component. We can also see, that there is no kinetic term for F, indicating it can be integrated out.

First step in the process of getting rid of F is to define a superpotential f:

$$f(\Phi_i) = \sum_i k_i\Phi_i + \frac{1}{2}\sum_{i,j} m_{ij}\Phi_i\Phi_j + \frac{1}{3}\sum_{i,j,k} g_{i,j,k}\Phi_i\Phi_j\Phi_k \ . \tag{1.25}$$

Superpotential is therefore formal expression of the fact, that the F-term Lagrangian is constructed from product of superfields. Also, we have seen that it contains mass and interaction terms, so that is where the name "potential" came from. It can be used to rewrite SUSY Lagrangian in a compact way:

$$\mathscr{L} = \sum_i (F_iF_i^* + |\partial_\mu\phi_i|^2 - i\overline{\psi_i}\sigma_\mu\partial^\mu\psi_i) + \left[\sum_j \frac{\partial f(\phi_i)}{\partial\phi_j}F_j - \frac{1}{2}\sum_{j,k}\frac{\partial^2 f(\phi_i)}{\partial\phi_j\partial\phi_k}\psi_j\psi_k + h.c.\right] \ . \tag{1.26}$$

The first sum is the D-term Lagrangian, where we have done integration per partes. Compare to the eq. (1.24). The second is the F-term in terms of superpotential - it is straightforward to convince oneself that it reproduces the equations (1.22) and (1.23). Now Euler-Lagrange equations of motion for the F_j are

$$F_j = -\left[\frac{f(\phi_i)}{\partial\phi_j}\right]^* \ .$$

so the Lagrangian is

$$\mathscr{L} = \mathscr{L}_{kin} - \left[\sum_{j,k}\frac{\partial^2 f(\phi_i)}{\partial\phi_j\partial\phi_k}\psi_j\psi_k + h.c.\right] - \sum_j \left|\frac{\partial f(\phi_i)}{\partial\phi_j}\right|^2 \ . \tag{1.27}$$

The last missing piece are the gauge interactions and gauge kinetic terms. To find the first, usual way is to do SUSY version of minimal coupling: $\Phi^\dagger\Phi \to \Phi^\dagger e^{2gV}\Phi$. We can now expand the exponential function in powers of θ (again, there are only several first terms) and work out the the multiplication. The term proportional to $\theta\theta\overline{\theta\theta}$ is

$$\Phi^\dagger e^{2gV}\Phi\mid_{\theta\theta\overline{\theta\theta}} = |D_\mu\phi|^2 - i\overline{\psi}\sigma_\mu D_\mu\psi + g\phi^* D\phi + ig\sqrt{2}(\phi^*\lambda\psi - \overline{\lambda\psi}\phi) + |F|^2 \ . \tag{1.28}$$

In this equation the ordinary gauge covariant derivative was introduced: $D_\mu = \partial_\mu + igA_\mu$, so that the first two terms describes normal scalar-gauge boson interaction and fermion-gauge boson interaction. More interesting is the fourth term where we have field λ, i.e. SUSY partner of A_μ called gaugino. This means that this term describes fermion-(Higgs)boson-gaugino (or higgsino-sfermion-gaugino) interaction.

Final step is the construction of the gauge kinetic term. First, we have to find SUSY equivalent of the field strength $F_{\mu\nu}$. Good candidate is the field

$$W_\alpha = -\frac{1}{4}\overline{DD}D_\alpha V \ .$$

It is easy to show that this superfield is left-chiral, i.e. $\overline{D}W = 0$. This means that the product of these fields is also left-chiral and its $\theta\theta$ component can be used in the Lagrangian:

$$\frac{1}{32g^2}W_\alpha W^\alpha \mid_{\theta\theta} = -\frac{1}{4}F_{\mu\nu}F^{\mu\nu} + \frac{1}{2}DD + (-\frac{i}{2}\lambda\sigma_\mu\partial^\mu\overline{\lambda} + \text{h.c.}) \ . \tag{1.29}$$

Apart from expected ordinary gauge kinetic term, we have also obtained kinetic term for gaugino. Note that everything was done for abelian U(1) gauge theory. If we suppose non-abelian gauge group, we would have more indices and lengthier expressions. Most significant difference would be the term with the gauge boson-gaugino interactions.

Last step is to integrate out the unphysical field D. It is done in the same way as in case of F-term - we calculate Euler-Lagrange equations of motion:

$$D = -g\sum_{ij}\phi_i^*\phi_j \ .$$

The total contribution from the third term of eq. (1.28) and second term of eq. (1.29) is

$$-V_D = -\frac{1}{2}\left|\sum_{i,j} g\phi^*\phi_j\right|^2 \ . \tag{1.30}$$

The complete SUSY Lagrangian is now combination of equations (1.27), (1.28), (1.29) and (1.30).

1.3.5 SUSY breaking, MSSM

In the previous section we have gradually constructed SUSY Lagrangian. However, as you might have noticed, it is fully-supersymmetric, i.e. it predicts that the supersymmetric partners of SM particles have the same mass and also the same coupling constant (interaction strength).

But as far as we know this is not true. Accelerator searches have not found any supersymmetric particle yet and the lower bound on charged sparticles from LEP is about 80-100 GeV [19]. This means that SUSY must be somehow broken. The first idea is of course to try to break SUSY spontaneously, as we did in case of SM.

When we try to do it, we observe, that SSB of SUSY brings many problems. If we suppose that the vacuum state is not supersymmetric, we immediately obtain non-zero vacuum energy, which might bring problems in cosmology (there is a significant difference between value obtained from SUSY SSB and the value anticipated by cosmologists). Also, SSB does not solve the problem of particles-sparticles mass difference entirely: in SSB traces over the mass matrices still remain the same for fermions and sfermions, making it difficult to give all sfermions masses significantly higher than their SM counterparts.

As a result, most models do not try to explain SUSY breaking dynamically, but instead introduce a "soft breaking terms" into Lagrangian. These terms explicitly break supersymmetry and cause sparticles to be heavier than particles, yet they conserve the cancelation of the quadratic divergences, which was the original motivation for SUSY. However, this also means that sparticles cannot have masses much higher than SM particles - about $O(1\text{ TeV})$ at maximum.

The soft SUSY breaking terms are

- scalar mass terms $-m_i^2|\phi_i|^2$
- trilinear scalar interaction $-A_{ijk}\phi_i\phi_j\phi_k$
- gaugino mass term $-\frac{1}{2}m_l\overline{\lambda}_l\lambda_l$
- bilinear terms $-B_{ij}\phi_i\phi_j$
- linear terms $-C_i\phi_i$

If we introduce such terms, the quadratic divergences will still be canceled, but this is not true for any other SUSY breaking terms (e.g. fermion masses) [15].

The simplest realistic SUSY model which satisfies all phenomenological constraints is called minimal supersymmetric standard model (MSSM). The minimal means that it introduces as few new particles and interactions as possible. In principle it only introduces SUSY partner for every SM particle with all consequences.

At first, we have to define the superfields we will need for construction of the MSSM Lagrangian. As was mentioned earlier, SM fermions live in a 5 representations of gauge group, so that we will need 5 chiral superfields which will represent them: Q, which contains quark and squark $SU(2)$ doublets and $SU(3)$ triplets, U^c and D^c which contains quark and squark $SU(2)$ singlets and $SU(3)$ triplets, L, which contains lepton and slepton $SU(2)$ doublets and $SU(3)$ singlets and finally E^c which contain lepton and slepton $SU(2)$ and $SU(3)$ singlet.

Unlike SM, all these fields are left-handed, so that the $SU(2)$ singlet fields (which are right-handed in the SM) contains anti-fermion rather than fermion.

We have to assign a superpartner for Higgs boson too. In this case, however, it is not entirely straightforward. In the SM Lagrangian we use complex conjugate of Higgs field to give masses to up-type quarks. However, such terms are not allowed by SUSY, because superpotential is holomorphic function. Inevitably, there must be two SM Higgs doublets to be able to give masses to all elementary fermions.

This means that without SSB we would have 8 SM Higgs bosons (2 complex doublets). Spontaneous symmetry breaking of $SU(2)$ symmetry turns 3 of them to unphysical Goldstone bosons, so that we are left with 5 Higgs bosons: A - neutral pseudoscalar, h and H - "light" and "heavy" neutral scalar and H^+ and H^- - the charged Higgs bosons. So that in MSSM we need 2 additional left-chiral superfields to describe 2 Higgs doublets, and they give us in total 5 particles and 5 sparticles. Chiral superfields of the MSSM are summarized in table 1.4.

We also have to define superpartners for the vector bosons. So that we have one vector superfield which contains 8 gluons g and 8 gluinos $\tilde{g}$. They will appear automatically if we use $SU(3)$ as a gauge group during the construction of the vector superfields.

In the analogic way we introduce a superfield with three weak vector bosons $W^{\pm}$ and W^0 and three winos $\tilde{W}$. Of course we need a superfield with $U(1)$ gauge boson and its supersymmetric partner: bino $\tilde{B}$. Because of SSB, binos and winos are not mass eigenstates, but instead they mix to form physical states which should be observable in the experiment. Vector superfields of MSSM are summarized in table 1.5.

Now, when we have defined the superfields, we have to set the superpotential (defined by eq. (1.25)). It is constrained by gauge group, however, it is not fixed completely. So that we have to employ the idea of minimality, i.e. we introduce only these terms which are necessary to build a realistic model. Alternatively, we can demand that the lepton and baryon number is conserved, nevertheless, the result will be the same as in the previous case.

After imposing above restrictions we get following superpotential:

$$f_{\mathrm{MSSM}} = \sum_{i,j=1}^{3} \left[(\lambda_E)_{ij} H L_i E_j^c + (\lambda_D)_{ij} H Q_i D_j^C + (\lambda_U)_i j \overline{H} Q_i U_j^c\right] + \mu H \overline{H} \ . \tag{1.31}$$

		Spin 0	Spin $\frac{1}{2}$	$(SU(3), SU(2), U(1))$
quarks and squarks	Q	$(\tilde{u}_L, \tilde{d}_L)$	(u_L, d_L)	$(3,2,\frac{1}{6})$
	U	$\tilde{u}_R^*$	$u_R^\dagger$	$(\overline{3},1,-\frac{2}{3})$
	D	$\tilde{d}_R^*$	$d_R^\dagger$	$(\overline{3},1,\frac{1}{3})$
leptons and sleptons	L	$(\tilde{\nu}_L, \tilde{e}_L)$	(ν_L, e_L)	$(1,2,-\frac{1}{2})$
	E	$\tilde{e}_R^*$	$e_R^\dagger$	$(1,1,1)$
higgs and higgsinos	H_u	(h_u^+, h_u^0)	$(\tilde{h}_u^+, \tilde{h}_u^0)$	$(1,2,\frac{1}{2})$
	H_d	(h_d^+, h_d^0)	$(\tilde{h}_d^+, \tilde{h}_d^0)$	$(1,2,-\frac{1}{2})$

Table 1.4: Chiral superfields of the MSSM. The first five rows are standard multiplets of the SM, sixth line is SM model Higgs doublet + SUSY partner. In the last column we can find in which representation of the gauge group the multiplet is.

	Spin 0	Spin $\frac{1}{2}$	$(SU(3), SU(2), U(1))$
gluinos and gluons	$\tilde{g}$	g	(8,1,0)
winos and W-bosons	$\widetilde{W}^{\pm}, \widetilde{W}^0$	$W^{\pm}, W^0$	(1,3,0)
bino and B-boson	$\tilde{B}$	B	(1,1,0)

Table 1.5: Vector superfields of the MSSM. In the third column there are SM gauge bosons, in the second column are their SUSY partner. In the last column we can find in which representation of the gauge group the multiplet is.

There, i and j are generation indices, λ's are matrices with respective Yukawa couplings and also we assume contraction over $SU(2)$ and $SU(3)$ indices:

$$H\overline{H} = H_1\overline{H}_2 - H_2\overline{H}_1 \ ; \qquad QD_R^c = \sum_{i=1}^{3} Q_n (D_R^c)_n \ .$$

You may notice, that the structure is the same as in the case of the SM: the first term is Higgs giving masses to leptons, next we have Higgs giving masses to down and up quarks.

Also note, that this choice of superpotential brings another conservation law, so called "R parity conservation". This means that interaction vertices introduced by (1.31) contain even number of superpartners. This in particular means that there is no interaction of type incoming sparticle, outgoing particle(s), i.e. the lightest supersymmetric particle (LSP) is absolutely stable, because it cannot decay.

Thanks to this, LSP is a good candidate for dark matter observed by astrophysicists. Also, there are good reasons to believe that LSP is color and electromagnetic neutral: if not, it would interact with nuclei, and thus creating very exotic isotopes with strange mass to charge ratios. Searches for such a phenomena gave very strict restrictions on their mass - if LSP had color or EM charge, it would have to be heavier than several TeV. This would on the other hand destroy the SUSY ability to deal with the quadratic divergences. So it is believed that LSP (if exists) should be neutral.

Consequently, LSP would behave like a heavy neutrino, so that we should have clear signature of SUSY events in collider experiments: all emerging SUSY particles eventually decay into LSP which fly away from the detector unnoticed, i. e. all SUSY events have some missing energy.

Last step in the construction of the theory is the SUSY breaking. As was stated earlier, it is not easy to do it spontaneously, so that MSSM introduces soft breaking terms. Unfortunately, that brings about 100 new parameters.

This concludes introduction to SUSY and a brief discussion of one realistic SUSY model: the MSSM. We have seen that the SUSY principles are very appealing in a mathematical way, but also can solve some problems we have in SM and in GUT's. The fact that SUSY deals with quadratic divergences is not surprising because SUSY was invented just for this purpose.

However, SUSY brings also other, highly nontrivial things - only after applying SUSY we get the unification of coupling constants (Fig. 1.5) and also the higher GUT scale which helps us in passing experimental tests on proton lifetime.

Obviously, SUSY must be broken, as we do not observe any sparticles, that would have been seen if the SUSY was exact. Nevertheless, it is quite difficult to break SUSY spontaneously, so that we rather use "soft breaking terms", i.e. terms which explicitly break SUSY, while the main features of it remain untouched.

The simplest possible realistic SUSY model is MSSM, the minimal SUSY extension of the SM. In most cases, its prediction does not differ much from the SM, but there are several possible observation which can exclude the SM and point to some of the SUSY models. The example is the existence of charged Higgs boson: the SM predicts only neutral Higgs, so that existence of charged scalar particle (which is quite well observable in the experiment) can show the way beyond the SM. The same case is the existence of LSP - its discovery will prove R-parity conservation and thus exclude SUSY models which do not have this symmetry. Also, existence of LSP and its properties can be the key in understanding dark matter of cosmology.

1.4 Neutrino physics

The story of neutrino resembles the turning of ugly duckling into a beautiful swan. Starting as a desperate idea of Wolfgang Pauli it turned into one of the most interesting particles of the SM and into a possible probe of the physics beyond the SM.

As was pointed out earlier, SM predicts that there are 3 types of exactly massless neutrinos, which are *only* left-handed and interact only via weak and gravitational interaction. Most of this was confirmed by the experiment: Neutrino was observed in the bubble chambers in the 1960's, LEP precision measurements of Z decay showed that there are 3 types of light[4] neutrinos and nobody has observed right-handed neutrino so far.

On the other side, experiments like Super-Kamiokande in 1990's have shown that neutrinos travel at a speed which is lower than a speed of light, indicating that they are massive. This in turn brings the possibility of neutrino oscillation (i.e. switching between different mass eigenstates), and thus solving the "solar neutrino problem"[5].

This brings us to the decision, how to amend the SM to be consistent with this observation, i.e. how to give mass to the neutrino. Obviously, we cannot use the same approach as in case of other elementary fermions - Higgs mechanism. This would have led to the introduction of a Dirac-like mass term for neutrino, implicating that the right-handed neutrino should be observed in the same abundance as its left-handed counterpart, which is not the case.

---

[4] Lighter than half of Z mass.

[5] Nuclear reactions in the Sun produce electron type neutrinos. However, on Earth we observe much less neutrinos of this type than we should if our Sun model is correct. The explanation is that part of the electron type neutrinos "oscillate" to become muon type or tauon type neutrino.

However, nothing prevents us from introducing a Majorana[6] mass term into a SM Lagrangian, so that we would have two distinct classes of neutrino mass terms (for one fermion generation) [20, 21]:

$$\mathscr{L}_{mass} = -m_D \left(\overline{\nu}_L \nu_R + \overline{\nu}_R \nu_L\right) - \frac{1}{2} m_M^L \left(\overline{\nu}_L \nu_L^C + \overline{\nu}_L^C \nu_L\right) - \frac{1}{2} m_M^R \left(\overline{\nu}_L \nu_L^C + \overline{\nu}_L^C \nu_L\right) \ . \tag{1.32}$$

In this equation m_D denotes Dirac mass of neutrinos and m_M^L and m_M^R denotes Majorana mass of left and right handed neutrinos, respectively. Using the properties of charge conjugation operator [1], we can express last equation in terms of neutrino mass matrix $\mathcal{M}$:

$$\mathscr{L}_{mass} = -\frac{1}{2} \left(\overline{\nu}_L \overline{\nu}_R^C\right) \mathcal{M} \begin{pmatrix} \nu_L^C \\ \nu_R \end{pmatrix} + \text{h.c.} \ , \tag{1.33}$$

where

$$\mathcal{M} = \begin{pmatrix} m_M^L & m_D \\ m_D & m_M^R \end{pmatrix} \ . \tag{1.34}$$

Natural next step is to diagonalize the mass matrix to find the mass (i.e. physical) eigenstates. If we suppose that $m_M^R \gg m_D$ we would find that first eigenvalue is $m_1 = m_D^2/m_M^R$, while the second is $m_2 = m_M^R$. Corresponding eigenvectors are

$$\begin{aligned} \nu &= \nu_L + \nu_L^C \\ N &= \nu_R + \nu_R^C \ . \end{aligned} \tag{1.35}$$

The first line corresponds to the small eigenvalue m_1, while the second corresponds to the large eigenvalue m_2. So that in this way we would obtain two physical neutrino fields: one very heavy, practically right-handed neutrino and one very light practically left-handed neutrino.

This approach is also called seesaw mechanism: if we assume that $m_1 = 0$ (i.e. zero mass for left-handed neutrinos), we would find (from eigenvalue equation) following relation between Dirac and Majorana masses:

$$m_M^R m_M^L = m_D^2 \ .$$

That implies that for given m_D the larger m_M^R the smaller m_M^L. So that with our assumption $m_D \ll m_M^R$ we have $m_M^L \approx 0$ and $m_2 = m_M^R$.

By this we can explain why we can observe tiny, yet massive left-handed neutrino. However, we should also justify our assumption $m_D \ll m_M^R$: if we suppose, that we have only Majorana mass terms, than our mass matrix (1.34) would have nonzero entry only at lower left corner. Then, our assumption means we are dealing with a small perturbation with respect to this matrix.

When we introduce other two neutrino families, we would obtain neutrino mixing matrix which parameterize the neutrino oscillations and therefore has measurable entries.

Only one question remains unanswered: can we somehow prove the existence of the seesaw mechanism itself? Although it was for a long time assumed that it is not the case, recent findings [22] show that with combined results from searches for double beta decay, LHC, ILC and dedicated neutrino experiments it would be possible.

---

[6] Majorana fermions fulfill Majorana equation [1] and, generally speaking, Majorana particles and antiparticles are (unlike Dirac fermions) identical.

1.5 Summary

In this chapter we have seen how we can describe (nearly) all observable phenomenology by the Standard Model - minimalistic theory based on a few basic principles. On the other hand, we have also seen the weak points of the SM: peculiar hypercharge assignment, problems with scalar mass quadratic divergence and problem with neutrino mass.

The first can be solved by GUT's which itself has several problems (unification of gauge couplings and proton stability), but this is cured as a by-product of Supersymmetry, which itself was invented to deal with the scalar mass divergence. SUSY also brings brand new phenomenology which can be directly tested at LHC. Last problem can be solved by the introduction of Majorana mass term for neutrinos and the reliability of this model can be tested by current and future experiments.

Chapter 2

Experimental Validation of the Standard Model

2.1 Methods of Experimental Particle Physics

The key property of every physical theory is its ability to give verifiable predictions. Quantum field theory (and Standard Model as its special case) typically give two types of predictions. The first one is the existence of some particular elementary particle or some interaction vertex. In this case, the experiment can reach only two outcomes: the particle (or vertex) either exists or it does not. In case of the SM all predicted particles have been observed with the exception of Higgs boson[1]

In case of vertices, also all of them (apart from these containing Higgs boson) have been observed (e.g. cubic and quartic gauge boson self-interaction or flavour changing charged currents) and no others (e.g. photon self-interaction or flavour changing neutral currents[2]).

Second type of QFT predictions are cross-sections and decay widths. As was mentioned in the first chapter, this numbers have been in case of the SM confirmed with extraordinary precision.

But what do we actually measure in the experiment? The basic scheme is always the same: we have some source of particles (typically collisions in particle collider) and we measure their properties like scattering angle, charge, mass or momentum. This helps us to identify the particle which was produced in collision and so measure its production rate, which has unambiguous correspondence to the particle production cross-section:

$$\frac{\mathrm{d}\sigma}{\mathrm{d}\Omega} = \frac{1}{L}\frac{\mathrm{d}^2 N}{\mathrm{d}t\mathrm{d}\Omega}\ , \tag{2.1}$$

Here, $\mathrm{d}\sigma/\mathrm{d}\Omega$ is differential cross-section for the outgoing particles in space angle Ω, L is the machine luminosity (measure of the density of beam) and $\mathrm{d}^2N/(\mathrm{d}t\mathrm{d}\Omega)$ is the number of particles outgoing in unit time in space angle $(\Omega, \Omega + \Delta\Omega)$.

Also, if particle is unstable, we can identify in the same way its decay products and measure the decay rates of the parent particle. Mostly we can also measure how far did particle fly before it decayed, so that we can, knowing its momentum, calculate the lifetime and decay width. And from the invariant mass of its products we can measure the mass of the parent particle. The decay products are usually the only way how to identify the primary particle which emerged in the beam collision.

---

[1] There is a possibility that Higgs was observed during the last days of LEP, nevertheless the statistics was too small to claim a discovery [24].

[2] To be exact, these FCNC's are forbidden at tree level, but allowed via loops, meaning that they are rather largely suppressed than not existing at all.

For example, we would like to know, if there was any Z boson produced in the collision. SM predicts that Z boson decays 70 % of time to quarks, 20 % of time to neutrinos and 10 % of time to charged lepton-antilepton pair. So what we can do is to look in every event for an electron pair (which is easy to identify) and plot its mass in a histogram. If the number of events would be sufficiently large, we would obtain something similar to Gaussian with a peak centered at the Z boson mass. It is also useful not to plot every electron pair, but only these which meet some criteria on their energy and direction of flight.

This is also the way how to discover new particle: we are looking for its decay products, plot their invariant masses, and if we find some mass peak, it is possible, that they are originating from the the new particle. However, to make sure that this was not a random fluctuation, we usually have "5σ criterion". This means, that the probability that the result was due to fluctuation is smaller than 0.00006 % (the probability of 5σ deviation in case of Gaussian distribution).

These were two simple examples like statistical approach can interpret experimental data. However, we can also do much more complicated analysis. Imagine, we have a sample with two types of events (usually, there will be more of them, but two is enough to explain the idea). For each event, we measure two properties, x_i and x_j - this can be position, energy, mass or any other observable property. The example of the plot of such an events in 2-dimensional parameter space is on Fig. 2.1 (a). Note that the plot is a result of simulation and contains the information from the Monte Carlo generator - events of one type are blue, events of second type are red. Now we want to use this simulation to learn, how to choose only one type of events. The Fig. 2.1 shows that the criterion can be simple cut in every variable. Obviously, we can also use more complicated function of x_i and x_j which could do better.

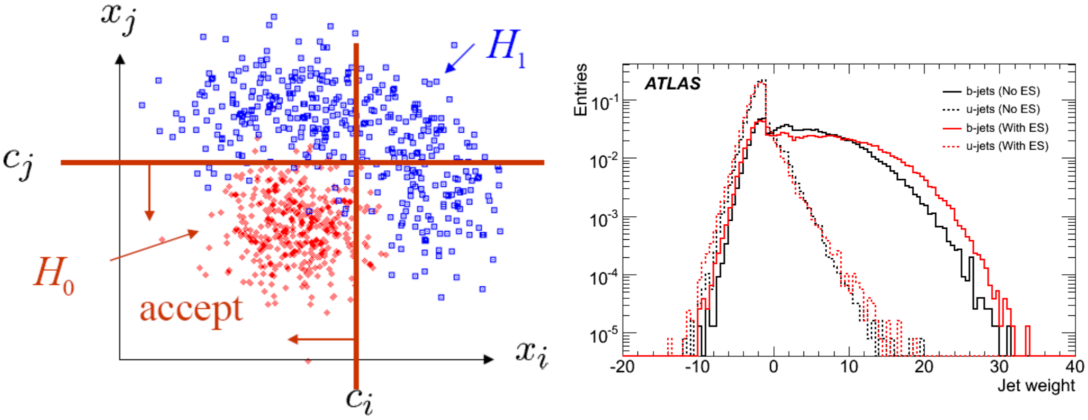

(a) 2D statistics

(b) Test statistics

Figure 2.1: The example of 2D distribution of a signal (red) and background sample (blue) is on figure (a). Originally from [26]. Test statistics constructed from multidimensional analysis is on figure (b). The signal is denoted by solid black or red line, while background is dashed red or black line. Originally from [27].

So we have two questions: what is the measure of quality of selected sample and how to find the best criterion for selection. First note, that it is often convenient to construct test statistics of lower dimension (usually scalar) $t(x_i, x_j)$ and find selection criterion for it. This means, that we have to find some t_{crit} and if $t < t_{crit}$ than we say that the first hypothesis is valid and if $t > t_{crit}$ we say that the second hypothesis is valid.

Next, the quality of sample is measurable by 2 quantities. The first is efficiency, i.e. how large fraction of the events of the required type are we able to choose with our criterion. The second is purity, i.e. how many events of the other type we select to be part of our sample. It is obvious that these variables are somehow complementary: higher efficiency is leading to lesser purity and vice versa.

Optimal selection means optimal trade off between purity and efficiency. Neyman-Pearson lemma gives us a hint, how to choose a test statistics in the best way (for given efficiency it leads to highest purity). It says, that if we know the probability density functions for both type of events (or, equivalently, conditional probability density function, given hypothesis 1 and 2), the optimal test statistics is

$$t(\vec{x}) = \frac{f(\vec{x}|H_1)}{f(\vec{x}|H_2)} \ ,$$

or any monotonous function of it. Symbol $f(\vec{x}|H_1)$ means the probability, that the event will be in parameter space region $\vec{x} + \Delta\vec{x}$, given the first hypothesis holds (i.e. it is the event of the first type). The proof of this lemma is in [25].

When constructing the test statistics, we can obtain something similar to 2.1 (b). On this picture we can see the distribution of the test statistics for two hypotheses: the jet in question is originating from bottom quark or it is originating from some light quark. Our test statistics is called jet weight W and is calculated according to Neyman-Pearson lemma:

$$W = \sum_i \ln \frac{b(S_i)}{u(S_i)} \ . \tag{2.2}$$

It is obvious, that the jet weight is the logarithm of the test statistics from the lemma. The conditional distribution functions are $\prod_i b(S_i)$ for the first and $\prod_i u(S_i)$ for the second hypothesis; i goes over all tracks in examined jet. We can see, that the distribution function for every hypothesis is product of many independent one-variable distribution functions. These functions describe the probability that the particular track i belongs to bottom jet or to the light jet, respectively, as a function of S_i, which is a geometrical parameter describing the track (it is called significance of the impact parameter).

So that we have some multivariate probability distribution functions for both hypotheses (being bottom jet or being light jet), which were turned into scalar test statistics (called jet weight) according to the Neyman-Pearson lemma (eq. (2.2)). Note that for each jet we now obtain one number: the weight. The distribution of the jet weight is on Fig. 2.1 (b). We can see the clear separation of the two hypotheses, allowing us to make a selection.

2.2 Search for Higgs Boson

While the previous section mentioned in general how to use statistics in particle physics, next section would show how we can discover Higgs boson with LHC and how we can measure its properties. It will discuss what LHC can see in case the Higgs would behave according to the SM predictions and also the main differences predicted by the MSSM.

2.2.1 Available production and decay channels

If we want to discover predicted particle, we have to know how to produce it and how we can detect it with our experimental device. At present, the most promising device for the discovery of Higgs boson is LHC[3], currently being finished at CERN. This machine will collide proton beams, each with energy 7 TeV. Equally important, the machine designed luminosity about hundred times larger than Tevatron has.

---

[3] Although it may be possible to observe light Higgs boson at currently running Tevatron at Fermilab, it is believed that this machine will not be able to collect enough statistics to claim a discovery. More on Tevatron searches is in [28].

The outcome of collisions will be studied by 4 big experiments: two general purpose detectors (ATLAS and CMS), one experiment focused on heavy-ions (ALICE) and one aimed at B-physics (LHCb). More detailed description of the experimental device will follow in the next chapter.

Standard Model predicts that Higgs couples to all massive particles, so that it is theoretically possible that it will be produced directly in the proton-proton collision at LHC. However, SM also predicts that the Higgs coupling is proportional to the particle mass, i.e. Higgs couples most strongly to the heaviest particles. Consequently, it is much more probable to produce some heavy particle which will decay into Higgs than the Higgs boson itself. Thus in case of LHC we may focus on four production channels:

- Gluon fusion. There is no coupling between Higgs and gluons, but we can use particles in the loop. Top quark has the strongest coupling to the Higgs boson, so that it is natural to expect a production via this particle. Of course, there can be also other quarks in the loop, but the top contribution is by far the largest. Feynman diagram is on Fig. 2.2 a).

- Weak Boson Fusion (WBF). Constituent quarks from passing protons may emit a pair of weak bosons which may fuse to form a Higgs boson. This channel is very distinctive (see later) so it has been studied very well. Feynman diagram is on Fig. 2.2 b).

- Higgsstrahlung. This was the only viable production channel on LEP as the other three were beyond its mass reach, or kinematically impossible (WBF). In case of LHC, collision of two quarks can produce highly energetic W boson which can emit Higgs boson. Because of the similarity of this process to the bremsstrahlung in QED, it was nicknamed Higgsstrahlung. Feynman diagram is on Fig. 2.2 c).

- Top quark associated production. Because of its huge energy, LHC can produce Higgs boson not only via virtual top, but together with real top quarks. Due to production of three massive particles this channel has also very distinctive signature. Feynman diagram is on 2.2 d).

The plot on Fig. 2.3 (a) shows cross section of various production channels - we can see, that gluon fusion and weak boson fusion are two most promising ways of producing Higgs. If we multiply this cross-section with the anticipated amount of LHC data which is several hundreds fb^{-1}, we would see that LHC would become a Higgs factory, producing $O(10^5)$ SM Higgs bosons in case it would be heavy and about ten times more if it would be light.

However, Higgs boson is an unstable particle, i.e. we cannot detect it directly but only via its decay products. The branching ratio of Higgs decay channels is on Fig. 2.3 (b). We can see, that it is strongly dependent on Higgs mass. Also, we can observe, that the decay products are preferably as massive as kinematically possible.

Comparing Figs. 2.3 (a) and (b) we can see, that most Higgs boson will be produced in a reaction $gg \to H \to b\bar{b}$ in case of light Higgs and $gg \to H \to W^+W^-$ in case of heavier Higgs. When we multiply the number of Higgs bosons produced by gluon fusion by the branching ratios of decays to $b\bar{b}$ and W pair respectively (50-90 %, depending on Higgs mass) we would find, that the data sample would be really large (tens of thousands events at least).

However, it is too soon to celebrate - we have not yet taken in account the background. Figure 2.4 shows cross-section of various physical processes on proton - (anti)proton colliders. Dominant background for $H \to b\bar{b}$ decay is QCD b-pair production (governed by inclusive b production σ_b) and single top production (denoted as σ_t on Fig. 2.4) where top decays to $b\bar{b}$. Fig. 2.4 shows that the background is about 7 orders of magnitude larger than Higgs signal, making the detection of light Higgs practically impossible.

In case of heavy Higgs ($M_H \gtrsim 150$ GeV), the decay into W pair dominates. Its background is direct W bosons production. This is electroweak process, so that it has several orders of

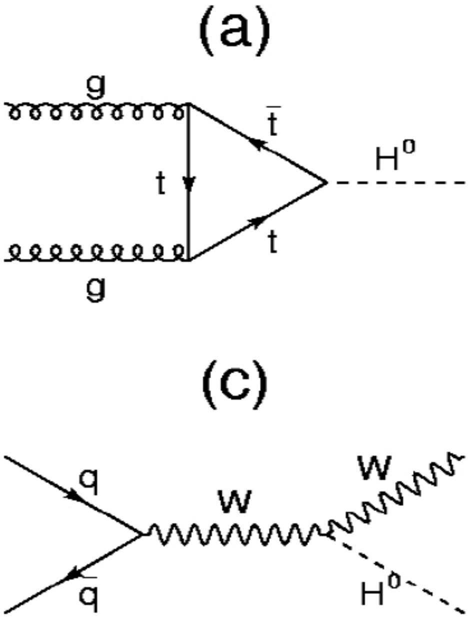

Figure 2.2: Feynman diagrams of four Higgs production channels on hadron collider. It depicts gluon fusion (a), weak boson fusion (b), Higgsstrahlung (c) and top quark associated production (d). Details are given in the text. Figure taken from [28].

magnitude smaller cross section than b quark production (see Fig. 2.4). In fact, $gg \to H \to WW$ will be excellent channel for heavy Higgs due to its abundance.

Before I will discuss next production process, I would like to mention the channel $gg \to H \to \gamma\gamma$. Although the branching ratio of decay to photons is only $10^{-3} - 10^{-4}$ (this decay is forbidden at tree level, so that it is highly suppressed), we can get at least several hundreds of these events thanks to the huge gluon fusion production rate. And because this signal is extremely clean (the background is well known), it can offer very precise measurement of Higgs mass, although it will not be probably the first channel to see the Higgs boson due to its low rate.

Next in numbers of produced Higgs bosons, is the weak boson fusion. Figure 2.5 shows lego plot of such an event, i.e. the energy deposit as a function of polar angle ϕ and pseudorapidity η[4]. We observe that detector can see one forward and one backward jet from scattered quarks and central jets coming from Higgs decay. Thanks to this very distinctive signature which is hard to mimic and decent production rate (thousands, even for the early LHC data), WBF is likely to be Higgs discovery channel.

As in the previous case, there is no point in trying to find Higgs decaying to $b\bar{b}$ as the QCD background is still overwhelming. However, next-to-largest rate for light Higgs is decay to $\tau^+\tau^-$, which has only EW background which is several orders of magnitude smaller than QCD one. The only problem is that tau decay involve necessarily at least two neutrinos, bringing some uncertainty into invariant mass reconstruction which could be greatly reduced by some kinematic assumptions, however. More details in [28]. The plot produced by the ATLAS collaboration

---

[4] Pseudorapidity is defined as $\eta = -\ln \mathrm{tg}(\theta/2)$ where θ is polar angle. Zero pseudorapidity have particles flying perpendicular to the beam, infinite pseudorapidity have these flying parallel with beam. For particles going with the speed of light the pseudorapidity is identical to the rapidity.

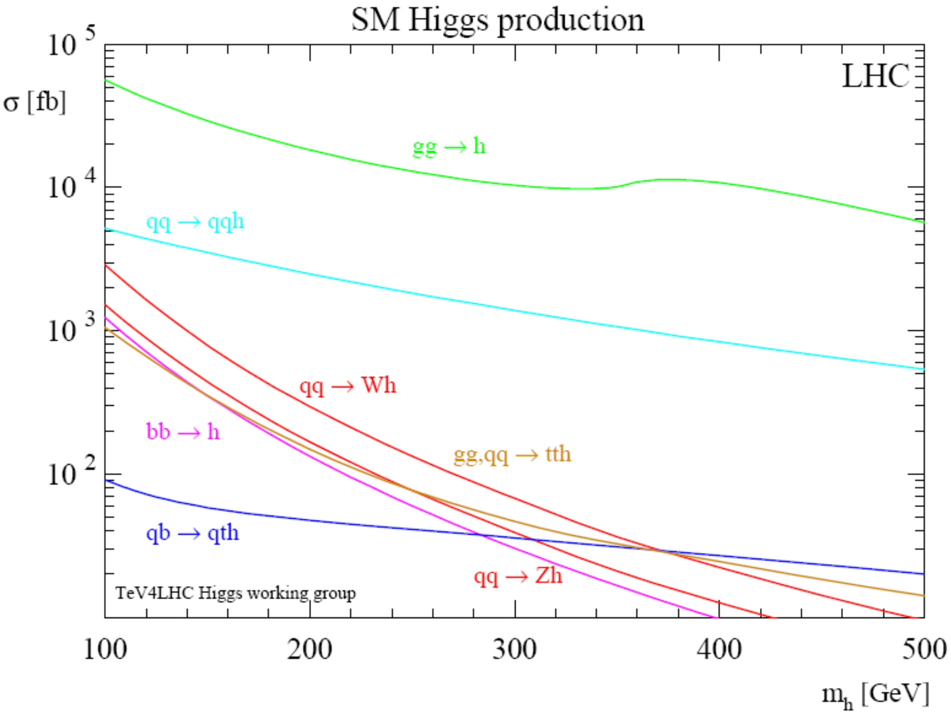

(a) Higgs Production

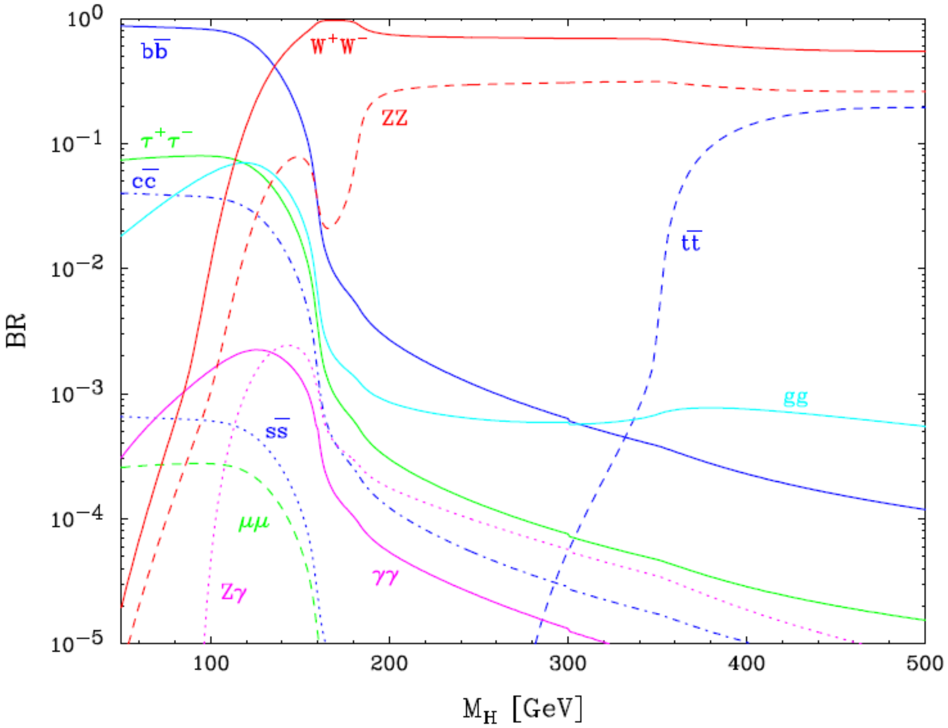

(b) Higgs Decay

Figure 2.3: Cross section of several Higgs production channels at 14 TeV (a) Branching ratio of various Higgs decay channels (b), both as a function of Higgs mass. Figure from [28].

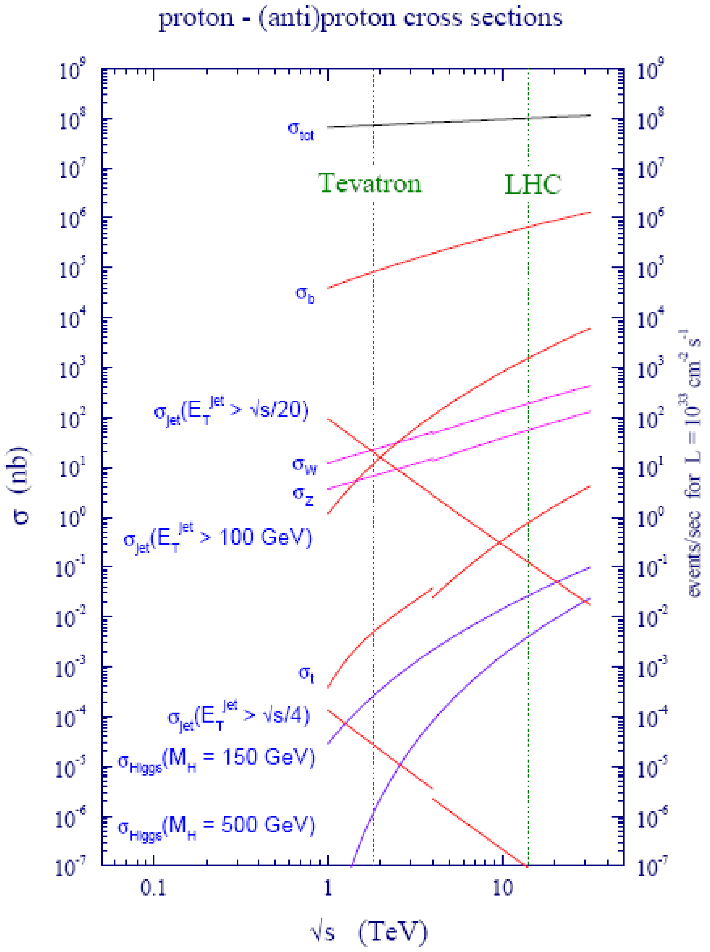

Figure 2.4: Cross section of various processes at Tevatron and LHC. Higgs signal (for two different masses) is σ_{Higgs}. Inclusive b production, which is dominant background for $H \rightarrow b\bar{b}$ is denoted as σ_b. Discontinuity is caused by differences between $\bar{p}p$ and pp collisions. Figure originally from [28].

showing the possible signal over background is on Fig. 2.7 (a).

In the case of heavy Higgs, we have decay into W pair, which is, as we have already learned, better for Higgs identification. Indeed, Fig. 2.7 (b) show that the signal in this case is much higher than background.

As in the previous case, decay to the photons is also possible, but due to much lower rate, it will surely not lead to discovery of SM Higgs, but it may serve well in precise coupling constant measurement.

The third production channel, Higgsstrahlung, was mentioned because it was the only production channel in LEP, and it is main production channel of light Higgs in Tevatron. However, as Fig. 2.4 show, its rate is falling steeply with Higgs mass and, moreover, its background cross-section grows QCD like. Therefore, Higgsstrahlung is very badly identifiable at LHC.

Last channel is very complex top quark associated Higgs production ($t\bar{t}H$ in technical parlance). Like WBF, it is a very complex event (see Fig. 2.6), but in the case of light Higgs it is easily imitable by $t\bar{t}$ production. Even larger problem than the poor signal to background ratio (about 1/6) is that we do not know the background well. To be exact, the background shape uncertainty is about 10 %, thus the statistical significance cannot be larger than 3σ even if we

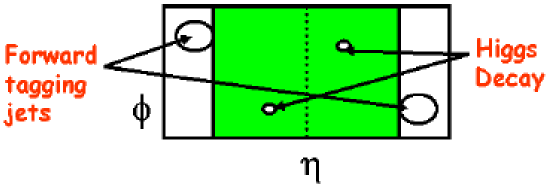

Figure 2.5: Lego plot (energy deposit as a function of polar angle and pseudorapidity) of weak boson fusion. Figure originally from [28].

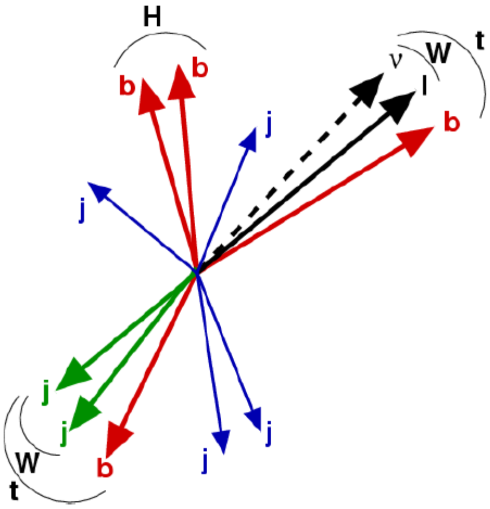

Figure 2.6: The schematic view of top quark associated Higgs production, where Higgs decays to $b\bar{b}$ pair. Figure originally from [28].

would have infinite amount of data [29].

As we have learnt in the previous cases, the situation becomes much better in the case if the Higgs is heavy. The background is relatively small and well known, so that this channel do not suffer from the background uncertainty as does $t\bar{t}H \to b\bar{b}$. On the contrary, this channel may obtain great importance as soon as Higgs would be discovered and its couplings to W bosons measured (e.g. at WBF). Knowing this, we can use $t\bar{t}H \to WW$ to measure Higgs-top coupling.

To conclude this section there is a plot made by ATLAS collaboration which summarizes its discovery potential (Fig. 2.8). We can see the significance of various channels, WBF clearly having the biggest discovery potential. The black curve showing the total significance is signaling that ATLAS will be able to make convincing observation of Higgs boson over very broad mass range. Note that the plot is for approximately 1/10 of planned of LHC data.

2.2.2 SM Higgs

Last section described how to discover Higgs boson. But this is not all: on the contrary - at the moment the new mass peak is discovered the *real* physics starts. We have to test, whether this new particles really behaves according to the SM predictions, or if some other theory describes it more properly.

This means, that we have to measure quantum numbers of newly discovered particle and compare them with theoretic predictions. These quantum numbers are electric and color charge, mass, spin, CP eigenvalue, gauge couplings, Yukawa couplings and spontaneous symmetry breaking potential (Higgs self-couplings) [28].

The measurement of color and electric charges is trivial - we know it directly from the decay products (or, more precisely, we can immediately tell whether the new particle is electric and color neutral or not).

The mass measurement was discussed in the last section - we can use various decay and production channels and in general we can expect precision of several per-mills with the complete LHC statistics. This is good enough because theoretical uncertainties are in the range of a few GeV's. There are no predictions on Higgs mass, except from experimental lower limit of 114.4

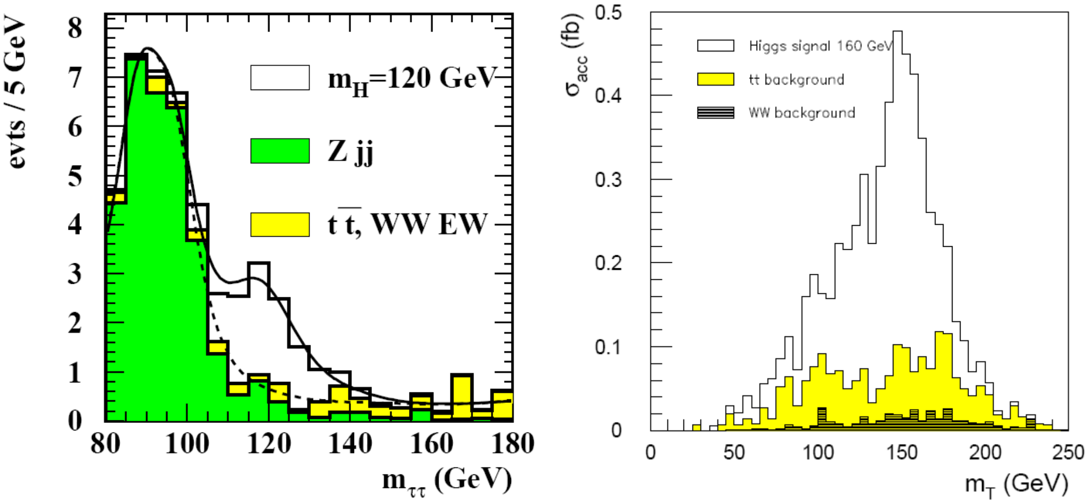

(a) $H \to \tau\tau$

(b) $H \to WW$

Figure 2.7: Higgs signal and background at WBF for light Higgs (120 GeV) decaying to τ pair (a) and heavier Higgs (160 GeV) decaying to W pair (b). Left plot shows event rate, the right shows cross section, both as function of invariant transverse mass. Figures from [28].

GeV coming from LEP [11] and several constraints form precision measurements [6], which give upper bound on SM Higgs mass to be about 200 GeV. But these constraints are not very strong and it is quite possible that Higgs would be heavier.

The measurements of spin and CP eigenvalues[5] are linked - both require measurement of angular distributions. SM predicts that Higgs is a scalar particle, i.e. its spin is 0 and CP state is even.

There are several methods of measuring spin and CP eigenvalue, each of them looking at different observable which allows discrimination between scalar (spin 0) and vector bosons (spin 1)[6] and pseudoscalars and pseudovectors (CP odd states). The results from one method, which uses relative angles between decay planes of Z bosons in $H \to ZZ$ is on Fig. 2.9. We can see, that we can distinguish scalar from pseudoscalar easily and scalar from vector for Higgs heavier than 200 GeV. There are also other techniques which are useful for lighter Higgs, so that we can say, that LHC will allow us to confirm whether Higgs really is scalar boson. More details again in [28].

Now comes the difficult part - measuring of the Higgs couplings. In fact, it was widely believed, that the measurement will not be possible at all and that LHC will measure only branching ratios. The reason for this believe was that like any other particle physics experiment, LHC can measure only rates of various channels and from them obtain $\sigma_i \cdot BR_j$ where σ_i is cross-section of production channel i and BR_j is branching ration to jth decay channel.

Note that for light Higgs we have $\sigma_{gg\to H} \propto \Gamma_{H\to gg}$ This is because they share the same matrix elements (cf. [1]) and differ only in phase space factors. The same is true for WBF, so that $\sigma_{WBF} \propto \Gamma_{H\to WW}$. If we use convention, that partial Higgs decay widths are labeled according to their final state, we obtain following expression for the branching ratio to decay

---

[5] Because CP is discrete symmetry, there are two possible values: 1 (CP even states) and -1 (CP odd states). The first case are e.g. scalar particles, the latter is e.g. pseudoscalars.

[6] We can tell whether candidate particle is boson or fermion readily from decay products.

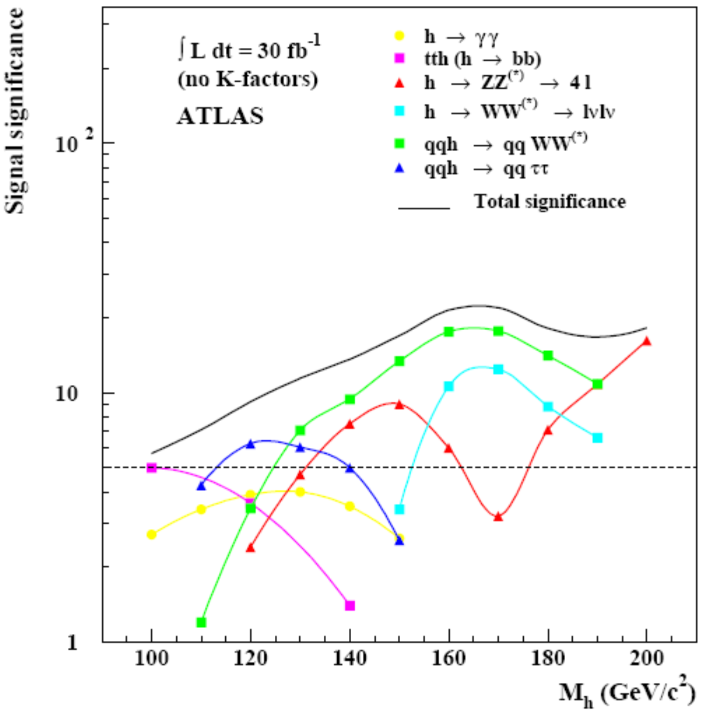

Figure 2.8: Obtainable statistical significance for various Higgs channels together with total significance with 30 fb^{-1} of LHC data. Dashed horizontal line is 5σ, i.e. the lower limit for discovery. Figure originally from [28].

product d: $BR_d = \Gamma_d/\Gamma_H$ where Γ_H is Higgs total decay width. Now we can write

$$(\sigma_H \cdot BR)_i \propto \left(\frac{\Gamma_p \Gamma_d}{\Gamma_H}\right) , \tag{2.3}$$

where Γ_p is production decay width. The value on the left we get from the experiment, and we would like to find the values of all Γ's and from them we would obtain Higgs couplings. Suppose we have only one production channel and n decay channels, one for every possible Higgs decay. From the experiment, we would obtain n partial decay widths, and the total width would be just their sum.

However, in reality we do not have channels for each Higgs decay as some of them have the same final state and some are unobservable. But we can get help from the SM which predicts some relations between decay widths (mainly that they are proportional to the mass of coupled particle with universal constant of proportionality for all fermions and there are also relations between fermion and vector boson decay widths). These can help reduce some degrees of freedom (d.o.f.) in the expression (2.3) and so measure the decay widths and consequently obtain the couplings. Fortunately, there is more decay channels available than we need after this d.o.f. reduction - this is important, because we want to *prove* that Higgs couplings are proportional to the mass. And this additional decay channels will serve as a cross-checks of our hypothesis.

The pessimistic scenario on precision of couplings measurements is on Fig. 2.10. Note also that future ILC will have much better conditions for Higgs couplings measurements as it will have clean environment of electron-positron collisions [28].

The most difficult is measuring the Higgs self-potential. On the other hand, it is also the most important measurement, because the existence of cubic and quartic Higgs couplings is firm

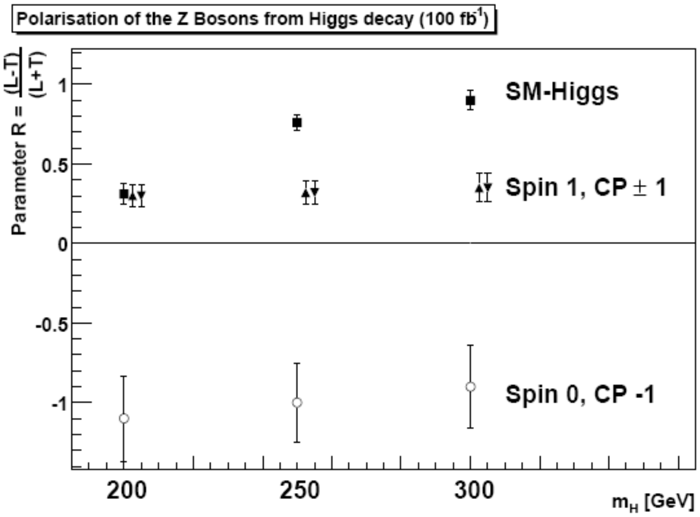

Figure 2.9: Results from the analysis of polarization of Z bosons from Higgs decay. Plot shows that pseudoscalar could be ruled out easily, while the distinction between (pseudo)vector and scalar can be made only for higher masses. Figure originally from [28].

prediction of the spontaneous symmetry breaking. According to it, the Higgs potential has the form

$$V(H) = \frac{1}{2}M_H^2 H^2 + \lambda H^3 + \frac{1}{4}\tilde{\lambda} H^4 \ . \tag{2.4}$$

There are again relations between parameters λ, $\tilde{\lambda}$ and M_H, as well as connection to the Higgs couplings, but to prove SSB we must take them as independent parameters and later check their values again these we can obtain from already measured Higgs mass and couplings.

To measure λ, we must find some three-point Higgs interaction. The best possibility is to look for them in Higgs pair production (Fig. 2.11). The two diagrams interfere destructively leading to production rate which is about ten times smaller than for ordinary Higgs. Like in the case of single Higgs production, dominant decay at low Higgs mass is to $b\bar{b}$ pairs, which is impossible to discriminate from backgrounds. Better situation is for higher masses, where we have decay to four W's, which is more easily identifiable. For low Higgs mass it is also worth to look to decay to $b\bar{b}\gamma\gamma$ which is extremely clean, albeit very rare (BR=0.001).

Although it is difficult to measure the precise value of Higgs 3-point coupling, it is much more easier to find whether there is any. If we introduce discriminating variable m_{vis} (visible invariant mass) as

$$m_{vis}^2 = \left[\sum_i E_i\right]^2 - \left[\sum_i \vec{p}_i\right]^2 \ , \tag{2.5}$$

where i goes through all final state particles and plot differential cross-section vs. m_{vis}, we would get something like on Fig. 2.12. We can see that for one we can easily distinguish signal from background and, more importantly - we can discover whether there is Higgs 3-point coupling or not. In case there is no 3-point coupling, there is no destructive interference in Higgs pair production and therefore the cross-section is much larger than in the case when Higgs 3-point coupling exists.

Therefore we can use Higgs pair production to *exclude* non-SM hypotheses on Higgs triple self-coupling. Figure 2.13 shows how well we can exclude non-SM values of λ as a function of collected data and Higgs mass.

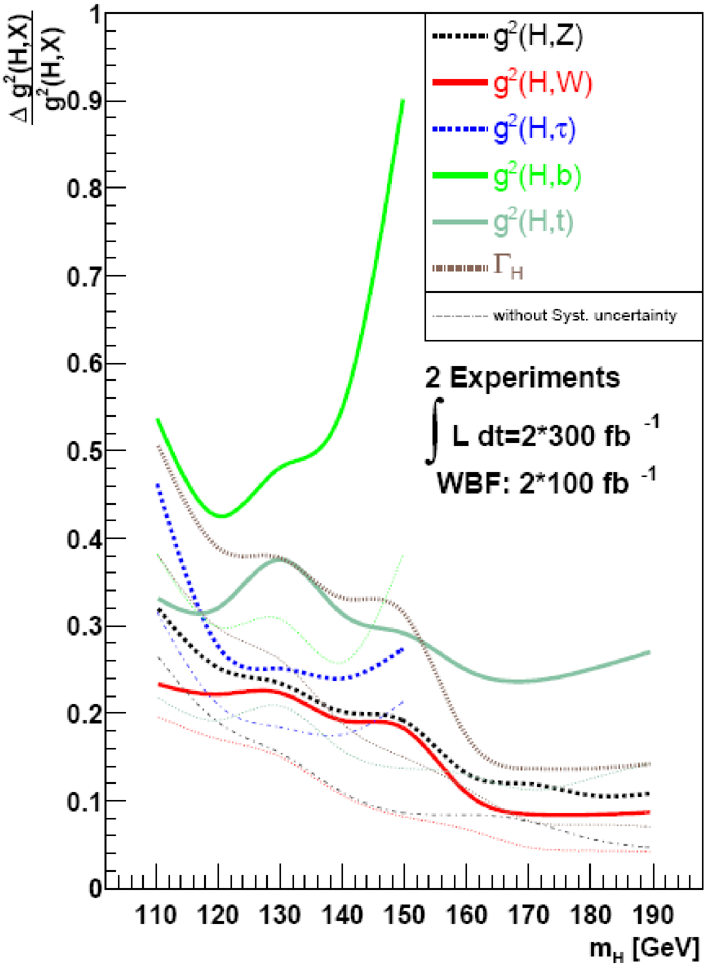

Figure 2.10: Rather pessimistic view about possible precision of coupling measurements at LHC. Plot assumes using combination of data from ATLAS and CMS after complete LHC running. Figure originally from [28].

To sum up, we can measure λ at LHC quite well in case Higgs would be heavy. However, we would run into deep problems in case Higgs is light because there is either too large background (decay to $b\bar{b}b\bar{b}$), or the rate is just too small to obtain any serious statistics ($b\bar{b}\gamma\gamma$). Nevertheless, for ILC the situation is opposite - it works well for light Higgs mass and poor for heavy Higgs.

The last property we should measure is the Higgs 4-point coupling $\tilde{\lambda}$. This is equally important as measuring λ, because while $\lambda \neq 0$ allows global minimum to be away from zero, $\tilde{\lambda} > 0$ is required to keep potential bounded from below.

To have 4-point Higgs vertex, we must produce Higgs triplet. The rates for such an process are really small, so small that even at VLHC (Very Large Hadron Collider with energy 200 TeV) the cross section is only several fb, 3 orders of magnitude smaller than single Higgs production at LHC.

It is not hard to imagine that at LHC the rate would be microscopically small. Also, to find some channel which is observable and its rate is usable seems impossible. Note that ILC is out of game here - it just does not have enough energy in collision to produce Higgs triplet (it could be, theoretically, produced directly, but the rate would be practically zero). Finally, even if we would be able to measure 4-point Higgs coupling, we would not be able to exclude the non-SM

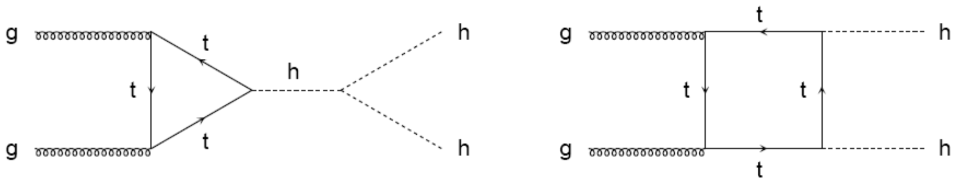

Figure 2.11: Feynman diagrams which show Higgs pair production. Note that they interfere destructively so that Higgs pair production is much smaller than single Higgs production. Figure originally from [28].

hypotheses as we did in case of 3-point coupling. The reason can be seen on Fig. 2.14: The variations coming from uncertainty on λ measurement are much bigger that the variations caused by change of 4-point coupling. Therefore, with our present knowledge and instrumentation we would not be able to obtain full picture of Higgs potential, even if we employ powerful devices of the future.

This section showed us that LHC can confirm several SM predictions about Higgs boson. It can measure its mass with good precision and tell whether it really is neutral scalar. Also it can measure Higgs couplings and in this way confirm that they are proportional to mass, but on this point we can get much more precise results from the ILC.

It was shown that the most difficult part is the measurement of Higgs 3- and 4-point interaction which is necessary to prove the existence of scalar potential which spontaneously break the SM. The difficulty is mostly in low rate of Higgs pair and triplet production and also in the final state which is really rich and therefore difficult to reconstruct. However we can quite convincingly exclude non-SM hypotheses for Higgs three point coupling. Nevertheless, in case of 4-point vertex we are not so successful and with present knowledge it seems that this parameter is not possible to measure even with the powerful machines of far future.

2.2.3 MSSM Higgs

Previous section showed, how would SM Higgs look like at LHC. However, it is quite possible that the Higgs sector would follow some SM extension, like SUSY. Some reasons were explained in the first chapter of this thesis.

There are many possible extensions of the SM, but here I will stick to SUSY, particularly to the MSSM. It predicts that there are two Higgs doublets: one which couple to down-type fermions and one which couple to up-type fermions. After the spontaneous symmetry breaking 3 degrees of freedom are gauged out to give masses to three gauge bosons, so that we are left with 5 physical states. These are two charged Higgs bosons ($H^{\pm}$), two CP-even neutral Higgses (H, h) and one CP-odd pseudoscalar A.

Each Higgs doublet has its own vacuum expectation value v_1 and v_2, respectively, but in practice we do not work with these but rather with their ratio denoted as $\tan\beta \equiv \frac{v_2}{v_1}$. Other parameters are Higgs bosons masses, but they are all related, so that there is only one mass is independent parameter. For historic reasons, the pseudoscalar mass M_A was chosen to be the second free parameter of MSSM Higgs sector (along with $\tan\beta$). The prescription how to calculate the rest of the masses from these two numbers is in [28]. They show one interesting property - for large M_A the masses of H, A and $H^{\pm}$ tend to be the same, while the mass of the lightest state h asymptotically converge to a limit dependent on $\tan\beta$. The graphic representation of this fact is on Fig. 2.15. We can see one remarkable feature of MSSM - that there is always at least one CP-even Higgs boson (i.e. SM like) in the region 90-145 GeV, i.e. in the same place as SM Higgs is highly expected. In most cases, it is the lighter h, but if the

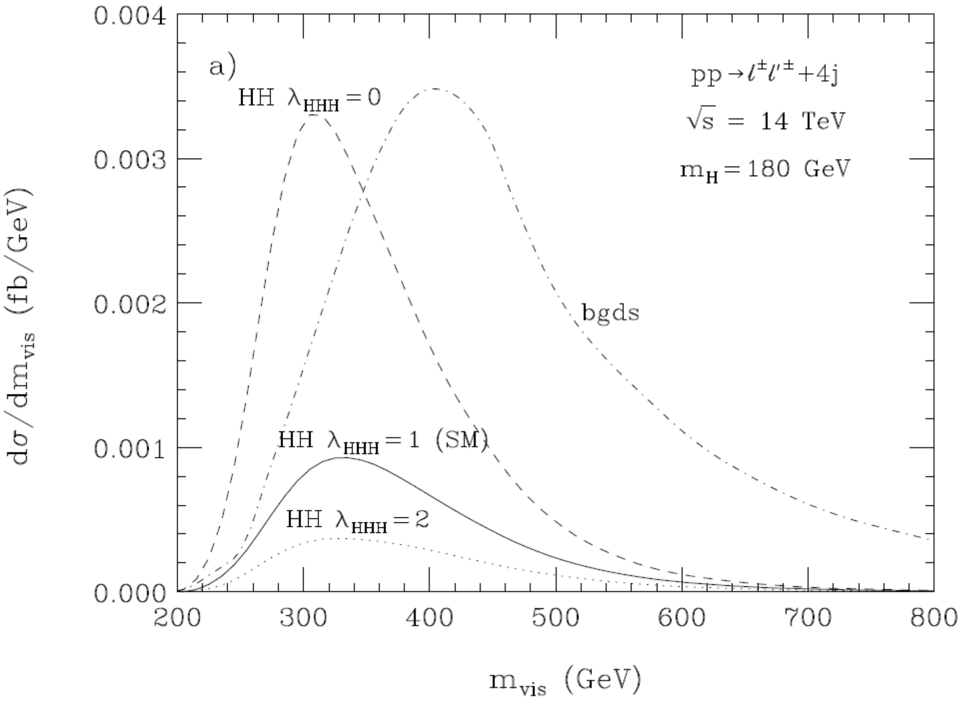

Figure 2.12: Distribution of visible invariant mass at LHC for 3 scenarios: No Higgs 3-point coupling, SM case and the case the 3-point coupling is doubled w.r.t. SM. Figure originally from [28].

pseudoscalar mass is low enough, it could be the heavier H.

Also, from M_A and $\tan\beta$ we can easily get values of couplings to gauge bosons and fermions. Example is on Fig. 2.16. We observe, that the behaviour of h and H is somehow complementary in a sense, that h has large gauge couplings for high M_A while H exactly the opposite. The same is true also for the fermion couplings. Lighter h has large coupling to up type fermions and small to down type fermions for large M_A and vice versa is true for H.

From figures 2.15 and 2.16 we can guess how will the branching ratios look like. These are on Fig. 2.17. We can see that it is pretty similar to the SM case (Fig. 2.3(b)), making it extremely challenging to decide between SM Higgs and CP-even MSSM Higgs. The only new features are decay of H into h or A pair which can bring interesting additional channels.

We also should care about the BR's of pseudoscalar Higgs boson A (Fig. 2.18). The pattern is much simpler, as coupling of pseudoscalar to gauge bosons is forbidden at tree level, so that we have mostly decays to fermion pairs (preferring the heaviest possible). If, however, the M_A is sufficiently large, we can observe decay to hZ, which might be more easily identifiable.

At last there are the branching ratios of charged Higgs. These are the simplest - they decay almost exclusively to tb or $\tau\nu$ if they are lighter.

Next ingredient we need to make conclusions about SUSY searches is the production rate. The channels for production of neutral Higgses are same as in the case of SM. Figure 2.19 shows the cross-section of gluon fusion. Comparing with Fig. 2.3 (a) we find, that the MSSM rate is almost the same as the SM rate for small $\tan\beta$, but is is becoming steeper as $\tan\beta$ increases. Cross section of pseudoscalar production has the same order of magnitude as the production of scalars, with notable difference around the top quark mass, where there is sharp peak in A cross section.

If we take in account that the BR's are also very similar to the SM we can say that for gluon

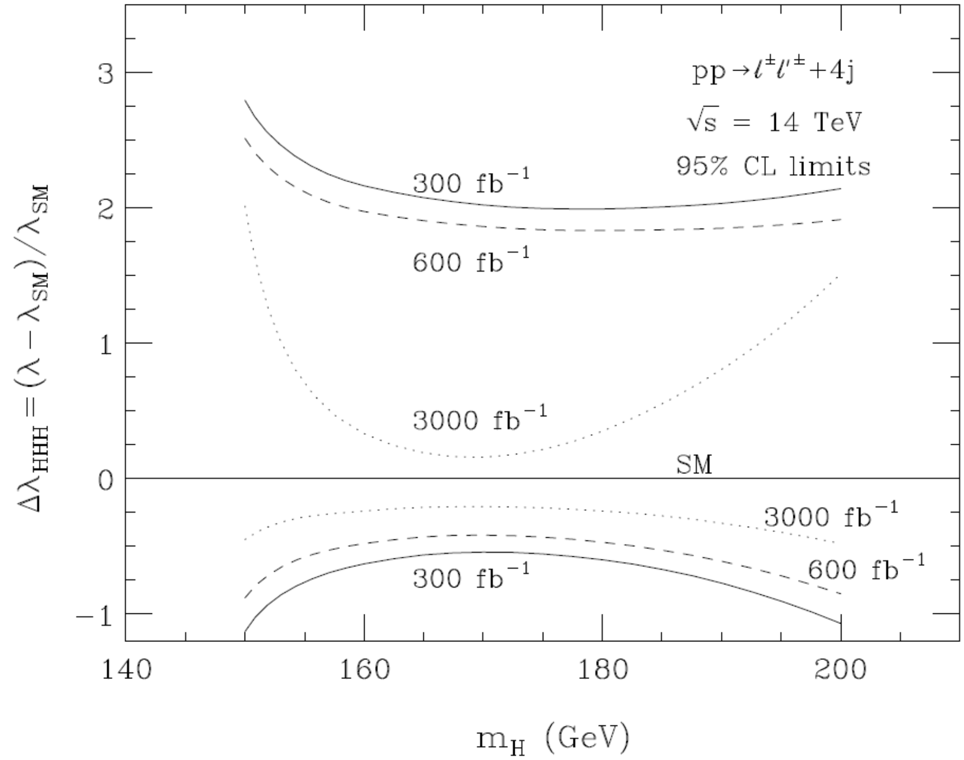

Figure 2.13: Borders of the exclusion regions for possible deviation form the SM value which is depicted as a solid horizontal line. Note that non-existence of Higgs 3-point coupling means that $\Delta\lambda_{HHH} = -1$. Figure originally from [28].

fusion the physical output will be practically same both for SM Higgs boson and MSSM H and h bosons.

SM case showed that more interesting than the gluon fusion is the WBF. The same is true also for MSSM. When we look back at Figs. 2.15 and 2.16, we can see that there is always at least one Higgs boson in accessible mass region with large enough coupling to the gauge boson. The WBF cross-section times branching ratio to τ is shown on Figure 2.20 both for h and H. This means that there will be always at least one CP-even state observable in WBF at LHC. If we are lucky enough, we can observe both of them.

What about other Higgs states? The searches for pseudoscalar A are mostly similar to the SM Higgs searches - with the exception that A do not couple to the gauge bosons. The only problem can be in the region of high M_A where H and A become practically degenerate. From Figs. 2.19 and 2.20 we can see that the production rate via gluon fusion and WBF is very small for H and A (here only gluon fusion applies as A cannot be produced in WBF), making their final states ($b\bar{b}$ and $\tau^+\tau^-$) unobservable.

However, some help comes from the new production channel - b quark associated production. It has reasonable rate due to enhancement of down-type fermion couplings in the region of high M_A. Thanks to this, both H and A mass is measurable with good precision over wide mass range. The new $b\bar{b}H/A$ channel can also be used to measuring the second MSSM parameter - $\tan\beta$, because its rate is proportional to $\tan^2\beta$.

Nevertheless, the key point in MSSM Higgs searches is the discovery of charged Higgs states, as it is the only way to directly prove the existence of two Higgs doublets. However, it is also the most difficult part.

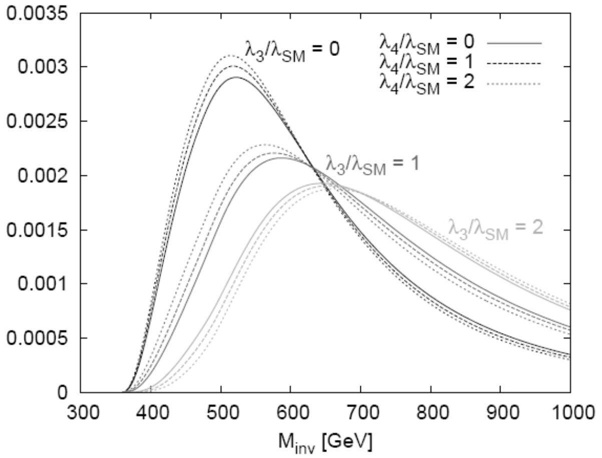

Figure 2.14: Differential cross section of Higgs triplet production normalized by the total cross section. We can see very strong dependence on Higgs 3-point coupling λ_3, while the differences between SM and non-SM predictions for λ_4 are microscopical. Figure originally from [28].

The best production process for charged Higgs is in a association with top quark due to large couplings. Ongoing are Tevatron searches which concentrate on low $H^{\pm}$ mass, as there is not much energy available for charged Higgs production. LHC will therefore concentrate on heavier $H^{\pm}$, having the mass larger than top quark.

The main problem is that decay to tb is useless, due to overwhelming QCD background, so that one must rely on decay to τ and ν which has BR only about 10 % and is not easy to properly reconstruct due to the appearance of neutrino. Thanks to this restriction, the charged Higgs production will be observable only for large $\tan\beta$ or small $M_{H^{\pm}}$ [28].

The summary of MSSM searches is on Fig. 2.21 which shows in M_A - $\tan\beta$ parameter space which Higgs states could be observable. We can see, that at least one CP-even state we can find in every case, but mostly we can discover also H and A. It also shows, that the discovery of charged Higgs states would be the most difficult.

2.3 Summary

This concludes the chapter on experimental methods of particle physics. We have seen, that the experimental validation mostly means statistical testing of several hypotheses and in an example we learned that the crucial part is the choice of the right observable which could than be used as discriminating variable.

Most place was devoted to the search for Higgs boson at LHC and to the measurement of its properties. We concentrated on the most promising discovery channels and found that LHC has very good capability to discover SM Higgs over wide mass range.

We also did a brief excursion to methods of measuring quantum numbers of the new particle and thus checking whether it really is SM Higgs. LHC should be able to prove that the new particle is really neutral scalar boson and measure its couplings to gauge bosons and fermions. Also it may be able to measure Higgs 3-point coupling, important prediction of the SSB. Nevertheless, it seems that we would not be able to measure 4-point Higgs coupling.

Last section outlined the phenomenology of MSSM Higgs sector. The key difference is existence of 5 physical states, but not all of them can be observable. We have seen, that the lightest of them, SM-like scalar boson h should be observable at any case. The other CP-even

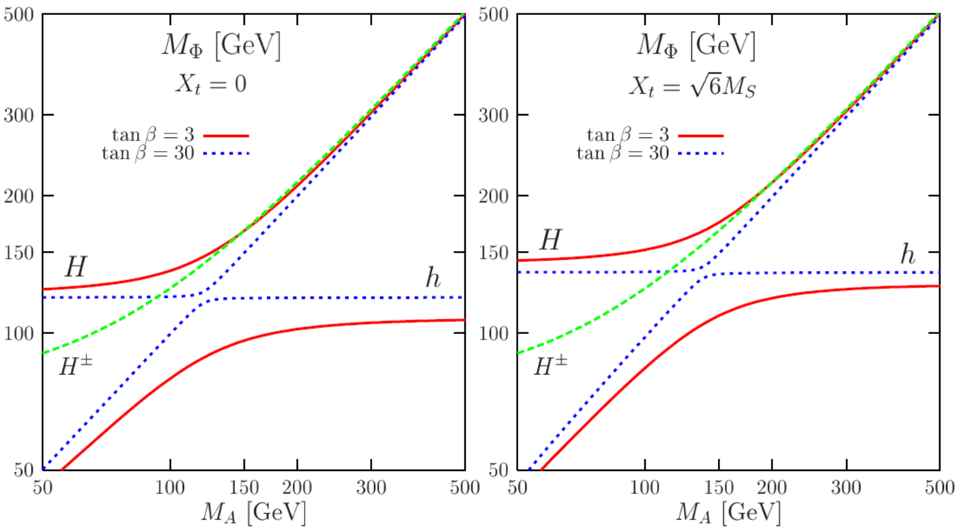

Figure 2.15: Two plots show how mass of Higgs scalars and charged Higgs pair depends on the pseudoscalar mass M_A. Left plot is for minimal mixing in top sector, while the right one is for maximal mixing. Figure originally from [28].

state H should be observable in most cases as well together with pseudoscalar A. The most difficult to observe is charged Higgs pair which, on the other hand, is the only way how to directly prove the existence of two Higgs doublets - main prediction of MSSM for energies below SUSY breaking.

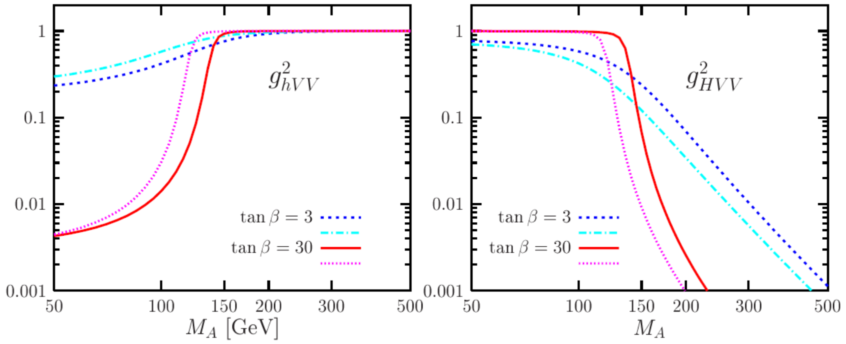

Figure 2.16: The size of coupling to the gauge bosons for lighter Higgs scalar h (left) and his heavier partner H (right plot). Maximal mixing in top sector denoted by darker colors, while the minimal mixing corresponds to lighter colors. Figure originally from [28].

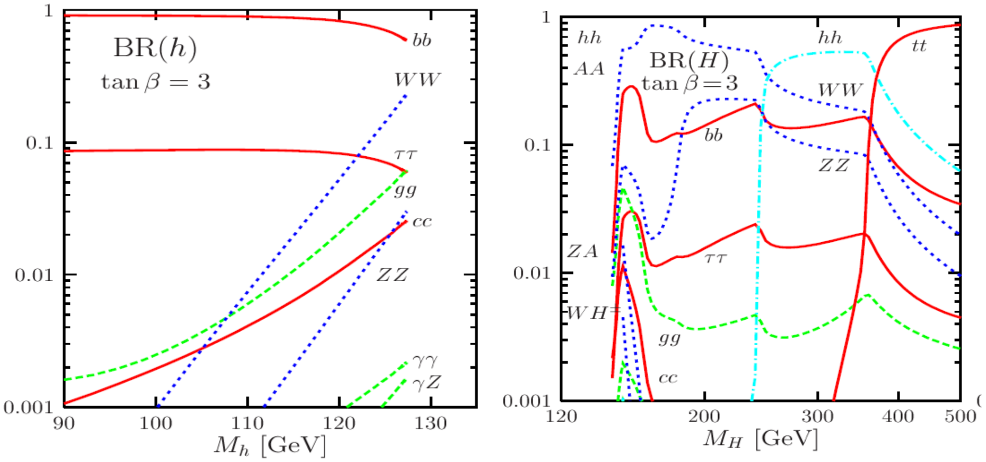

(a) h (b) H

Figure 2.17: Branching ratio of light MSSM scalar Higgs h (a) and for heavy MSSM scalar H at LHC, both as a function of their mass. Figure from [28].

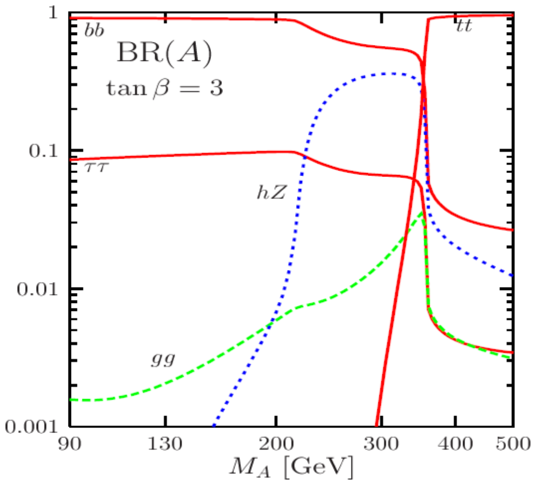

Figure 2.18: Branching ratio of MSSM pseudoscalar Higgs boson as a function of its mass. Figure originally from [28].

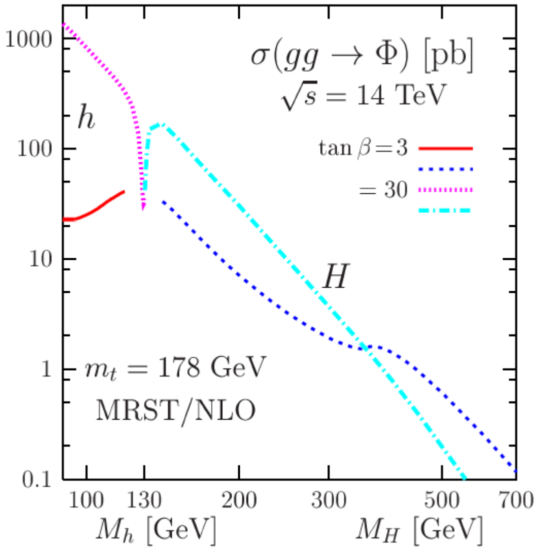

Figure 2.19: The cross section of production of scalar Higgses via gluon fusion. Left part is function of h mass and right is the function of H mass, using the fact, that according to MSSM M_H is always higher than m_h (cf. Fig. 2.15). Figure originally from [28].

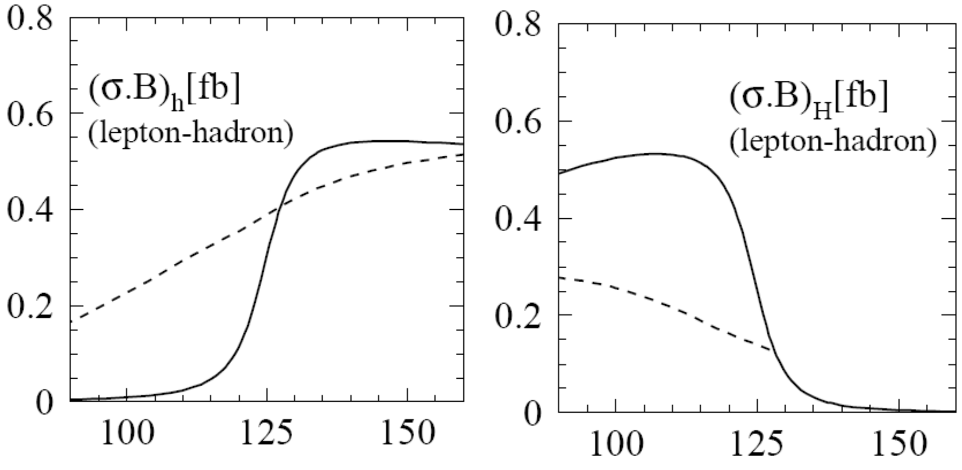

(a) h

(b) H

Figure 2.20: Cross section times branching ratio to the observable final state for both light h and heavy H. Figure from [28].

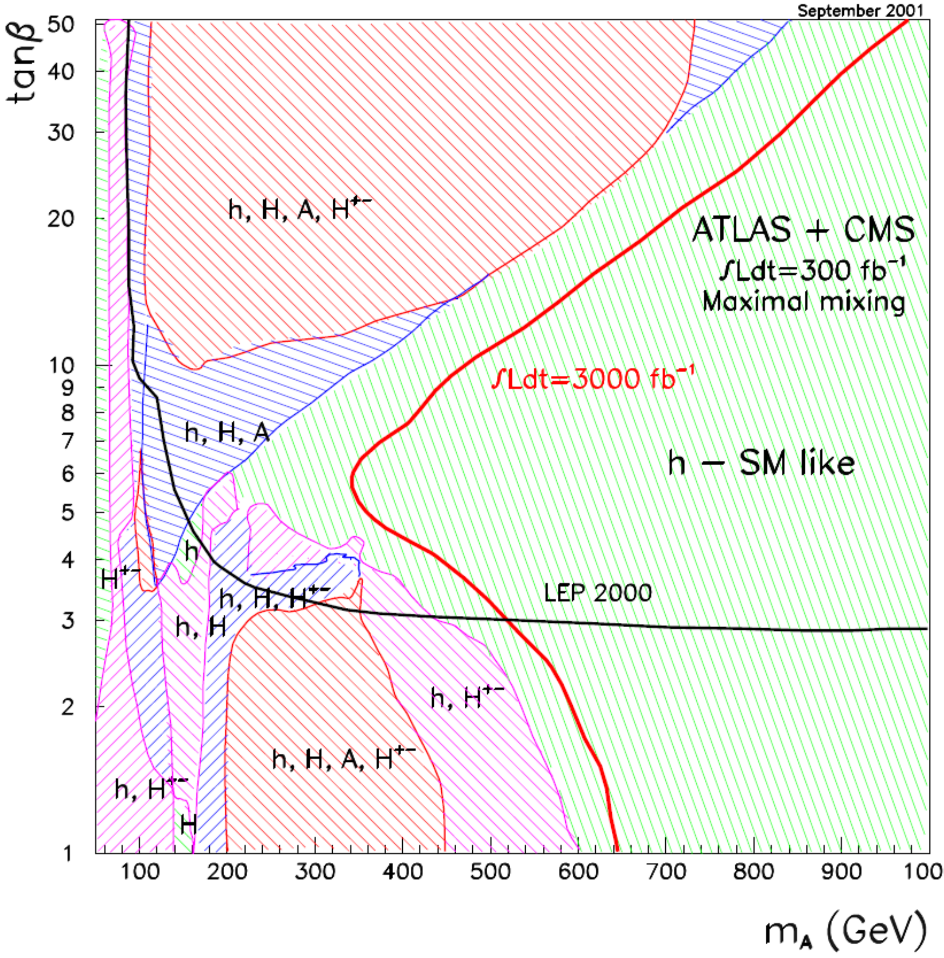

Figure 2.21: Summary of the MSSM discovery possibilities on the LHC (combined data from ATLAS and CMS) in M_A-tan β parameter space. It also shows how big should be improvement brought by LHC upgrade to SLHC. The discovery is defined as at least 5σ statistical significance in at least one channel. Area excluded by LEP is below the solid black line. Figure originally from [28].

Chapter 3

Experiment ATLAS

3.1 ATLAS in the context of current and future experiments

Since 1940s the main devices for studying particle properties have been the particle accelerators, as they can provide very high energy and particle density. Also, they are better controllable than cosmic rays or radioactive decay. The first accelerators had energy of several MeV's, but since then, they have grown in power and current most powerful particle accelerator (Tevatron at FNL, USA) can achieve collision energy of about 2 TeV. Nevertheless, in a few months even larger collider will be started at CERN, Switzerland: LHC with the collision energy of 14 TeV.

LHC has not only the biggest energy, it is also designed to have unprecedented luminosity of beam (10^{34} $\mathrm{cm}^{-2} \cdot \mathrm{s}^{-1}$), about hundred times the luminosity of Tevatron. In about ten years the upgrade to SuperLHC (SLHC) is planned. SLHC will have luminosity of about about ten times higher than LHC.[1]

The proton beams at LHC will be composed of numerous bunches (each containing about 10^{11} protons) separated by 25 ns, resulting in bunch crossing rate of 40 MHz. At full luminosity, we should obtain about 23 proton-proton collisions for each bunch crossing. However, during the initial running (luminosity $10^{31} - 10^{32}$ $\mathrm{cm}^{-2} \cdot \mathrm{s}^{-1}$) we should have only about 1 collision per bunch crossing. The main parameters of the accelerator are summarized in Table 3.1.

The beams for the LHC will be prepared in older CERN accelerators (PS and SPS) and injected inside LHC with the energy of 450 GeV - see Fig. 3.1 for the schematic view of the CERN accelerator chain.

Apart from protons, LHC is designed to accelerate also the nuclei of heavy elements such as Pb. The collision energy will be then 1150 TeV. These will be used typically one month a year and will allow study of the hot and dense matter. ALICE is specially designed to study heavy-ions collisions, but other detectors can also do some measurements.

The LHC is being built in the tunnel which previously hosted the LEP accelerator and is nearing its completion. As of May 2008, the whole accelerator is assembled and is being cooled to the operating temperature of about 2K. Also, the pressure is being lowered, so that at the end there will be less pressure inside LHC than in the outer space. The status of work can be checked at [31].

It is expected that the cooling will have finished by the middle of June, and the first injections can start at the end of June [32]. It is not firmly decided yet, but it is very probable, that the first physics run (expected in August) will be at 10 TeV and only after that the energy will be gradually increased to the nominal value.

Along the course of the accelerator ring, there are four big detectors which measure the

---

[1] The exact number is still subject of discussions. It is also possible, that the beam energy will be increased to about 10 TeV, giving 20 TeV in collisions.

Table 3.1: LHC parameters

particles used	protons and heavy ions (Pb^{82+})
circumference	26.659 m
injected beam energy	450 GeV (protons)
beam energy at collision	7 TeV
magnetic field at 7 TeV	8.33 Tesla
beam luminosity	10^{34} cm^{-2}s^{-1}
integrated luminosity/year	100 fb^{-1}
protons per bunch	10^{11}
operating temperature	1.9 K
revolution frequency	11.2455 kHz
power consumption	120 MW
energy stored per beam	362 MJ
energy stored in magnets	11 GJ

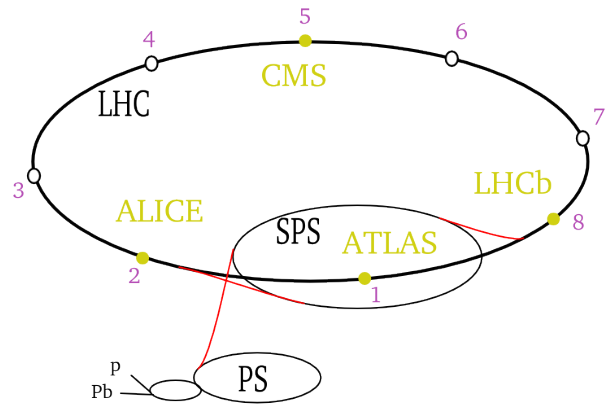

Figure 3.1: The scheme of the CERN accelerator chain together with location of LHC experiments. Figure from [33]

outcome of the collisions. These include 2 specialized detectors (ALICE, LHCb) and two general purpose experiments (ATLAS, CMS). The latter have no specific task, but are rather aimed at detecting as much as possible and so study the physics at the energy which has not been accessible before. Here is the brief description of LHC experiments:

ALICE (**A** **L**arge **I**on **C**ollider **E**xperiment) is a detector specially designed to study the collisions of heavy ions. Experiments in the CERN in 1990's and in the Brookhaven National Laboratory in 2000's showed that at very high temperatures the quarks are probably not confined inside hadrons but they are are rather free in a state which was called the quark-gluon plasma (QGP). It is expected that this state of matter exists naturally inside the quasars and that it was also one of the initial stages of the Universe.

The LHC should create the quark-gluon plasma by colliding nuclei of lead with an energy of 5.5 TeV per nucleon. The QGP will be then identified thanks to the specific signatures of escaping particles - for example the abundance of strange particles and the suppression of the production of J/ψ mesons (made from charm and anticharm pair of quarks) or Υ ($b\bar{b}$), because the turmoil of QGP prevents forming of heavy quark pairs.

ALICE is being constructed at Point 2 and its collaboration involves more than 1000 people from 28 countries.

LHCb (**L**arge **H**adron **C**ollider **b**eauty) is an experiment devoted to the measurement of CP violation, especially in the B mesons decay. It is expected that it could be most clearly seen in the difference between the decay of B_d meson ($d\bar{b}$) to J/ψ ($c\bar{c}$) and K^0 ($d\bar{s}$) and the decay of $\overline{B_d}$ meson to respective antiparticles. By studying the difference in the decay times, we would be able to determine the complex phase of CKM matrix [3].

The CP violation in the charged and neutral B meson system has been recently observed at BaBar and Belle [6], however, their statistics is not large enough to make precise measurement of the CP violating phase of the CKM matrix. It is expected that LHCb will be able to measure it more precisely.

The LHCb is located at Point 8. This experiment has nearly 900 participants from 13 countries.

CMS (**C**ompact **M**uon **S**olenoid) is one of the two general purpose detectors at LHC. The name "compact" means that it is somewhat smaller than ATLAS (about 8 times in volume), but has about twice its weight. It is being built at Point 5 (cf. Fig. 3.1) - unlike ATLAS it was assembled on the surface and lowered to the experimental cavern afterwards. The name also signalizes that CMS is optimized for tracking muons. Its magnet will be the largest solenoid ever built, producing a magnetic field of the strength of 4 Tesla. The CMS collaboration involves about 2000 scientists and engineers from 36 countries. The scientific goals of the CMS are similar to that of ATLAS, namely

- The search for origin of the spontaneous symmetry breaking (Higgs boson)
- The search for physics beyond the SM - for example supersymmetric particles
- The study of heavy ion collisions and of the formation of the quark-gluon plasma, emulating thus the very first moments after the Big Bang

Although the construction of two similar detectors may seem as a waste of time and money, it fulfils the natural requirement on experimental physics - that any result should be independently confirmed. Also, thanks to the combined statistics from both experiments, we can reduce systematic as well as random errors, as we have seen in the section on measurement of Higgs properties.

ATLAS (**A** **T**oroidal **L**HC **A**pparatu**S**) is a general purpose detector designed to exploit the full LHC potential. It is being built at Point 1 (see Fig. 3.1). The project involves collaboration of more than 1800 scientists and engineers from 34 countries. Although ATLAS's main task is to search for the origin of spontaneous symmetry breaking in the electroweak sector of the SM, it is designed to measure the broadest possible range of signals. Because of unprecedented energy and collision rate of the LHC, the ATLAS will be larger and more complex than any other detector. The main lines of the ATLAS research are:

- The search for the Higgs boson or any other mechanism of the electroweak symmetry breaking
- The investigation of CP violation in B-decays
- The precise measurement of mass of heavy particles like top quark or W boson
- The search for supersymmetric particles or any other new models of physics
- The studies of compositeness of fundamental fermions

	ATLAS	CMS
Tracker	$\|\eta\| < 2.5$, B=2T	$\|\eta\| < 2.5$, B=4T
	Silicon pixels and strips TRT - e/π identification	Silicon pixels and strips no particle identification
Calorimeter	$\|\eta\| < 5$	$\|\eta\| < 5$
electromagnetic	Pb-Liquid Ar	$PbWO_4$
hadronic	Fe/scintillator (center) and W-LAr (fwd)	brass/scintillator (center) and Fe/Quartz (fwd)
Muon spectrometer	$\|\eta\| < 2.7$	$\|\eta\| < 2.5$
	air-core toroids with muon chambers	return yoke of solenoid instrumented with muon chambers

Table 3.2: Comparison of the ATLAS and CMS detectors.

> To fulfil these goals the ATLAS consists of several components which together provide as much information about the collision as possible. The whole experiment will be described in detail in the next section.

Not listed here are two smaller experiments which do not have their own experimental hall. The CMS hosts experiment TOTEM, which is aimed at measurement of total cross section, elastic scattering and diffractive processes at the LHC. It will consist of Roman pots and other forward detectors which can detect particles that have such small transverse momentum that they cannot be caught by CMS.

Similar kind of experiment is LHCf (LHC forward) which is installed 140 m in front of and behind ATLAS. Like TOTEM it will measure mostly particles with large (pseudo)rapidity which escape from the ATLAS undetected.

As was indicated, ATLAS and CMS are very similar experiments - the main purpose is to gather data twice as fast as with single detector. Also, different technology can ensure independent measurement: if we observe some kind of events only on one detector (although it should be visible on both), it can signal some problem with the detector. Thanks to the slightly different design, each of the detectors is efficient in observing other type of events - for example, precise CMS calorimetry allows it to observe $H \to \gamma\gamma$ with better resolution than ATLAS, while the latter has much better b-tagging efficiency. The main construction differences are summarized in table 3.2.

ATLAS and CMS can be compared to CDF and D0 - two general purpose detectors at Tevatron which are also complementary to each other and together they gather data faster than single detector. The same pattern could have been seen also at LEP with its four general purpose experiments that acted in nice accord and together verified the Standard Model up to a few permille [11].

The results from ATLAS (and LHC as whole) would be also vital input for the future experiments, notably the ILC - future project of powerful linear electron-positron collider. It is supposed to provide very precise measurements of the properties of the particles discovered by LHC that will also provide some knowledge about the particle properties, so that ILC will know where to look.

3.2 Detector description

The structure of ATLAS resembles onion: it is composed of several layers of different subdetectors which lie on top of each other. They will be described in detail in next sections. The complete view of this detector can be seen of Fig. 3.2. The innermost part is the Inner Detector, which itself is composed of three other subsystems (Pixel, SCT and TRT). Its purpose is to measure track of charged particles (using semiconductor trackers and drift tubes) and also tell charged leptons from hadrons (i.e. mostly discriminate between electrons and pions). Inner Detector is contained in a cylindrical solenoid whose magnetic field bend tracks of charged particles, allowing the measurement of charge and momentum.

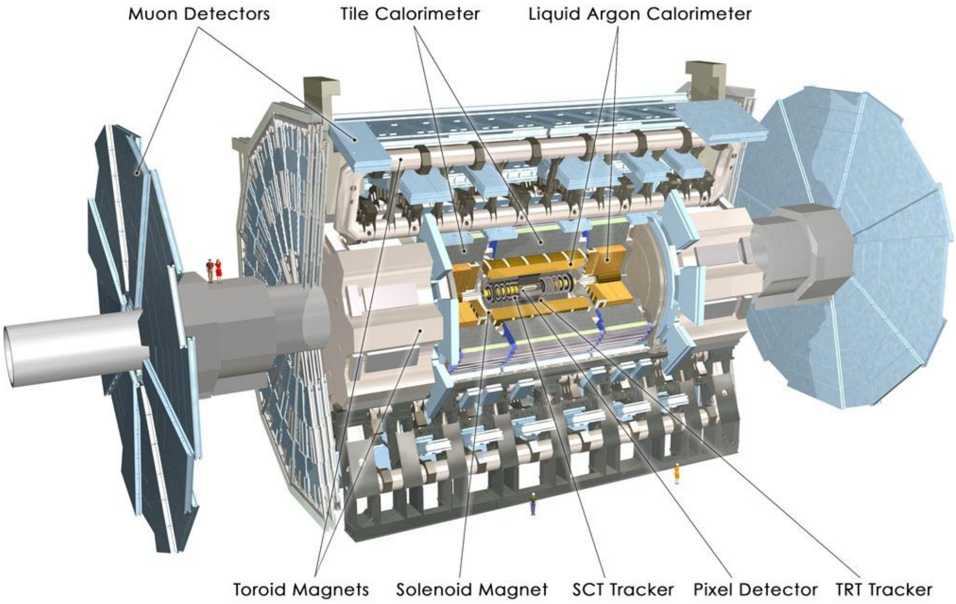

Figure 3.2: Overall view of the detector ATLAS. Several human figures are displayed there to show the scale of the detector. Figure from [38].

The middle part of ATLAS is formed of calorimeter system. It is composed of electromagnetic calorimeter, which captures leptons and photons, and from hadronic calorimeter which should capture practically all hadrons and jets escaping from the center of the detector. The calorimeters have very large pseudorapidity coverage allowing the detection of most particles.

Around calorimeters there are eight big toroidal magnets with air core which create magnetic field to bend highly energetic muons which can escape from calorimeters. These are detected in muon chambers which are assembled on top of the toroid magnets. There are also muon wheels in the front and in the back of ATLAS. The only SM particle which cannot be detect directly at ATLAS is neutrino which can be spotted only from missing transverse energy. However, if we go beyond the SM we find other particles which escapes further detection, notably the lightest SUSY particle, invisible Higgs [40] and many others. The scheme of particle identification at ATLAS is at Fig. 3.3. Next sections will introduce ATLAS subsystems in greater detail.

3.2.1 Pixel Detector

The innermost part of the Inner Detector is the Pixel Detector. Its detailed view is on Figure 3.4. We can see, that it has three cylindrical layers in the "barrel" area and 3 disks in each "endcap".

The layers are labeled as B-layer (it has radius 5.05 cm), Layer 1 ($r = 8.85$ cm) and Layer 2 ($r = 12.25$ cm). The barrel part is 80.1 cm long. The three disks are located 49.5 cm, 58 cm and 65 cm away from the center of the detector. Their inner radius is 9 cm and outer 15 cm.

Each layer can further be divided into ladders which are essentially 13 modules with the same ϕ coordinate. The modules on the same ladder are labeled form -6 to 6, i.e. module number 0

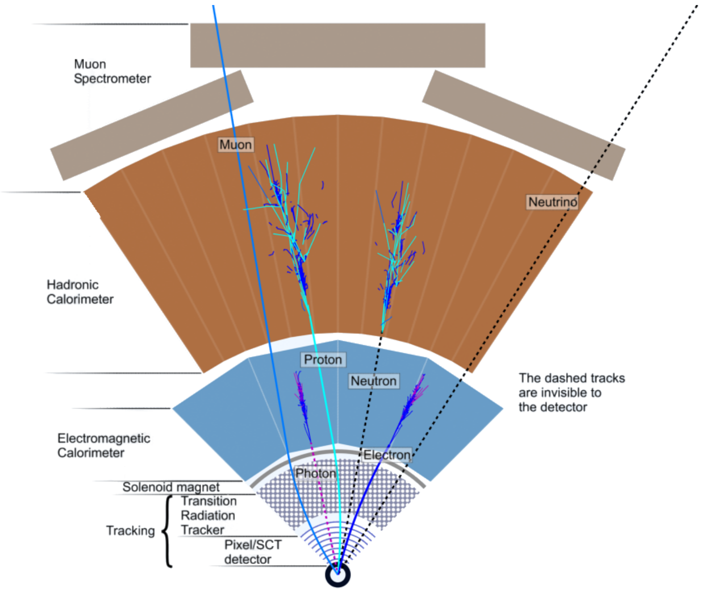

Figure 3.3: Scheme of particle identification in ATLAS. Charged particles are detected in the Inner Detector, and the curvature of their tracks can be used to measure the charge. Most photons and leptons are captured by the electromagnetic calorimeter, hadrons are stopped at hadron calorimeter. High energy muons leave hits in muon spectrometer and neutrinos can be detected only from missing energy. Figure from [38].

is just around the interaction point and the modules 6 and -6 respectively are on the edges of the barrel. The numbers of ladders at each layer are 22, 38 and 52 respectively.

On the disks the modules are arranged like a fan (cf. Fig. 3.4). Every disk is divided into 8 sectors with 6 modules at each of them. So that there are 1744 pixel modules altogether: 288 on the endcap disks and 1456 on the barrel layers. On both barrel and endcaps, the modules overlap to assure that the detector is hermetic with respect to outgoing particles[2].

One pixel module is about 6 cm long and 2 cm wide. There is an array of 47 232 pixels on it which are arranged to 144 rows and 328 columns. Each pixel has size $50 \times 400\ \mu$m. The read out is done by 16 chips, each serving an area of 18×160 pixels. Because the pixels are arranged to form a two-dimensional field, they can offer extremely precise measurement of two coordinates of the track. The third coordinate is of course the module location which is, ironically, known with much less precision[3] than the pixels are able to achieve: cf. Tab. 3.3.

The Pixel Detector is constructed to be as close to the interaction point as possible and to give extremely precise measurements of the tracks and the vertex positions. The usual charged particle will leave 3 hits in the detector (if it is not heavy enough to decay before it reaches the first layer), but for example cosmic muon (see chapter 4) can leave much more hits, because it can go through the detector from top to bottom. Also, because cosmic muons are often approaching the Pixel Detector from tangent, rather than by perpendicular direction, it is much more probable that the cosmic muon will hit adjacent pixel modules in the same layer (more details are given in section 4.2.2).

---

[2] This is not completely true. There are known to be tiny 'holes' in the overlap regions. Also, not all modules have overlap.

[3] This is the current status, but out knowledge of the module positions ('alignment') will get better over the time as we collect more data.

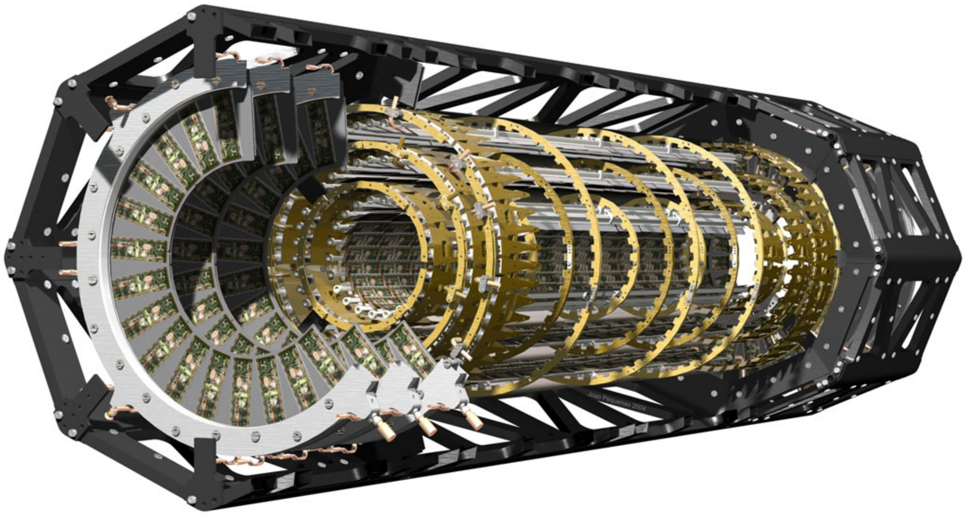

Figure 3.4: View of the inside of the Pixel Detector. Three forward endcap disks are clearly visible as well as overlapping modules in the barrel layers. Figure from [38].

3.2.2 SCT

The Semiconductor Tracker is designed very similarly to the Pixel Detector, but instead of pixels it uses the silicon strips for detection. So that the main difference is that active parts of SCT form an one-dimensional array, i.e. SCT are very precise in the ϕ direction, but less precise in the z coordinate (along the beam axis). Look in the Table 3.3 for details.

There are 2 active layers on each SCT module so that the small difference in r coordinate of both layers allows us to measure particles's z coordinate.

3.2.3 TRT

Transition Radiation Tracker is the last (and largest) part of the Inner detector. It is built from the straw detectors, whose diameters are 4 mm. The central wire in each of them has 30 μm in diameter. In the barrel, the straws are 144 cm long, in the endcap they are a bit smaller.

TRT detects the transition radiation photons which were created by passing highly energetic particles and so it can distinguish between the electrons and hadrons (typically pions) because each creates a different number of these photons.

Unlike semiconductor detectors (e.g SCT or Pixel Detector), the straws in TRT are relatively cheap and traversing particle does not lose too much energy. The TRT can give about 36 hits for the average particle.

3.2.4 Calorimeter

The primary purpose of the calorimeter system is to measure the energy of particle. It is very dense and usually makes the particle stop in the calorimeter and therefore deposit all its energy there in a form of electromagnetic or hadronic shower.

ATLAS calorimeter consists of two different parts in terms of material composition. The first one is the Liquid Argon calorimeter (LAr). It has three parts: electromagnetic calorimeter, hadronic calorimeter and forward calorimeter. The EM calorimeter is made from accordion shaped lead electrodes which have liquid argon between them. It is both in the barrel and in the endcaps (cf. Fig. 3.5).

Table 3.3: Inner Detector Subsystem parameters

System	Element size	Resolution	η coverage
Pixels	50 × 400 μm	$\sigma_{R\phi} = 14\ \mu$m $\sigma_z = 87\ \mu$m $\sigma_R = 87\ \mu$m	± 2.5
SCT	75 or 112.5 μm × 12 cm	$\sigma_{R\phi} = 15\ \mu$m $\sigma_z = 770\ \mu$m	± 2.5
TRT	4 mm diameter 150 cm long	$\sigma_{R\phi} = 170\ \mu$m	± 2.5

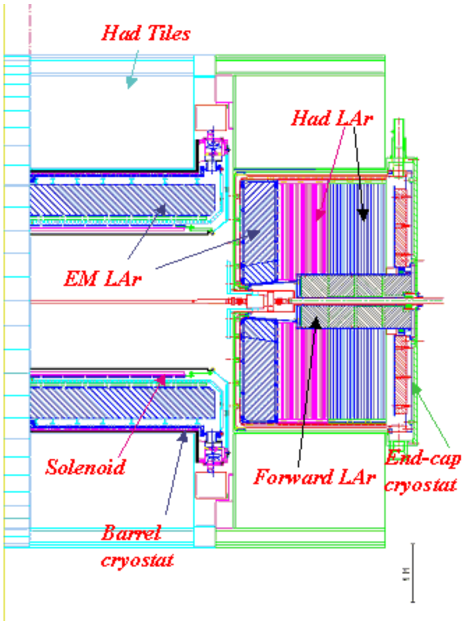

Figure 3.5: Schema of the ATLAS calorimeter system. Figure shows both Liquid Argon (LAr) and Tile Calorimeter. From the functional point of view, we can see both electromagnetic (EM) and hadronic calorimeter. Forward calorimeter should capture leptons, photons and hadrons with large pseudorapidity. Figure from [38].

Hadronic LAr calorimeter is in the endcaps and uses copper plates in liquid argon to stop hadrons. Forward calorimeter is located very close to the beampipe to cover particles with large pseudorapidity. It is made of copper and tungsten.

Second part of ATLAS calorimeter is the Tile Calorimeter that makes use of steel as the absorber material and scintillating plates read out by wavelength shifting (WLS) fibres as the active medium. The calorimeter has quite high granularity - it consists of towers which have size 0.1 × 0.1 in $\Delta\eta$ and $\Delta\phi$. It has also very quick response which makes it ideal trigger device.

3.2.5 Muon Chambers

The only detectable particles which may traverse through the whole ATLAS are muons. They can be energetic enough not to be stopped by the calorimeters and also have sufficiently long lifetime not to decay inside the detector. Therefore, there is an outer envelope of muon spectrometers which measures their momenta with high precision. This is very important, because typical trigger for hadronic collider like LHC would often include the existence of at least one high-energetic muon. The precise measurement of their momenta helps to reconstruct the mass of particle from which they originated - this could be for example the Higgs boson. [4]

In the barrel region ($|\eta| < 1$) there are three layers of muon chambers consisting of precise Monitored Drift Tubes (similar to the TRT from the Inner Detector) and fast Resistive Plate Chambers (RPC) used for triggering. In the endcap regions, these detectors are placed vertically, also in three layers. There are, apart from the already mentioned MDT, Thin Gas Chambers, which are also used for triggering. In the regions with high pseudorapidity (i.e. high particle flux), the MDT are replaced by Cathode Strip Chambers which are more radiation tolerant.

3.2.6 Magnets

The whole ATLAS is set in a very strong magnetic fields which is used to bend the tracks of charged particles. The field is generated by two systems of magnets. The first one is solenoid magnet which is located between the Inner Detector and the Calorimeters. It generates field of 2T.

The second system are Toroid magnets which are on the perimeter of the whole ATLAS detector, together with the muon chambers. Barrel Toroid (8 coils with air core) is designed to provide 3.9 T. The Endcap Toroids are essentially large cryostats and should provide a field of 4.1 T.

3.3 ATLAS Trigger

When running at the full luminosity, there will be a bunch crossing every 25 ns and each crossing will bring approx. 20 of pp collisions. Not only that such a huge flux of information (about 10^9 Hz) is impossible to store and analyze, but only very few collisions will be interesting, because most of them will be ordinary low energy SM processes.

In fact, the ATLAS physics programme is like looking for a needle in a haystack. To be successful in this task, ATLAS employs a three level trigger to choose the potentially interesting events. This means that trigger job is to select the bunch crossing with the interesting event. That is not a trivial task - for example the next bunch crossing happens before the photons from the previous one are able to reach the edge of the detector.

The level one trigger uses only a very limited subset of information obtained from the calorimeter and the muon chambers (RPC and TGC). But that is enough to make a choice, because in ATLAS we are interested in events with massive particles (100 GeV and more) which quite often decay into leptons. The selection is based on direction, transverse momentum and energy sums, so that L1 typically selects high p_T leptons, hadrons or jets.

L1 trigger needs about 2 μs (compare to 25 ns, which is the time separating the bunches) to reach its decision and then the information is passed to the level 2 trigger. It uses full information from the detectors, but only from the regions selected by the L1 trigger - so called Regions of Interest (cf. Fig. 3.6). The L2 Trigger lowers the data flux to approx. 1 kHz.

The level 3 trigger finally channels the information from the detectors to the permanent data storage. But before that it further filters the events selected by the L2 trigger using all information from all detectors. At this stage rather complicated selection criteria of the offline analysis can be applied. L3 trigger also does the event building. This means it collects the pieces of information connected to one event from various detectors and puts them into a single memory. Each event then has size approximately 1 MB. The writing to the permanent data

---

[4] We know that direct exclusive decay $H \to \mu^+\mu^-$ is quite rare, but on the other hand, the muons can be decay products of Higgs decay products, e.g. $H \to ZZ \to \mu\mu\mu\mu$.

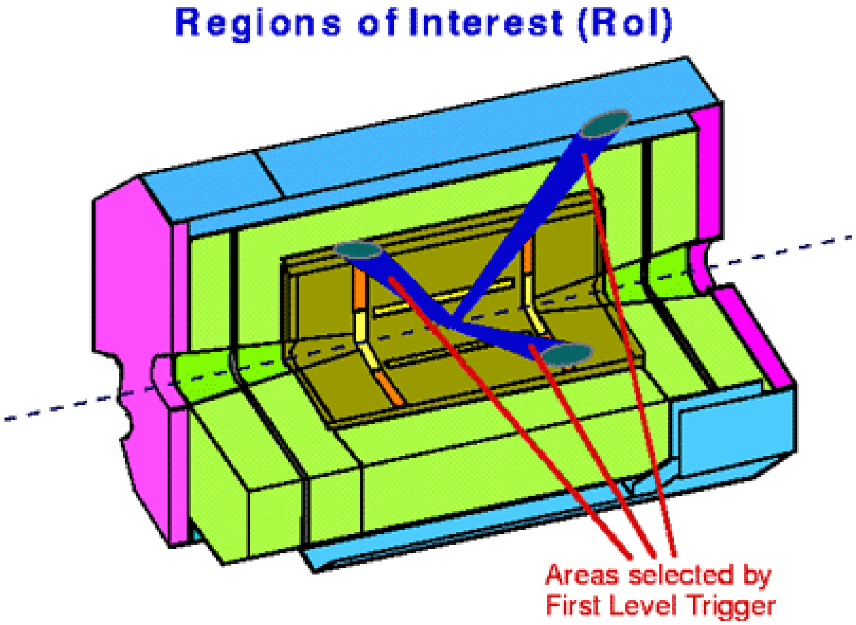

Figure 3.6: Example how the Regions of interest selected by L1 Trigger may look like. Figure from [38].

storage is done with frequency of about 100 Hz, more than million times lower than the initial information flux.

3.4 ATLAS computing

3.4.1 Athena

Last chapter showed that the amount of data coming from the experiment is tremendous, impossible to handle without computers. The software which runs during the data taking is called online software. Its task is to select data (trigger), store it properly (DAQ - data acquisition), control the hardware and the common infrastructure like cooling or electricity distribution (DCS - Detector Control System), do online monitoring etc.

In contrast to it, there is the offline software, which could be run whenever and wherever needed. It includes various algorithms for reconstruction of the tracks from the data, and also for analyzing and visualizing them. The software for event generation and particle simulation is rated among the offline software too. All parts of offline software will be discussed in more detail later in this section.

Because there are hundreds or thousands of physicists willing to analyze data from ATLAS, the collaboration would be impossible if each of them uses his own algorithm, not to mention that most of them are not experts on programming.

On the other hand, if there would be just one programme (e.g. MS ATLAS Analysis®), there would be no need for having different physics teams because everyone would have identical results.

Possible solution to this problem is the introduction of a software framework. This means, that there is a set of common methods and data types which are then used to construct more sophisticated algorithms. If the pool of common tools is robust enough, everyone can build algorithms which perfectly suit her or his needs and in the same moment, this algorithm is understandable to all other members of the collaboration. Moreover, the software framework encourages the common approach and reusability of the code.

In the case of the ATLAS experiment, there is an offline software framework called Athena. It is based on C++ and therefore it is object oriented. It encompasses not only the reconstruction and analysis algorithms needed for the ATLAS data, but also all other software needed for the HEP computing. The software can be divided into 5 sections, but the distinction is not always perfectly clear. Together they form a software chain which is depicted on Fig. 3.7.

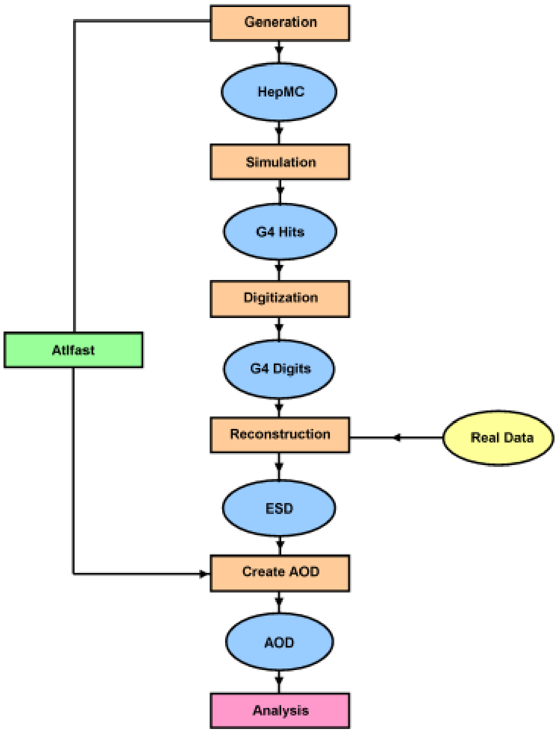

Figure 3.7: Diagram of the Athena full software chain. Figure from [42].

Generators The primary task of a generator is to create an output (list of outgoing particles, their position and momenta) of some physical process if we know the initial conditions. For example we have colliding electron and positron at center of mass energy 100 GeV and we would like to know what can emerge from this reaction when we would repeat the collision a lot of times. The ideal way to do this is to use some Monte Carlo generator. Naturally, this machinery can be used also for more complex events, like hadron collisions, because the parton distribution functions are basically only other probabilistic distributions. It is obvious that the accuracy of the generator is highly dependent on our knowledge of the underlying physics.

Simulation The input of a simulator is some Lorentz 4-vector, describing initial state of a particle, and the geometry of the event (e.g. the shape and material composition of the detector). The output is a hit collection, i.e. a set of all hits (a particle coming through an active detector volume) in the various parts of the detector together with information like deposited energy, incoming direction etc.

The most widely used simulation program is Geant4, which is also incorporated into the Athena. The quality of simulator is critically dependent on the quality of input data, especially the accuracy of geometry model. It has to have granularity large enough to be realistic, but on the other hand it cannot be too much detailed, because of the computing time it would take.

Digitization The tasks of this algorithm is to take the set of hits and assign to it the response of the detector we would get, provided those hits actually had happened in the detector. In some way it is natural extension of the simulators and indeed, digitization is mostly done by the same programs as simulation.

The digitization also takes into account the imperfection of and finite resolution of detectors. Also, it cares for the production irregularities like the "noisy" and "dead" pixels which are included in the digitization of the Pixel Detector.

As it was stated above, the output of digitization is technically identical to the output of detectors. Therefore the digitized data are ideal to test our computing system if it is able to handle the real data from ATLAS.

Also, the digitization of the generated events has another important purpose: by comparing the digitized and real data we may test the quality of our generators and simulators. Usually, also the "MC truth" (the data from generator) are stored with the digitized data for reference. The output files from digitization are called RDO (raw data object).

Reconstruction As was mentioned earlier, the main task of the reconstruction is to take the digital signal from detector, find hits and then try to fit a track through them. There are several reconstruction algorithms and in the Athena user can choose which of them would be good to use.

Reconstruction does the preliminary identification of final particles too (based on information from detectors like TRT or muon chambers) and creates objects like electron container (where it stores electron candidates), photon container etc.. Reconstruction also saves all reconstructed tracks, vertices, jets and missing transverse energy. The output is stored in ESD (event summary data) and AOD (analysis object data). The latter is more compact and is meant to be used for physical analysis, while the first is detailed description of the event. The event model is designed so that user can back-track form AOD to appropriate ESD if needed.

Other type of output file produced during reconstruction is so-called TAG file, very small (1 kb) summary of the event, which can be used in pre-analysis event selection.

These were “standard” reconstruction outputs, nevertheless, user can also order the creation of a more specific output called Combined Ntuple (CBNT) which contains all relevant tracking information that can be extracted via simple lines of code in ROOT (see later).

User can also ask the reconstruction algorithm to directly produce histograms he needs so that he can quickly check the reconstruction performance. This is the case of monitoring.

Analysis The last part of the offline software chain is the physics analysis. In contrary to the reconstruction algorithms which have to be certified by ATLAS physics convenors, analysis algorithm can be written by any user. The purpose of it is to take the information from the reconstruction and find what actually happened - for example by plotting the invariant mass of the muon pair in the $Z \to \mu\mu$ events, user will find gaussian peak, centered on the Z mass - this way a mass of the unstable particles can be measured.

Nevertheless, if it would be so easy, there would be no need for particle physicist and everything could be done by programmers. The physical insight is necessary the at moment we come across something we have not seen before and therefore something completely unknown to our algorithms. In this moment, the physicist has to decide which events contain the "new physics", which observables are good to plot (obviously, he has to understand what they mean). Finally, he or she has to interpret the result.

Important part of the analysis is also the visualization of the data. This could be done essentially in two ways - first is to visualize the whole statistics in form of various histograms, cuts, fits etc. Favourite tool for this is ROOT, which will be dealt with later in this chapter.

The second approach is to visualize single event by drawing all tracks and hits that were reconstructed in that event. This helps us to decide almost instantly whether some event was interesting or not. In case of ATLAS this job is done by Atlantis.

Atlantis is a stand-alone event display. Unlike the Athena it could run on many platforms including Windows or Sun. The only thing it needs is functional Java.

If a user wants to use Atlantis to view the events, he just turns on production of so-called jiveXML files in jobOption file (see below). These are then produced during reconstruction or analysis on top of the standard output. The XML files can than be easily viewed in Atlantis. The example of an event viewed by Atlantis are in the section 4.2.2. Documentation is available on dedicated website [43].

3.4.2 Using Athena

Athena is a very robust framework. Apart from common data types, methods and functions, it provides central software repository for all algorithms (it means that every user can use the code of all other users, which made their code part of the Athena), and also a tool for managing all Athena software - the Configuration Management Tool (CMT).

All ATLAS offline software can be browsed via web, for example using ATLAS LXR server [44]. The code is divided into dozens of independent packages, each specialized in some particular task (for example digitization of the Pixel Detector). If a user finds a package that would be of use for him, it can be "checked out" using CMT. This means that the content of the package is copied to the user's local directory. As is usual in Unix, users get only the source codes which they had to compile to obtain binaries.

To run the Athena, one needs not only the compiled source code, but also so-called jobOption files. These are python scripts which are used to choose which algorithms will be executed and when they will be executed, to feed parameters into the algorithms and also to specify the input and output. Also due to the utilization of Python, the jobOptions can contain loops, conditions and other usual programming structures which can for example decide which algorithm to run given some particular type of input data.

For configuring the algorithm the jobOptions use a system of flags - each flag activates or disables some feature of the algorithm, or sets value of some variable. Using jobOptions allows us to run different algorithms and to steer their execution without having to recompile them. It also means, that the knowledge of the C++ is not the necessary condition to successfully run the Athena. The understanding of Python and the knowledge of the set of possible flags is enough for most users.

The Athena package is usually delivered with a set of jobOptions which can be used to perform typical tasks with the algorithm. So that by using copy and paste one can make a jobOption file suiting his needs without even knowing the Python.

The Athena is under continuous development, so to keep some order the software is divided into releases. The actual release (May 2008) has number 14. The release is basically set of software packages which were tested to be working together. The amount of testing is of course different in production releases which comes every 3-6 months and are denoted like 14.0.X., the development releases, coming every month (denoted 14.X.0) and the nightly releases, which are basically the newest code and are tested on the run.

Other consequence of the continuous development is that the documentation is still a step or more behind the actual status. The main sources of information about the Athena are ATLAS Twiki pages [45], static (or classic) ATLAS software pages [46], Doxygen documentation [47] and the hypernews [48].

ATLAS TWiki pages are based on the concept of wiki - that means that every user can write his experience with some problem and how to solve it. Or just describe the algorithm he had produced. Because everybody can contribute, Twiki pages are like blackboard in a discussion room where everybody can write notes. The advantage is that nowadays Twiki covers really a lot of topics, but the disadvantage is that you can never be sure that there are no mistakes. Also the topics are most often incomplete. Last year a campaign for validating Twiki pages was launched, so that if user comes across a page with a logo "validated", he can be quite sure, that the information is useful.

Static pages covers less topics than Twiki, but the content is made by Athena developers, so that is usually more accurate than Twiki.

Doxygen is automatically generated code documentation, however is mostly very technical, depending on how verbose was the developer in writing comments. User can quickly find there how is some method or data type defined, but this require some knowledge of C++.

Probably the most useful source of information and help is the hypernews forum - a collection of web based e-mail conferences on some topic (e.g. alignment, pixel offline software, etc.). There user can get help from the experts quite quickly.

3.4.3 ROOT

A paragraph about physics analysis briefly mentioned ROOT as one of the analysis tools. Similar to the Athena, ROOT is also C++ based software framework, although not so robust. Because ROOT is specialized in high-energy physics, it provides classes like Lorentz Vector or Histogram, etc. These can be used in constructing ROOT algorithms.

There are basically two ways of using ROOT. The first one is interactive mode - a user writes the C++ statements on the command line and they are executed by ROOT interpreter. The second way is to write a script, store it and then execute it. The script can be also compiled which speeds up the calculation approximately ten times.

ROOT is able to do many things, but the most used feature is plotting histograms - it is able to do many different types of histograms which users can simply edit via ROOT graphical user interface or from command line.

Apart from histograms the ROOT is able to do a lot of mathematical tasks like infinitesimal calculus or linear algebra. It can cooperate with OpenGL, so that it is also used for making fancy 3D models of the detectors and other devices. ROOT can also draw the Feynman diagrams.

ROOT uses its own filetype as the main output. Typical suffix is .root. This format is very economical in means of ratio between stored information and the actual file size. Therefore it is used also by the Athena as a typical output or input. The ROOT is very well integrated in the Athena - one can produce ROOT histograms directly from the Athena.

Although ROOT starts with a command line interface, it is possible to turn on graphical user interface - user just has to create an instance of the class TBrowser. This opens a browser, where one can open a root file for editing.

ROOT is very popular in HEP community and is used not only by ATLAS collaboration, but rather by most experimental particle physicists and even by people from other professions who need software for data analysis and visualization.

The documentation, examples and installation guides for ROOT can be found on its web site [49].

3.4.4 Monitoring

In this section I would like to introduce one particular piece of the Athena which has undergone extensive development recently: the monitoring package, more specifically Pixel monitoring. It is contained in the package `InnerDetector/InDetMonitoring/PixelMonitoring` and is a sister package to monitoring packages of other ID subsystems.

Because there is online and offline ATLAS software, there is also online and offline monitoring. As was mentioned in the beginning of the previous section, the online software consists mainly of data acquisition system and detector control system (DCS). So that the main task of online monitoring is to show the actual state of the detector (like temperature, humidity, pressure) to the shifter and if possible, store it for future reference. Most often this is done automatically by sending the graphs in some regular interval (e.g. every day) to a dedicated web page.

The task of offline monitoring is however different. It is run along the normal Athena software chain and, generally speaking, it produces histograms showing the 'data quality'. Naturally, the exact meaning of this term is highly dependent on the physics input. And that has been very variable in the past year as there has been various types of tests during the Pixel Detector commissioning. So that the pixel monitoring software had to be different for every detector setup. This resulted in state when monitoring code was a rather unorganized set of several pieces of code with very few in common.

That is why the pixel monitoring software was completely rebuild since the beginning of 2008. Nowadays, there is a common interface (jobOption file) in which user chooses which kind of setup he is using and the proper monitoring histograms are initialized and filled.

Recently a new type of monitoring setup was created which will be used during pixel sign-off in May. The whole code is contained in `commissioning.cxx`, whose content can be easily viewed by ViewCVS [50]. The structure of the code is quite simple. In the first part the requested histograms are booked in the memory, in the second there are methods how to fill them during each event and the last part is post-processing, i.e. the data in histograms are used to produce several new summary histograms.

During Pixel sign-off, the monitored quantities will be Pixel module occupancy and Time over Threshold (ToT). Occupancy of a pixel/module is the number of hits it received during one run. Example of such histogram is on Fig. 3.8 During post-processing, we also produce histograms with occupancy spectrum, i.e. the number of hits divided by the total number of events. This histograms can tell us whether there were any 'noisy' or 'dead' pixels during the run. Noisy pixels are fault electronics which produce more hits than they actually had. Dead pixels, on the other hand, are these which produce very little or no signal.

If we plot pixel occupancy spectrum (e.g. Fig. 3.9), we would see that most of pixels are normal, but several produce much more signal than average (noisy). We can also plot a noisy pixel map for a particular module, so that we can see which pixel is bad and should be excluded from data taking.

This shows that monitoring software will be particularly important during the first phases of ATLAS running because it will show how our detector behaves. Without this knowledge, proper tracking would be impossible, so that there would be no data to analyze.

3.4.5 Full Dress Rehearsal

Last year was done first of so-called Full Dress Rehearsals (FDR-1) to prepare for the real data. In this exercise a data containing practically everything that can emerge in *pp* collisions were produced (unlike the previous studies where they had always only a certain type of physics

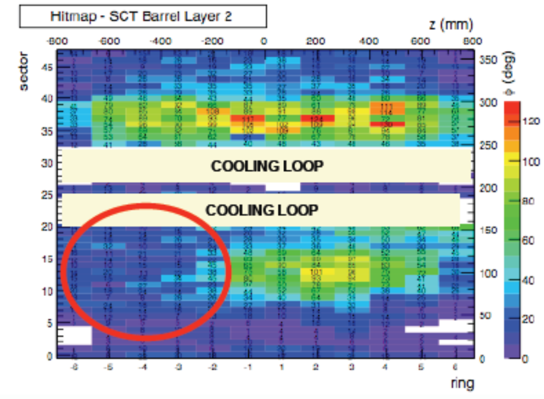

Figure 3.8: Occupancy of the SCT modules during February cosmic run. Notice that a lot of modules were off due to a failure in cooling. Similar picture for Pixel modules is not available yet, as the data taking will start on second week in May. Figure from [51].

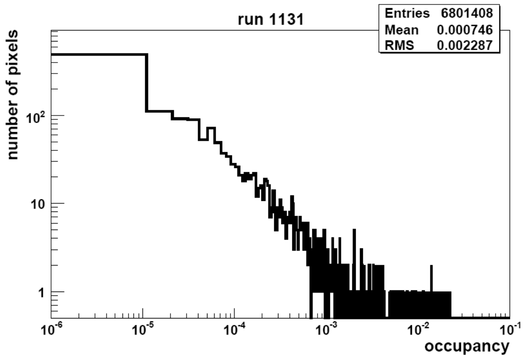

Figure 3.9: Pixel occupancy spectrum during the cosmic rays test on surface. Most of pixels have occupancy smaller than 10^{-5}, but the noisy pixels can have occupancy as high as 10^{-2}. Notice the logarithmic scale on both axes. Figure from [52].

simulated). Also this time no MC truth was included in the data, because there would be no such things in the real data.

Several detector problems (like malfunctioning modules) were included too, so that the physicists had to carefully distinguish whether the missing energy was caused by a SUSY particle or by the broken calorimeter.

Example of FDR-1 physical analysis is on Fig. 3.10. It shows the invariant mass of muon pair (after filtering on on both muons having larger momentum than 4 GeV) and we can see nice peaks at J/ψ and Υ masses, indicating that our reconstruction algorithms work properly.

FDR-1 was a very interesting exercise to test our computing system, although it provided less than one-day LHC data for initial luminosity. FDR-2 is planned for June and will provide more data with higher luminosity and so will serve as a final test before the real physics data taking.

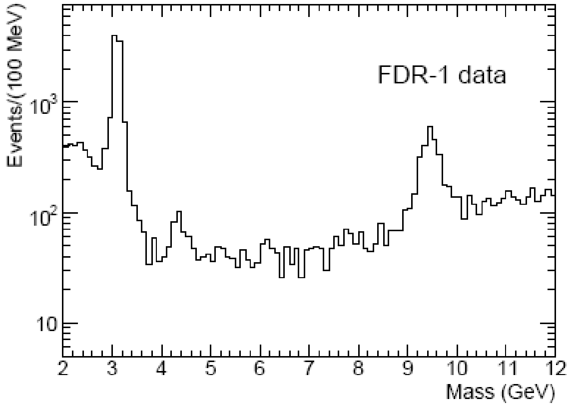

Figure 3.10: Reconstruction of muon pair mass during FDR-1. We can see nice peaks at region of J/ψ ($c\bar{c}$) and Υ ($b\bar{b}$). Plot corresponds to very early data and poor calibration. Figure from [53].

Chapter 4

Early Physics

4.1 Expectations

After more than fifteen years of designing, testing and building, both ATLAS and LHC are nearly finished. The LHC is being cooled down and in July a first beam should be injected to the LHC. After some period with single beam operation, another beam will be injected and the collisions may start. There is no exact schedule as there are too many unknowns, but in general we suppose that the first ”physics runs” would be in August 2008.

ATLAS should be completed by June. The last piece to be connected is the Pixel Detector, which will be signed-off in May and as soon as the ATLAS is complete it can begin to collect data. There are several types of physical phenomena that can be investigated before the physics runs, together they are called ”early physics”.

4.1.1 Cosmic Rays on the Surface

The first possible measurement will be the muons coming from the cosmic rays. This term is somewhat misnomer, because there are no rays or continuous beams of incoming particles, but rather a lot of individual particles coming to Earth from all directions. Some of them are originating in the Sun, but most are coming from the sources outside the Solar system and sometimes even outside our Galaxy.

The cosmic rays are composed mostly (over 90 %) from protons, the rest are helium nuclei (9 %) and electrons. The energy spectrum of incoming cosmic particles is very wide, ranging from few MeV to more than 10^{20} eV, seven orders of magnitude higher energy than the protons at LHC will have. When the energetic particle enters the Earth atmosphere, it collides with the molecules of air. The particles created in collisions are mostly pions and neutrons and they further decay to photons, neutrinos, electrons and muons. These particles can then be detected on surface and in fact, this was the way how the muon and pion were discovered in 1930s and 1940s, respectively.

If muons are energetic enough, they can pass through ground, therefore they are present even in the experimental cavern 100 meters below surface so that they can be measured at ATLAS as soon as the detector will be turned on. They have been of a big interest lately because the distribution of cosmic rays is well known and therefore they can be used to test the detector. Also, cosmic rays have the ability to cross the whole detector which is something the particles produced in collisions in the center of ATLAS will never have as they typically travel only through one hemisphere of the detector.

Calorimeters were tested by cosmic rays as soon as they were installed in the cavern, i.e. some two years ago. TRT and SCT were tested in pit several times in 2007 and 2008 in so called Mx weeks (“milestone”). But Pixel Detector has not been connected in pit until the middle of

May, so that it could not have been tested by cosmics before that.

Nevertheless, in the end of 2006 the endcap part of the Pixel Detector was tested by cosmic rays on surface. The three disks were placed horizontally (i.e. facing the ceiling, to maximize the number of cosmic muons coming through the detector) and four scintillators were placed above and under them to serve as a trigger (see Fig. 4.1). The event was recorded if the top scintillator and at least one of the bottom scintillators was hit. This ensured that most of the recorded muons indeed passed through the detector. There was also an iron shielding above the bottom scintillators which stopped low-energy muons.

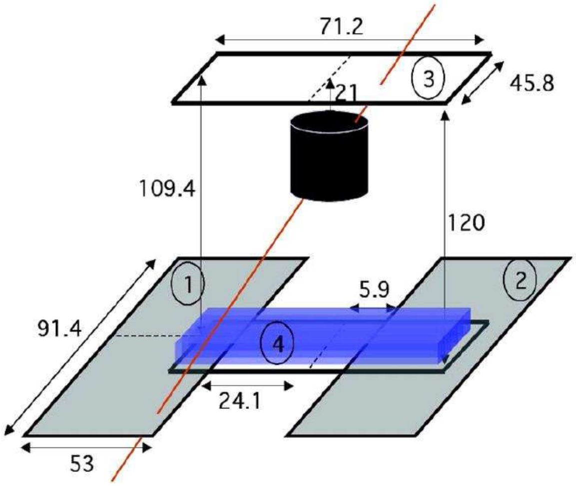

Figure 4.1: Setup of the measurement of the cosmic muons in Pixel endcap on the surface. There are four scintillator plates as well as iron shielding (in blue). Red line symbolizes accepted cosmic track. Figure from [52].

The first thing that was studied using the cosmic data was the electronic noise. When the muon fired the trigger the data were recorded for sixteen consecutive BCID's (bunch crossing ID) and every hit contained an information in which BCID it was collected. One BCID lasts 25 ns, i.e. the time between two bunch crossings at full luminosity. The signal caused by the cosmic muons had BCID=5. When the BCID of the hit was smaller than 4 or larger than 6, it was classified as a noisy hit.

The noisy pixels were investigated by counting the occupancy: number of noisy hits per event and BCID. The pixel was classified as "hot" if its occupancy was greater than 10^{-5} - it was about 0.023 % of all pixels. The noise occupancy of the good pixels was about 10^{-10}. The distribution of the BCID for both the good and hot pixels is on Fig. 4.2. We can observe that most good hits indeed have BCID=5, while there is no correlation between the trigger signal and the noise (as should be the case).

After that the map of noisy pixels was compared with the map of pixels marked as special during the production. Fig. 4.3 shows good agreement between the both.

In case of semiconductor detectors, important measured quantity is also time over threshold (ToT), which tells how long has been a particular pixel excited to the conduction band by a traversing muon. The distribution of ToT for all hits is on Fig. 4.4. The time is in units of a 25 ns (i.e. one bunch crossing) and we can see that it peaks at 5 BCID (125 ns), explaining why the good hits had BCID=5.

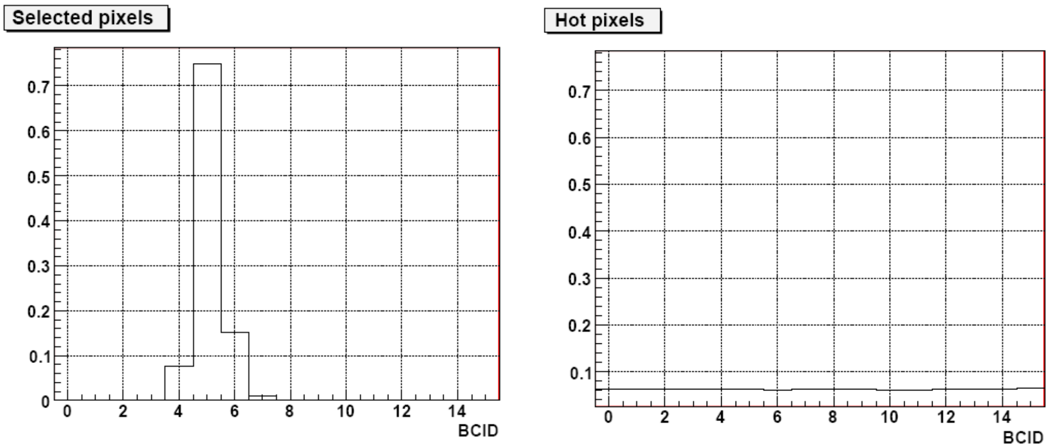

(a) “Good” pixels

(b) “Noisy” pixels

Figure 4.2: Distribution of the BCID for both good and noisy pixels. We can see strong dependence on BCID (and through it on trigger), while the hot pixels give signal in a rather random fashion. Figures from [52].

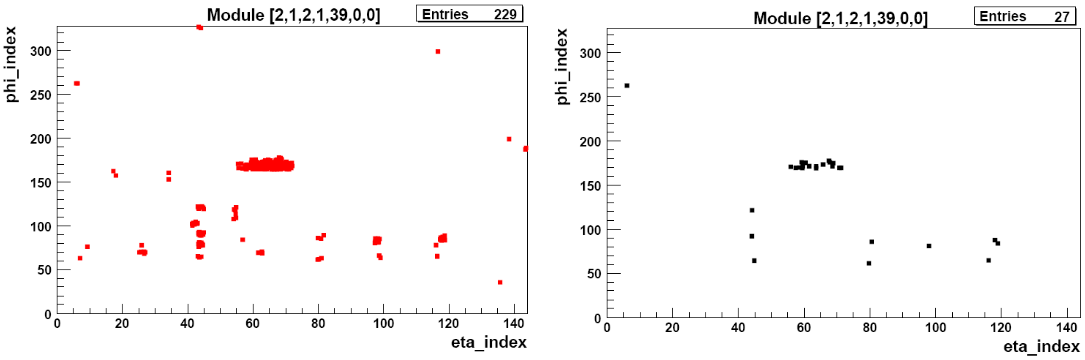

(a) “Special” pixels

(b) “Noisy” pixels

Figure 4.3: Distribution of pixels marked as “special” during production tests for one particular module and the distribution of noisy pixels for the same module. Figures from [52].

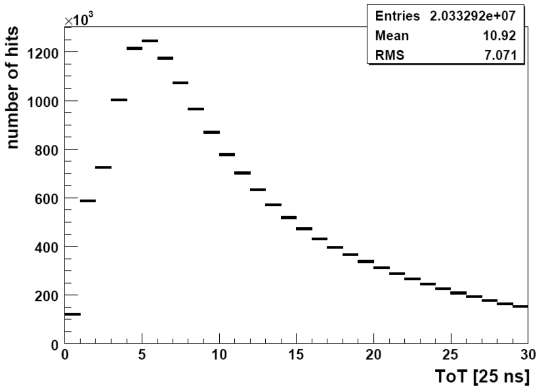

Figure 4.4: Distribution of the Time over threshold of the pixel hits in the units of 25 ns. The peak is visible at 125 ns (=5 BCID). Figure from [52].

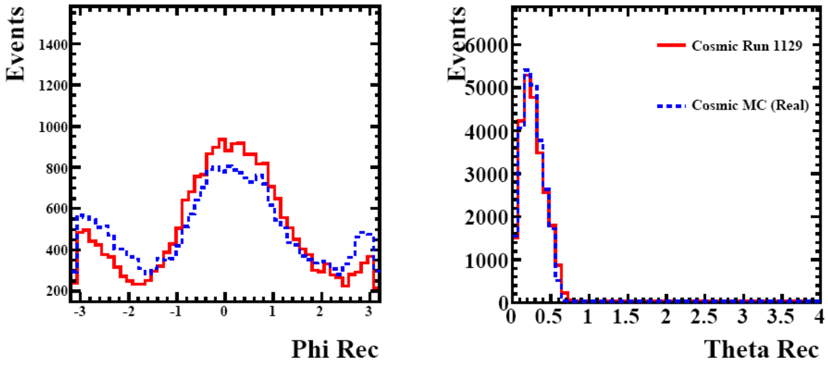

Figure 4.5: Comparison of the Monte Carlo simulation (blue dashed line) and real data (red solid line) for the tracks of cosmic muons. Left plot shows azimuthal angle ϕ of the tracks, while the right shows polar angle θ. Figure from [52].

After masking the hot pixels the data were used to reconstruct the cosmic tracks and compared them to the simulation. During the reconstruction, no ESD or AOD was produced, but all information about tracks was saved in CBNT (combined ntuple). The agreement was excellent (see Fig. 4.5).

Because of the large statistics collected during cosmic runs, data could also have been used for the alignment study. The modules on pixel disks are purposely constructed to have an overlap between the modules on the top and bottom side of the disks. This feature was used to study relative alignment of the neighbouring modules. The Figure 4.6 shows the distribution of the tracks with overlap hits. There was quite a lot such tracks (24 %) because the overlap of modules on pixel disks is rather high.

The relative alignment constants were determined from the overlap hits residuals, i.e. the difference between the position of the hit and the extrapolated track. In case the overlap hit was used in track fitting, the residuals are called biased, in the other case the residuals are unbiased. After that a dedicated alignment algorithm (so called robust alignment) was used. It uses iterative approach and is based on two assumptions: (1) for the perfectly aligned detector the residuals are centered around zero and (2) if the module is shifted by δ, the mean of unbiased residual distribution is shifted by $-\delta$. The results from the alignment are on Fig. 4.7. It found that the shifts of modules are in order of several dozens μm. This confirmed the expectations from the optical survey of the module positions.

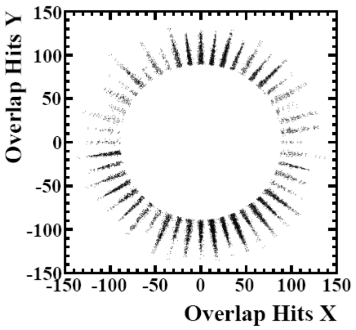

Figure 4.6: The distribution of the overlap hits in the pixel endcaps. Figure from [52].

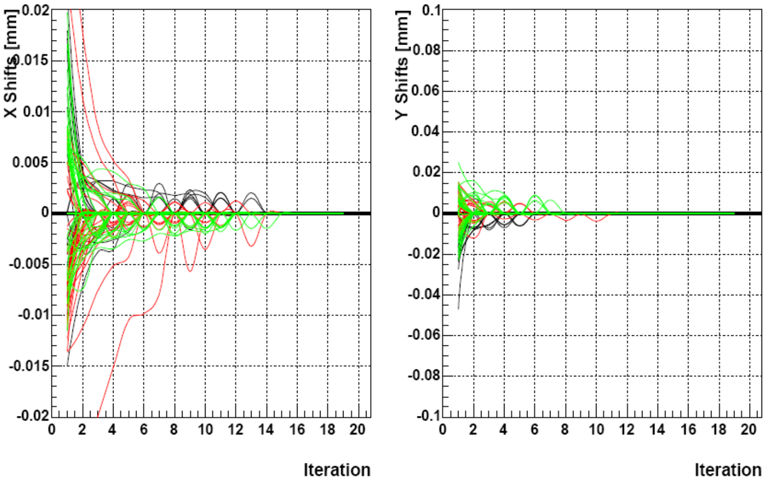

Figure 4.7: The effect of robust alignment on unbiased residuals in x (right) and y (left) direction. Figure from [52].

To sum up, the surface measurement of cosmic muons has been a great success. It was able not only to test the pixel noise level and find the hot pixels, but thanks to the pixel disks geometry and the amount of collected data, the cosmics also helped with the alignment of the modules. Equally importantly, data showed nice agreement with the simulation, thus giving confidence in the current software model of the Pixel Detector and also to the detector itself. More about the Pixel endcap cosmic tests can be found in the dedicated ATLAS note [52].

4.1.2 Early Physics in the pit

In a few weeks the ATLAS should be completed and it will begin to collect data. The first ones will be cosmic muons which can be collected even before the LHC will be functional. Unlike the surface study described in the previous section, in this case the cosmic muons will investigate mainly barrel area, because the modules there are facing the surface, while the disk modules are nearly parallel to the direction of most incoming cosmic muons. The rate and distribution of cosmic muons will be discussed in next sections.

As soon as the beam will be circulating in the LHC there will be hits by the particles from the beam halo. These are machine induced secondary particles which originate in the scattering of the beam protons on the residual gas in the vacuum pipe or at beam-beam scattering in the insertion regions. The beam halo particles are coming in the direction of the beam leaving signal mainly in the endcap disks, so that they can provide complementary data to the cosmic muons.

Beam halo is composed mainly of charged hadrons, but there are are also neutrons (7 %) and muons (6 %). The flux of the beam halo through the plane corresponding to the cavern wall at nominal luminosity should be of order of several MHz. These events could be very useful for the endcap alignment, however, no beam halo tracks are recovered with the standard tracking tools yet [56].

In the single beam period we can observe also so called beam-gas events. These are collisions of beam particles with the remaining gas inside ATLAS Inner Detector. Figure 4.8 shows schema of both beam-halo and beam-gas events.

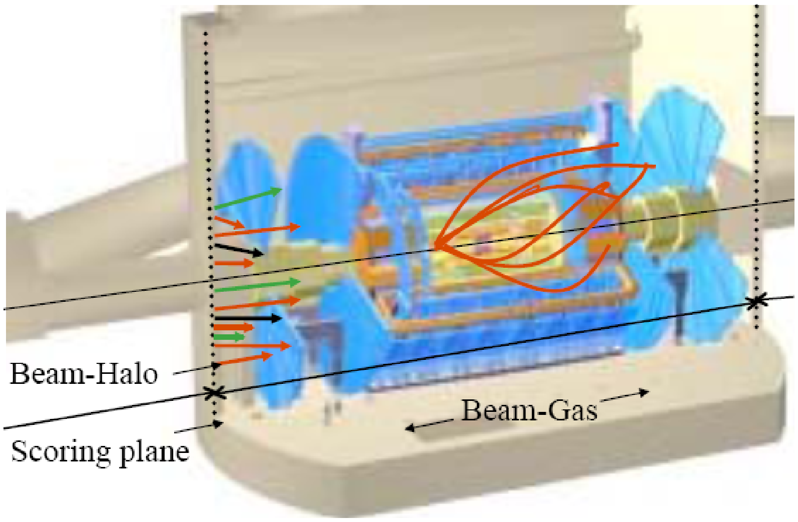

Figure 4.8: Schematic view of beam halo and beam gas events. Figure from [56].

The rate of such events can be estimated from the luminosity and the supposed level of vacuum. It varies from 0.1 Hz for 43 bunches in the startup to 156 Hz for running with 2808 bunches (nominal value) after the machine conditioning. These events can be successfully reconstructed and will be useful for alignment, especially in time we would have only one beam and therefore no *pp* collisions.

The comprehensive (yet in some parts out-of-date) study of early physics at ATLAS can be found in [54].

4.2 Simulation of Cosmic Muons in the Experimental Cavern

Because the testing of Pixel endcap with cosmic muons on surface was very successful, there was natural question whether we would be able to do the same in the experimental cavern with the Pixel barrel. We know very well the distribution of the cosmic muons on the surface [6], so that to figure out the distribution in the cavern we carried out a Monte Carlo simulation in the Athena.

Two different Monte Carlo models were tested. One based on the approximation formula from Particle Data Group [6] and one based on experimental fits written for experiment ALEPH by Alois Putzer. Their main difference is that the PDG formula slightly overestimate the rate of low energetic muons.

Both of these generators were used to create a muon sample with the respective distribution, and these muons were used as an input for Geant3 simulation which took in account the ATLAS and cavern geometry as well as the 100 m overburden. The cosmic muon rate in the cavern was afterwards compared with the measurements which were done in 2004 [54]. This proved that the generator by A. Putzer is in much better agreement with the real data than the PDG formula, so that the Putzer's generator become part of the standard Athena code and the main generator of cosmic muons for ATLAS.

Our study had, therefore, two parts. The first was Monte Carlo generation of the large muon sample and subsequent simulation in the newest simulation code (Geant4) and latest ATLAS geometry. Afterwards, the simulated data were turned into digits and reconstructed with the standard reconstruction tools to find the efficiency of our tracking tool and prepare for the real data taking.

4.2.1 Monte Carlo Generator and Geant4 Simulation of Hits

As it was anticipated in the previous section, the standard tool for generating cosmic muons at ATLAS is slightly modified algorithm of Alois Putzer. The original FORTRAN code was wrapped in C++ and it can be found in the package `Generators/CosmicGenerator`. The code consists of two major parts: CosmicGenerator, which is the main algorithm that collects input parameters, handles output files and calls the second algorithm - CosmicGun, which is the wrapper for the A. Putzer's code and its purpose is to create muons according to hard-coded distribution of energy and impact angles. The version which we used for generating cosmic muons is tagged `CosmicGenerator-00-00-24`, which is not the latest, but has all the functionality needed and is stable. Athena release 13.0.10 was used for the simulation.

In practice, the "generation of cosmic muon" means that a point-like particle with muon characteristics is created in a given spacepoint (chosen randomly from all allowed, see below) and is given a momentum vector according to the prior probability distribution. The user can define following options for the cosmic muon generator:

- Range of energies.
- The highest possible deviation of the incoming muon direction from being vertical (in terms of maximal value of the cosine of polar angle).
- Coordinates of the area/volume in which the muons will be generated.
- Whether to switch on optimization for the cavern (see later).
- The size and center of optimizing sphere: It serves as the primary filter. Only these muons whose momentum points towards this sphere are passed to the Geant4 for further simulation.

As was announced beforehand, all this options are simply set via python script (jobOptions file). Because it is not entirely clear how should be this parameters set, the first part of study was dedicated to testing different parameter settings to find the optimal one i.e. as realistic as possible while taking as low computing time as possible.

In case of energies it is quite straightforward: The larger range, the more realistic. Fortunately, thanks to the character of cosmic rays, there are very few high energetic particles, so that large increase in the upper bound leads only to a minimal increase of computing time. A bit more difficult is the setting of lower range, as there is a lot of low-energetic muons. On the other hand, most of them would not be able to pass through the overburden. So we chose 1 GeV as the lower bound and 2 TeV as upper bound. Note that default setting for lowest energy was 10 times higher. Figure 4.9 shows energy distribution of those muons which were able to hit the Pixel Detector and it can be seen, that discarding muons with initial energy lower than 10 GeV would seriously harm the realism of the simulation.

The cut on size of polar angle can speed up the whole calculation by ignoring muons which have so large polar angle that they will never hit the ATLAS cavern. Nevertheless this cut was set to 0 (i.e. all muons accepted) because the optimizing sphere is much better filter on direction than this one.

It is obvious that there is no sense in generating muons in some volume over the ATLAS cavern and that a plane is completely sufficient. To find how big this plane should be to capture most of the muons eventually hitting the Pixel Detector while staying as small as possible, we generated a cosmic muon sample originating in the area of 600 m × 600 m over the ATLAS cavern (this was the largest area allowed by ATLAS geometry).

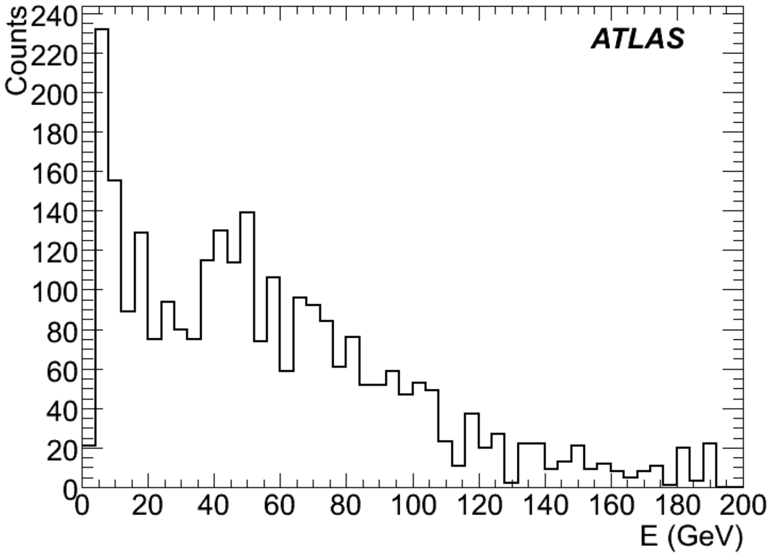

Figure 4.9: Distribution of the initial energies of the cosmic muons that eventually hit the Pixel Detector.

Figure 4.10 shows that over 99 % of muons hitting the Pixel Detector are coming from the region 400 m × 400 m. This means that if we choose 400 m × 400 m as a generating surface we would save about half of the computing time (the area was halved) while losing less than 1 % of cosmic muons. Note also that the generating plane is not on surface but rather ca. 20 m above it to include also surface structures in the simulation.

The last (and probably most difficult) choice were the properties of the optimizing sphere. While its position should be undoubtedly in the center of ATLAS, its size is a matter of discussion, because there are several effects acting against each other. Suppose we make the sphere very small - so that most of the generated muons will be ignored and it would take some time to generate a decent sample. On the other hand, such muons almost certainly hit the Pixel Detector, so that the simulation would be quicker. Too small optimizing sphere can also bring penalty on realism, as there may be muons which do not originally point to the sphere, but are scattered and in the end they hit the detector (cf. Fig. 4.11). On the contrary, large optimizing sphere would allow fast generation, but then most of the muons fed to the simulation would not hit the Pixel Detector so that we would be losing time generating muons not hitting anything as can be also seen on Fig. 4.11.

Experience shows that the simulation part takes much longer than MC generator, so that to minimize the computing time we should make optimizing sphere small. But not too small to lose muons which were not originally pointing to it (Fig. 4.11). As a hint we investigated scattering properties of the muons which hit the Pixel Detector. Plots showing the correlation between angles on surface and at the time of the hit are shown on Fig. 4.12. We can see that angles on surface and at the times of the hit are virtually the same, meaning that these cosmic muons which are able to hit the Pixel Detector do not scatter much, so that we can safely choose quite small radius. In particular we chose $r = 10$ m which safely covers whole tracker and calorimeters, while still rules out over 99.9 % of generated muons. A simple test also showed that further decreasing of the size of this sphere increases the generating time exponentially, so that for smaller spheres there would be very little gain in calculation time.

The simulation of the cosmic muons in the ground and inside of the cavern was done by

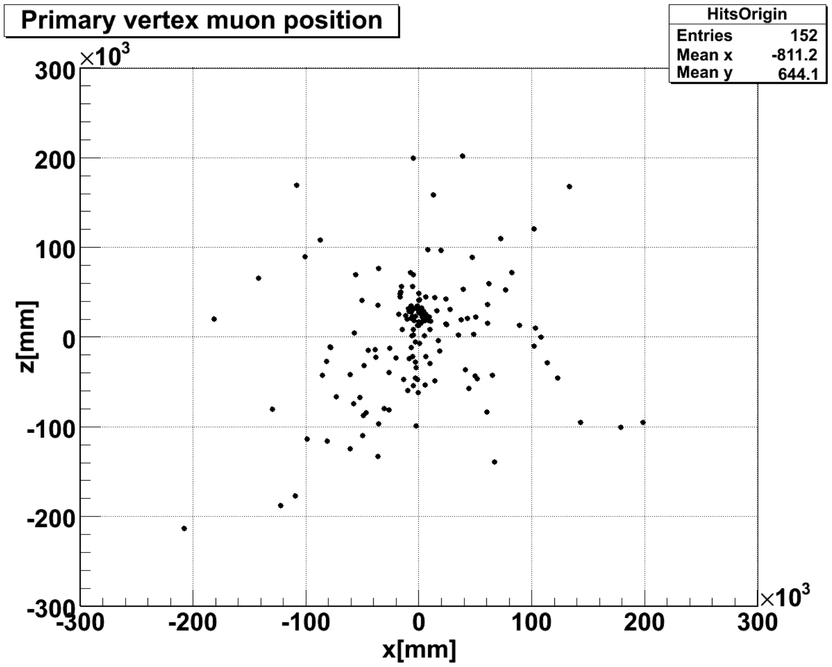

Figure 4.10: Distribution of the initial positions of the cosmic muons that eventually hit the Pixel Detector.

Geant4. It is a stand-alone toolkit for the simulation of the passage of particles through matter. It is widely used in a lot of areas (including medicine and space flights) and it is used also in ATLAS. There, however, it was incorporated into the Athena framework, so that even if the user do not know Geant4, he can still use it via standardized Athena tools. The documentation can be found in [59].

The package which is used as in interface for Geant4 in Athena is called `Simulation/G4Atlas/G4AtlasApps`. For our study we used version `G4AtlasApps-00-02-15`. This package does not contain any simulation code, but it rather hosts a bunch of Python scripts which can be used for various simulation scenarios on ATLAS. One of the jobOption files is dedicated also to the simulation of cosmic rays on ATLAS. There, like in the case of the Monte Carlo generator, can be set various simulation options:

- Which part of ATLAS should be included in the simulation. There are simple switches for the whole systems like Inner Detector, Calorimeters or Muon spectrometer, but there are also finer switches for the particular subdetectors.
- Number of processed events.
- Whether a root file with hits should be produced and the name of this output file.
- Version of ATLAS geometry.
- Whether to write track timing information. It stores the positions of cosmic muons when entering the cavern, so that they can be used again in case we would like to test the effect of different ATLAS geometry and we would not want to simulate again the flight of muons through the ground.
- The way how Geant4 obtains initial positions of the particles. There are three possibilities: load some files with generated muons, call some Monte Carlo generator included in the

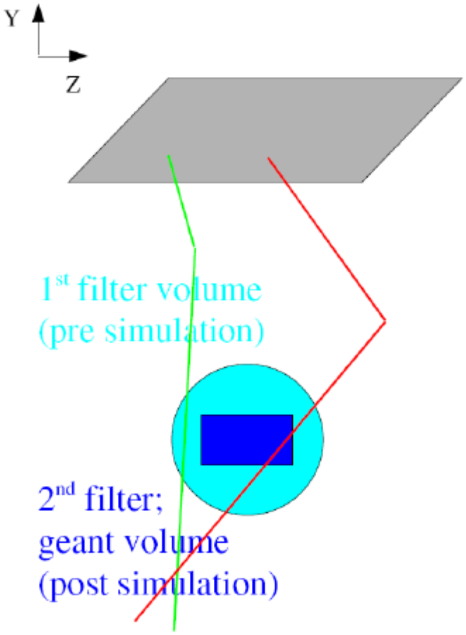

Figure 4.11: Scheme showing the function and caveats of optimizing sphere. The green event is accepted by Geant4, although it eventually miss the detector, while the red event is rejected in the start.

Athena, or use its own toy Monte Carlo. In case of the last choice, user can set the type of generated particle, its angular and momentum distribution as well the initial area where the particle is created.

- Various user actions: a declaration of user algorithms which can be used to run user-defined simulation.

Because the whole detector is now complete we want to turn on all the parts of ATLAS, because traversing muons will lost energy on every subdetector they will fly through and if they are not properly simulated, the results will be unrealistic.

The number of processed events is a matter of personal taste and is determined mainly by the computing resources. In this case, runs with 30 000 simulated cosmic muons were optimal. The results from the simulation were always stored in the root file with hits because we wanted to use them for further processing.

The versions of ATLAS geometry used for the cosmic studies are different from these used in the standard simulation in a way that the first contains also the overburden, access shafts and surface structures. The schematic view of the ATLAS experimental cavern is on Fig. 4.13. The convention is that the name of geometry containing also the overburden is beginning with *ATLAS-Comm*. If there is no magnetic field, the geometry name begins with *ATLAS-CommNF*. After that follow three couples of digits which indicate the version. Full information about the various geometry tags can be found in [60]. In our study we were using ATLAS-CommNF-02-00-00, which is compatible with ATLAS geometry tag CSC-01-02-00 that was widely used during the commissioning studies last year.

The writing of track timing information may seem unnecessary if we do not want to change the geometry. Nevertheless, the timing information is necessary for further digitization and reconstruction so that we had this option turned on. The main source of particles for this study

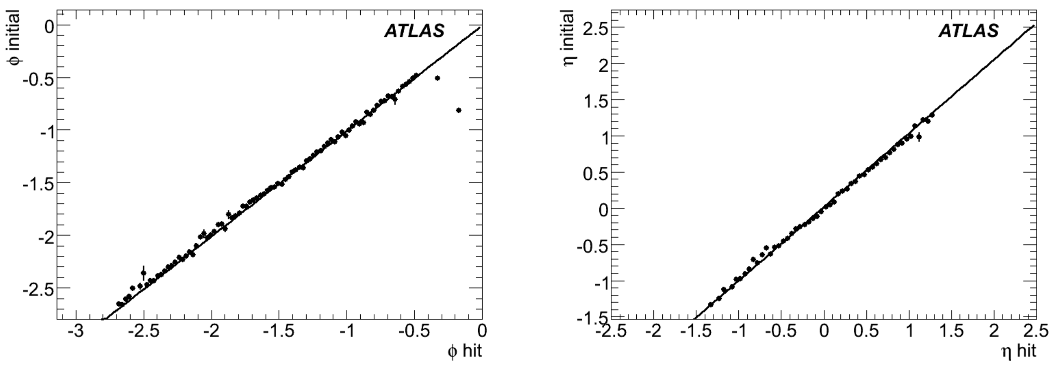

(a) ϕ correlation

(b) η correlation

Figure 4.12: Correlation of the initial angle and the angle at the time of the hit, together with the linear fit. The equation of the fit is $y = 1.002x - 0.007$ for ϕ and $y = 1.017x + 0.017$ for η.

Muons generated	Muons accepted	in Pixels	in ID	Real time	Pixels rate	ID rate
6 907 433 412	11 575 728	220	59 333	259.6 s	0.85 Hz	229 Hz

Table 4.1: Rate of the cosmic muons determined from the simulation by Geant4 for the Inner Detector and for the Pixel Detector alone. The parameters of the simulation are described in the text.

was of course the MC generator described earlier in this section. Nonetheless, for debugging we also used simple built-in generator which was firing muons from the point on the surface directly above the interaction point straight down with the energy 50 GeV.

We also added some user modifications to our simulation. The first modification was the usage of filter on Inner Detector volume: only these particles which enter inside it are saved, all others are discarded and so saving both storage space and also reconstruction time. This filter is purely geometrical, based on dimensions of the TRT.

The other modification is that all hits in Pixel Detector are saved not only to root file but also to a text file, together with the flight direction, lost and remaining energy and of course the identification of the module which was hit.

The last modification we added was the saving of hits on cavern floor, together with their energy and flight direction. This helped us to understand what is the overall distribution of the cosmic muons in the ATLAS cavern and compare the results with the measurements of the cosmic muons rate in 2004 [54].

All this changes were done via infrastructure provided by the package `Simulation/G4Utilities/G4UserActions`. Here the user can define what will be done (on top of normal simulation) at the beginning and end of run, start and end of each event and at every step of the simulation. Because this methods will be run by Geant4, user has access to all Geant4 classes, variables and libraries.

The first result from the simulation was the cosmic muon rate. It is summarized in the Table 4.1. We can see that over 99 % of generated muons were discarded due to primary filtering by the optimizing sphere. Also we can see that only a tiny fraction of this muons (0.5 %) is able to reach the Inner Detector, and from these only 0.3 % can hit the Pixel Detector.

This might seem a bit too low, but if we look on the rates, it is more optimistic due to huge initial cosmic muon rate on surface. Even in Pixel Detector we can collect several thousands

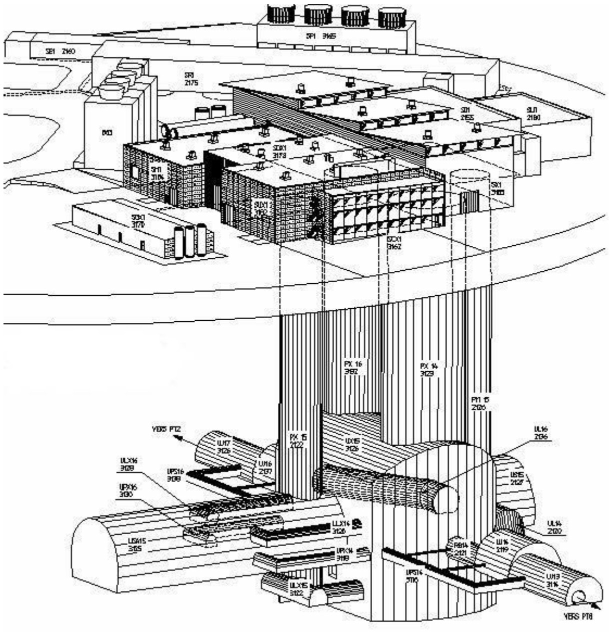

Figure 4.13: The view of the ATLAS cavern, support caverns, access shafts and surface structures at Point 1.

hits in a few hours of data taking which ensures hits in all parts of the detector. Nevertheless, the barrel geometry is quite different than the geometry of pixel disks, especially, the overlap in barrel is much smaller, so that we may suppose that the statistics for doing an alignment of pixel barrel will have to be much larger than we had on surface.

There are several other facts about the cosmic rays we can deduct directly from the simulation, thanks to our modification to the simulation algorithm which produces text file with information of interest. Therefore we developed a ROOT script which reads the simulation text output and fills the data in the histograms.

Figure 4.14 shows distribution of the position and of the energy of the generated muons. We can clearly see the impact of access shafts: most hits are concentrated just over the shafts. The distribution of energy shows that there are in fact two types of muons: one low-energy coming through the shafts, whose energy peaks at about 10 GeV. The others are the high-energy muons coming mostly through the ground and with energy peaking at about 50 GeV.

Other thing that we can observe from the simulation data is the distribution of pseudorapidity and of the azimuthal angle ϕ in the time of hit. It is on Fig. 4.15. The ϕ distribution is normal, similar to one obtainable on the surface. However, the distribution in pseudorapidity is largely affected by the existence of the shafts (cf. diagram on Fig. 4.16).

Next, we can observe the distribution of the hits in the Pixel Detector. Figure 4.17 shows the cosmic muon hits in the Pixel Detector as a function of the distance from the beam axis r and the z coordinate. We can clearly see the three layers and three disks. The total number of hits was 2820 (corresponding to about 55 minutes of data taking) while in the outermost layer, there were 1171 hits (in 676 modules), in the middle 859 (in 494 modules) and in the inner layer, there were 510 hits (in 286 modules). At disks, the situation is much more worse. There were only 144 hits in the A endcap (positive z direction) and 134 hits in the C endcap (negative z direction), while there is 144 modules at each endcap.

The Fig. 4.17 shows, that the hits distribution is rather homogenous, the observed inhomogeneity is coming mainly from the low statistics, but there may be also some effect coming from

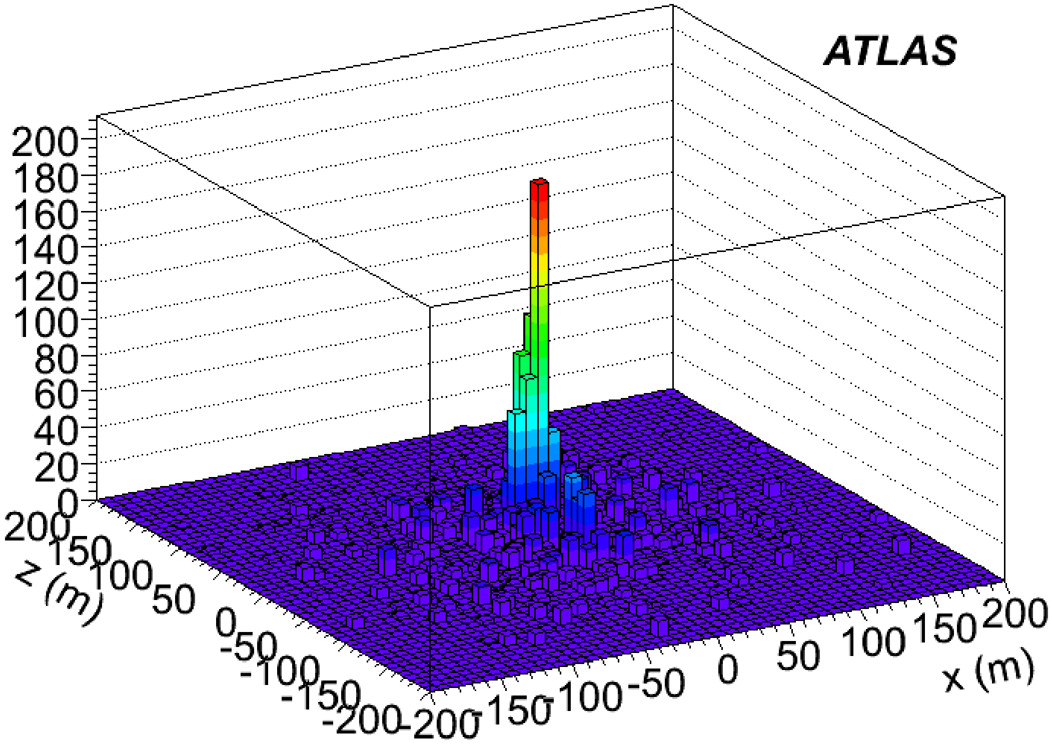

Figure 4.14: The density of the initial positions of accepted cosmic muons. We can see that most muons eventually hitting the Pixel Detector are coming through the main shaft. Notice also smaller peak next to it corresponding to the secondary access shaft.

cavern geometry (shafts), although it should be very small since the Pixel Detector is not lying under any access shaft.

The energy of incoming particles on Fig. 4.18 is quite different from the initial energy distribution (4.9). Now there are no two peaks but rather exponential decrease of energy of all particles.

Figure 4.19 shows the distribution of deposited energy (left plot) and also integrated deposited energy in the whole Pixel Detector (right plot). We observe, that the distribution can be nicely fitted by the Landau function. The integrated energy distribution is very homogenous, showing that the cosmic rays will leave practically same energy in all modules.

As was mentioned above, our modified simulation algorithm monitored also the hits on the floor. The results can be seen on Figure 4.20. We can clearly see the dominating effect of the access shaft in the hits distribution on the left figure. Unsurprisingly, through the shafts are coming mostly low energetic muons, as can be checked on the right plot of Fig. 4.20, which shows average energy per hit. This results are in very good agreement with the measurements, which were done in 2004 in the empty cavern (Fig. 4.21).

Altogether we can see, that our simulation is giving realistic results which are in agreement with experiment, where comparable. The main result is the rate in Pixel Detector which is about 0.85 Hz. This number is in excellent agreement with the results from other groups, thus giving confidence to our simulation. This rate ensures decent cosmic coverage for the barrel area, but it would be much worse in the endcap area.

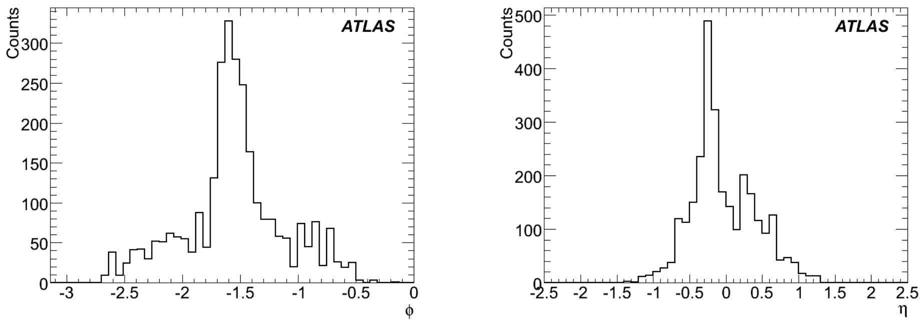

(a) ϕ distribution

(b) η distribution

Figure 4.15: The distribution of the ϕ and η of cosmic muons. While most muons come in vertical direction $\phi = -\pi/2$, in pseudorapidity we can see overwhelming effect of both access shafts.

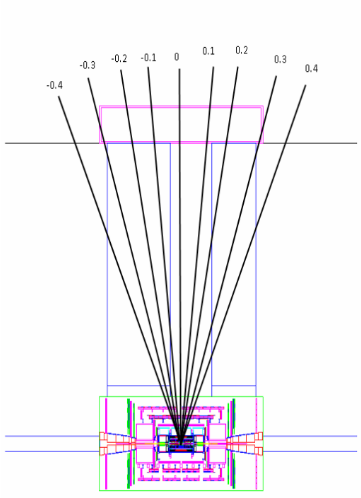

Figure 4.16: Values of pseudorapidity in ATLAS cavern and access shafts.

The cosmic muons can be divided in two categories: low energetic (ca. 10 GeV on surface) ones, coming perpendicular through the shafts and high energetic ones (ca. 50 GeV on surface), coming with high pseudorapidity through the ground. This fact could be used in improving the efficiency of the Monte Carlo simulation by splitting it in two parts, thus improving the speed.

All this is quite promising so that we continued in this study by digitizing the hits and reconstructing them to find more realistic and detailed results about the effects of cosmic rays on the Inner Detector.

4.2.2 Digitization of Hits and the Cosmic Muon Reconstruction

The digitization of cosmic hits is quite straightforward and since release 13 could be done "out-of-the-box". This means, that standard ATLAS digitization algorithms can digitize cosmic hits. In the jobOption files one can set standard things like input and output files, number of processed events, number of skipped events in the beginning (this is very important when running several digitization jobs in parallel - each of them has to skip different number of events so that all jobs digitize different data) and the geometry tag.

The main difference in digitizing cosmics and collision data is in different timing - cosmic muons are coming from above so that they are not synchronized in any way with the LHC 25

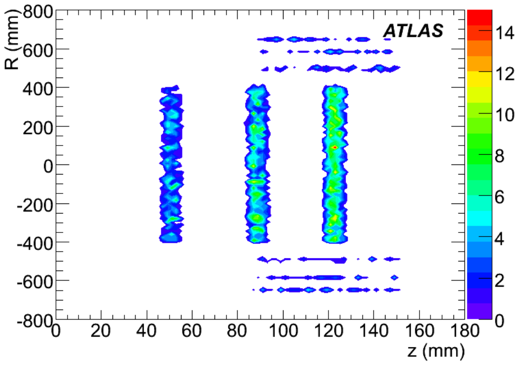

Figure 4.17: The density of hits in the r-z plane. All 3 layers and 6 disks are visible.

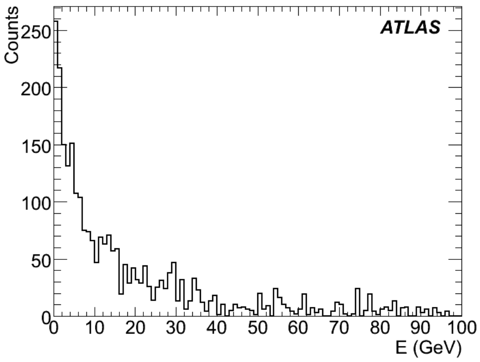

Figure 4.18: Energy of the muons hitting the Pixel Detector.

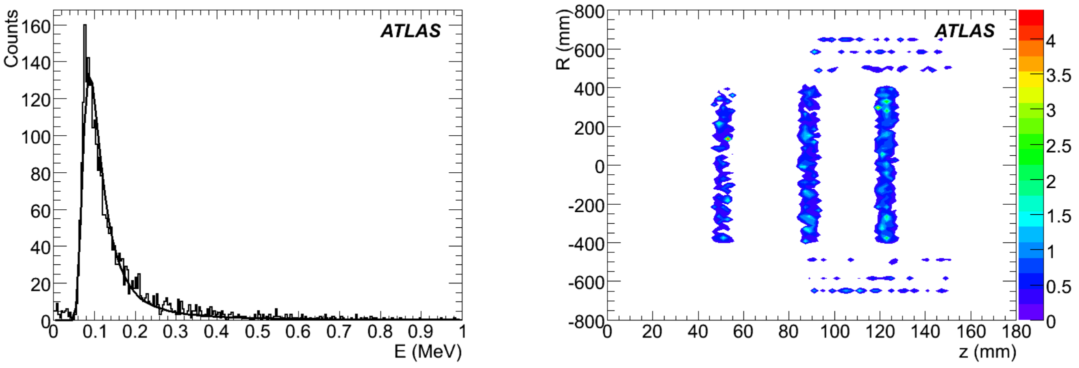

(a)

(b)

Figure 4.19: (a) The distribution of the energy deposited in the Pixel Detector fitted with Landau function. (b) The distribution of deposited energy per hit (in MeV) in r-z plane.

ns clock. But this issue has been already addressed, so that the user only has to uncomment relevant lines.

Other options one may set in the digitization jobOptions are, which detectors will be on and switching on and off noise in calorimeters. In our case we left only Inner Detector turned on because we would like to know how this particular part of ATLAS responds to the cosmic rays. Also, this can help keeping the output files reasonably small and last but not least, this concentration just on ID significantly reduces computing time. The output of digitization are RDO files, as was already stated in the third chapter. This files are then used as an input for the reconstruction.

There are several software packages which care for the ATLAS reconstruction. Their quality is crucial for the experiment, so that these packages are constantly tested by the whole collaboration and all changes in the reconstruction software must be authorized by the physics convenors. The main reconstruction package is called `Reconstruction/RecExample/RecExCommon`. It is able to reconstruct ATLAS *pp* event using the information from all detectors. Nevertheless, this package is maybe too robust for some purposes, so that there is also package `InnerDetector/InDetExample/InDetRecExample` which contains reconstruction only for the Inner Detector. In fact, the first package calls the latter during its run to do ID reconstruction.

Nevertheless, reconstruction of cosmic muons is different from the reconstruction of *pp* colli-

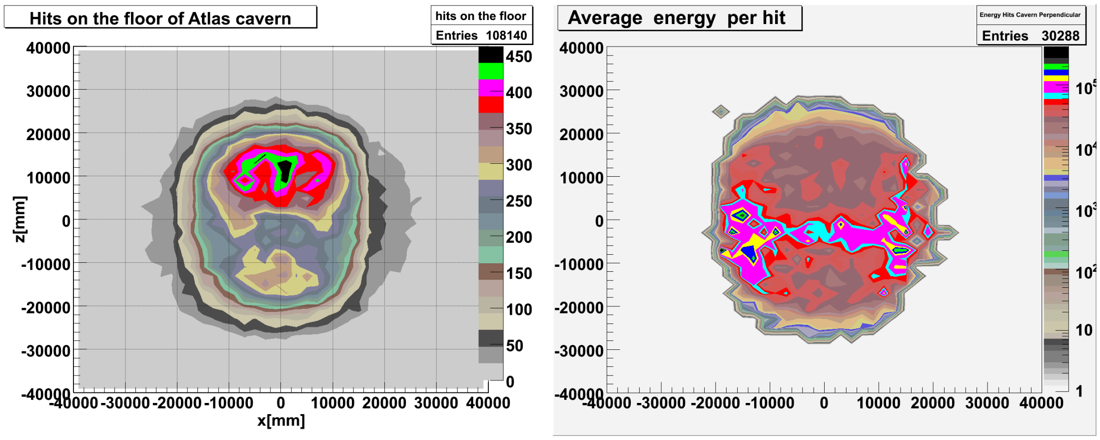

(a) Hits density (b) Energy per hit

Figure 4.20: The density of the hits on the floor of the cavern we got from our simulation together with the energy (in GeV) per hit on the floor distribution.

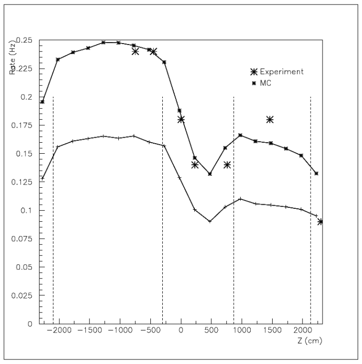

Figure 4.21: The results from the old simulation of cosmic muons in the cavern (line) together with the measurements of the flux (stars). Figure from [54].

sions. The main differences are that the tracks do not start in the centre of detector but on its top, leading to different timing (see Fig. 4.22). Also, in case of ID, they leave tracks mostly in TRT and very rarely in Pixels or SCT. The example of such a track is on Figure 4.23. There are also other issues, like that cosmic muons are able to hit several adjacent modules in one layer (see Fig. 4.24). This all means that our approach to cosmic reconstruction has to be different from the normal reconstruction.

Two approaches were tried, one which basically modified the standard ID reconstruction algorithm to suit the cosmic setup, while the second involved development of completely new cosmics dedicated tracking. They differ in many details, but they share the same common idea: the tracking begins in silicon detectors (SCT and Pixels) and the track is then extended to the TRT. Example of such a reconstructed track is on Fig. 4.25. Nevertheless, in case of energetic muon, the algorithm is able to reconstruct tracks which have no hits in SCT/Pixel.

The main package for cosmic reconstruction in Inner Detector is called `InnerDetector/InDetExample/InDetCosmicRecExample`. In the last year it experienced very intensive development and now, in the Release 14 it is able to handle all kinds of cosmic setup and is able to reconstruct online real data coming directly from the detector, stored experimental data as well as simulated data. The latest versions also contains the current set of alignment constants obtained during the cosmic runs in February and March 2008.

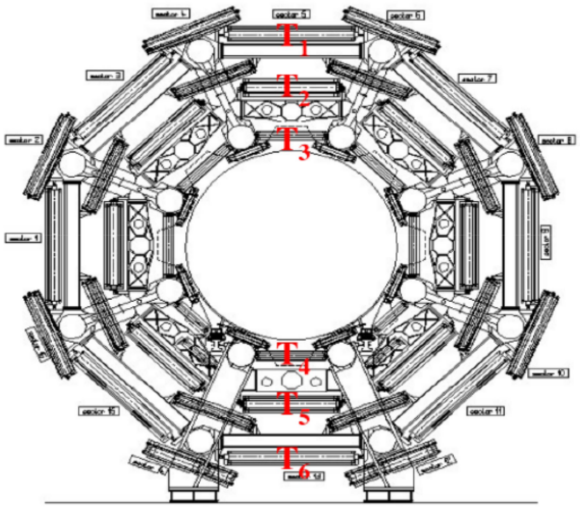

Figure 4.22: Timing for cosmics and normal events (from collisions). Normal events have $T_1 > T_2 > T_3$ and $T_4 < T_5 < T_6$. For cosmics, however, we have $T_1 < T_2 < T_3 < T_4 < T_5 < T_6$. Figure from [57].

The cosmic reconstruction package is quite robust with a lot of possible settings so that it is designed to be as user-friendly as possible, because it is run by many people, not only by its programmers. There are several interconnected jobOption files that take care of that. The main jobOption file which user submits to Athena is called `InDetCosmicRec_topOptions.py`. It does nothing more than calling other python scripts which do the actual job. All parameters of the job are set in a script `InDetCosmicFlags_jobOptions`.

Basically, user can set this categories of parameters:

- Input files. This include switch between simulated and real data and giving their locations.
- Type of cosmic setup. This is very important in case of real data. In each of the data taking weeks, the setup was slightly different, so that this setting helps to do correct reconstruction.
- Geometry tag. It is the same as in the previous cases. In case of simulated files as an input, the geometry tags used in simulation and reconstruction must match, otherwise the results have no physical sense.
- Set of alignment constants. These are stored in a large common database of alignment constants (several TB), each set is tagged, so that user only chooses the appropriate tag to obtain desired set of constants.
- Switching on and off Pixel, SCT and TRT in reconstruction.
- Optimization switches like masking of dead channels.
- Switching on and off different reconstruction algorithms.
- Several options regarding track fitting (e.g. which fitter to use).
- Monitoring switches. There is global switch, but one can also turn on monitoring only for some subsystem, like Pixels.

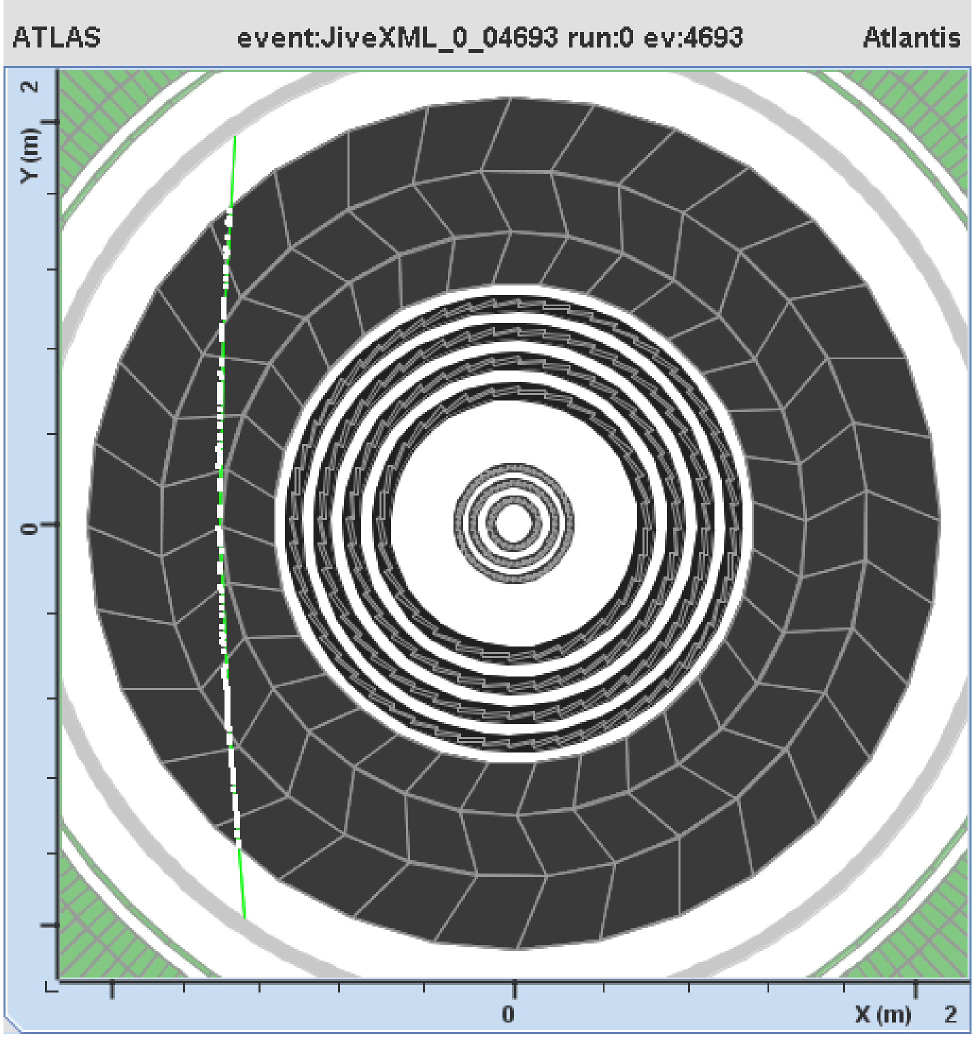

Figure 4.23: Reconstructed cosmic track which has no hits in silicon detectors. White squares are TRT drift circles, green line is reconstructed track.

- Switch for making CBNT. This is an ntuble containing all relevant tracking information in a form of ROOT tree. It serves for an analysis of the properties of cosmic tracks.
- Switch for making ESD. It is turned off by default, as all relevant information goes into CBNT and there is no need of further Athena analysis run on the ESDs.
- Switch for making JiveXML files to display the events via Atlantis.

The details of particular settings (like name and location of CBNT or JiveXML files) are set in their private jobOptions, also available in the package.

In this study we used one of the newest versions of the package, tagged `InDetCosmicRecExample-00-03-62`, which not only implements the latest set of alignment constants but is also able to reconstruct the real data from the current cosmic setup.

Apart from changing the values of flags we also did some minor changes to the python code in the jobOptions to make the package suit out needs. Because the default version is not able to load more then one file with digitized cosmic hits at a time, we had to add several lines to the jobOptions to add this feature to the package. We also turned on production of JiveXML files which we used for a visualization of events in Atlantis (Figs. 4.23 to 4.25).

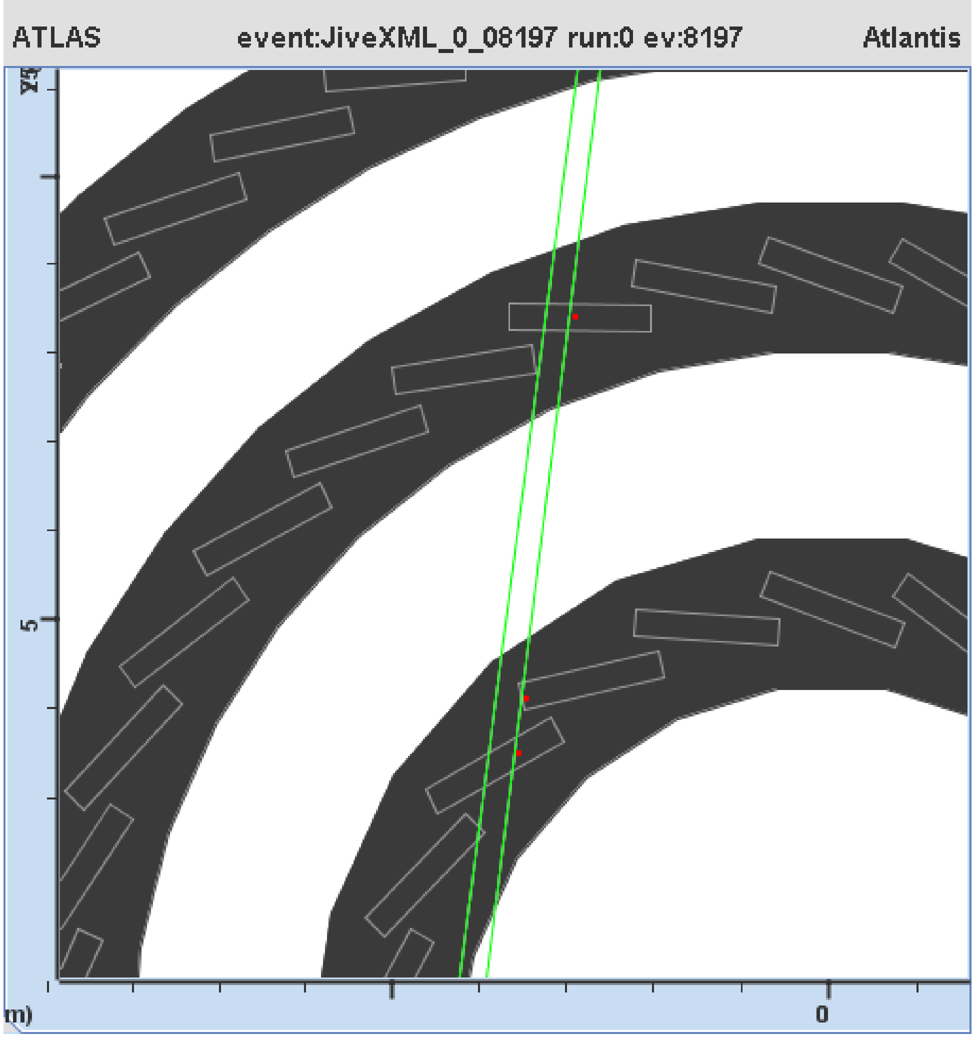

Figure 4.24: Reconstructed cosmic track that passes through several pixel modules in one layer. Notice also two tracks provided by two algorithms.

Only about 3000 out of more than 50 000 events in Inner Detector were visualized, but this was enough to prove that our expectations based on the Geant4 simulation were true: the Atlantis clearly showed that Pixel hits are very rare, but when they happen, there are usually more than two hits in the Pixel Detector and quite often they are even in the same layer (see detail of such a cosmic track at Fig. 4.24). But sometimes quite strange things can happen, which the standard tracking cannot handle - for example splitting of track due to cosmic muon decay (Fig. 4.26). And sometimes the tracking is simply wrong (Fig. 4.27).

The information about cosmic tracks are stored in the Combined Ntuple (CBNT). It can be accessed and processed via ROOT. The data from reconstruction are stored in a form of a TTree, which is a structure that organize output event-wise and track-wise but ROOT allows also access directly to sums over all events and tracks. In case of reconstruction of the simulated events, the CBNT stores also information from the original Monte Carlo, so that it is possible to study the reconstruction efficiency.

The Figure 4.28 shows the number of reconstructed tracks in the semiconductor detectors. We can see that out of more than 50000 events in Inner Detector only about 1000 tracks were reconstructed in the SCT/Pixel. The Figure 4.29 compares MC truth and the reconstructed

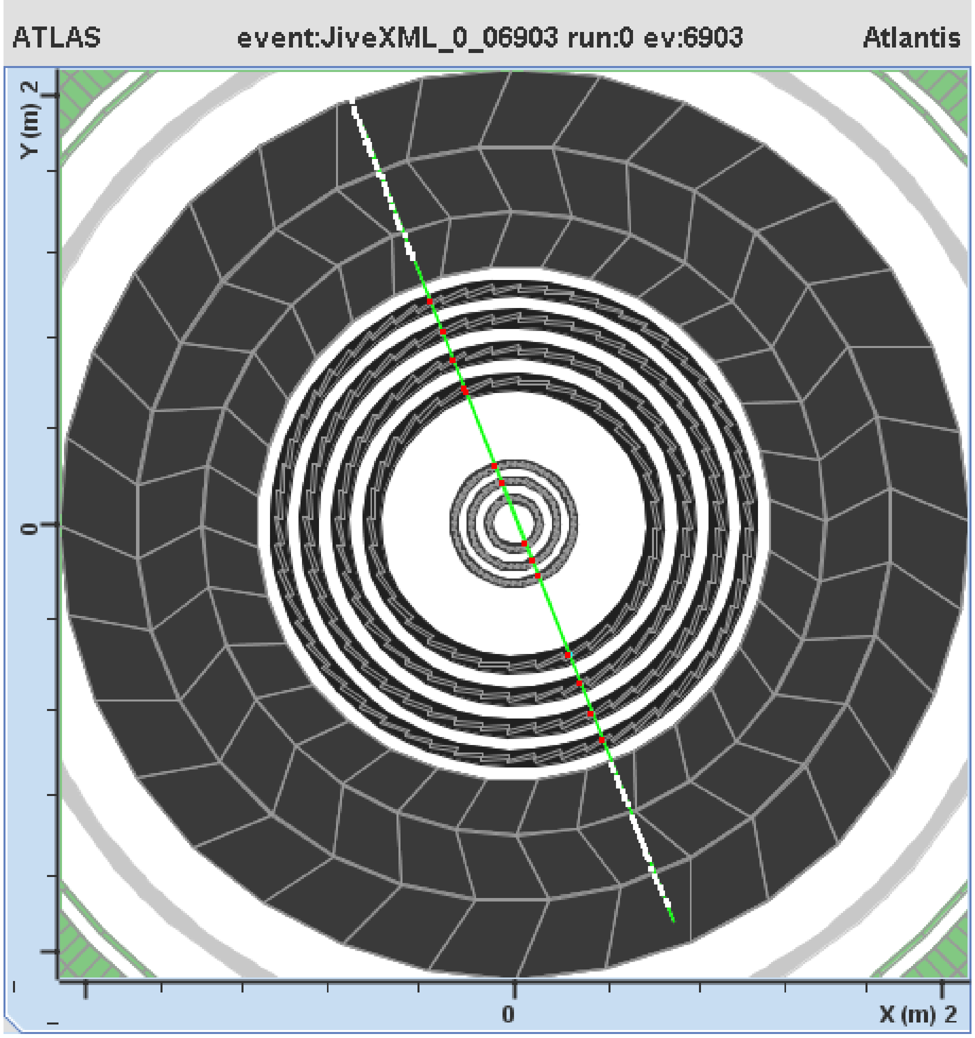

Figure 4.25: Very rare track coming through all layers of silicon and leaving hit in each one except one.

values for the azimuthal angle ϕ and polar angle θ. We observe excellent agreement in the shape of distributions.

As was stated above, due to comparably low rate, the main purpose of measuring the cosmics in Pixel Detector in the pit (at least at this stage of construction) will be just the testing of the functionality of the pixel modules. Therefore we were also interested in the results from Pixel monitoring.

The histogram showing the occupancy (number of hits during run) of all the modules in the second barrel layer is on Fig. 4.30. This should be compared with the similar histogram for modules in SCT barrel obtained during the February cosmic measurements (Fig. 3.8). We can see that they are similar, and that during data taking unexpected things like malfunctioning cooling loop can happen.

The Pixel monitoring is also able to handle occupancy of single pixels. The Fig. 4.31 shows the superposition of pixels' occupancy over all modules. In real data taking there will be important also the histograms with pixel occupancy spectrum like on Fig. 3.9 which is coming from the surface pixel tests. We did not produce any such histograms in our simulation because we had not simulated pixel noise (it was measured only for endcaps).

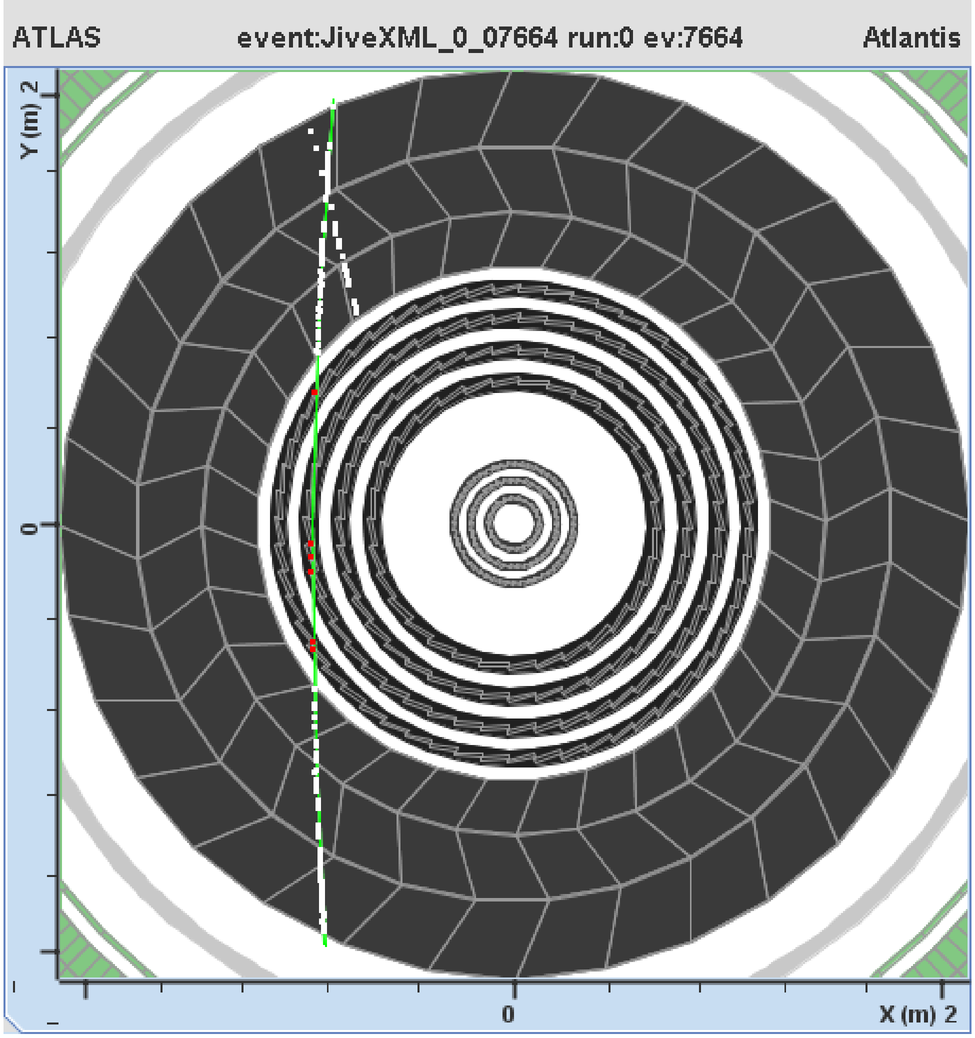

Figure 4.26: A track which split into two, but only one branch was reconstructed.

4.3 Conclusions

The events we should see in the beginning of ATLAS run will be different from these we will encounter during normal LHC run. In particular, there will be some events in a single beam period (beam gas, beam halo) and some events even without any beam (cosmic muons). Especially the last type of events is quite well known so that it can be used to calibrate the detector.

Cosmic muons were used to test the Pixel Detector on the surface and this study was a big success. Measurements were able to find both dead and noisy pixels and exclude them from data taking. Moreover, the collected statistics was so huge that it could have been used for the alignment of pixel modules (due to large overlap in disks).

Our aim was therefore to find whether something like that will be possible in pit after connecting Pixel Detector to ATLAS. So that we run a Geant4 simulation of cosmic rays (adapted to our needs), and proceed through the whole Athena chain. From the simulation results we were able to calculate the rate of cosmic muons both in Inner Detector and Pixel alone. We also got some particle distributions which showed that by far most muons have come through the shafts. However, the rate indicated that we would not be able to gather enough statistics for alignment of Pixel Detector in the fashion of surface test.

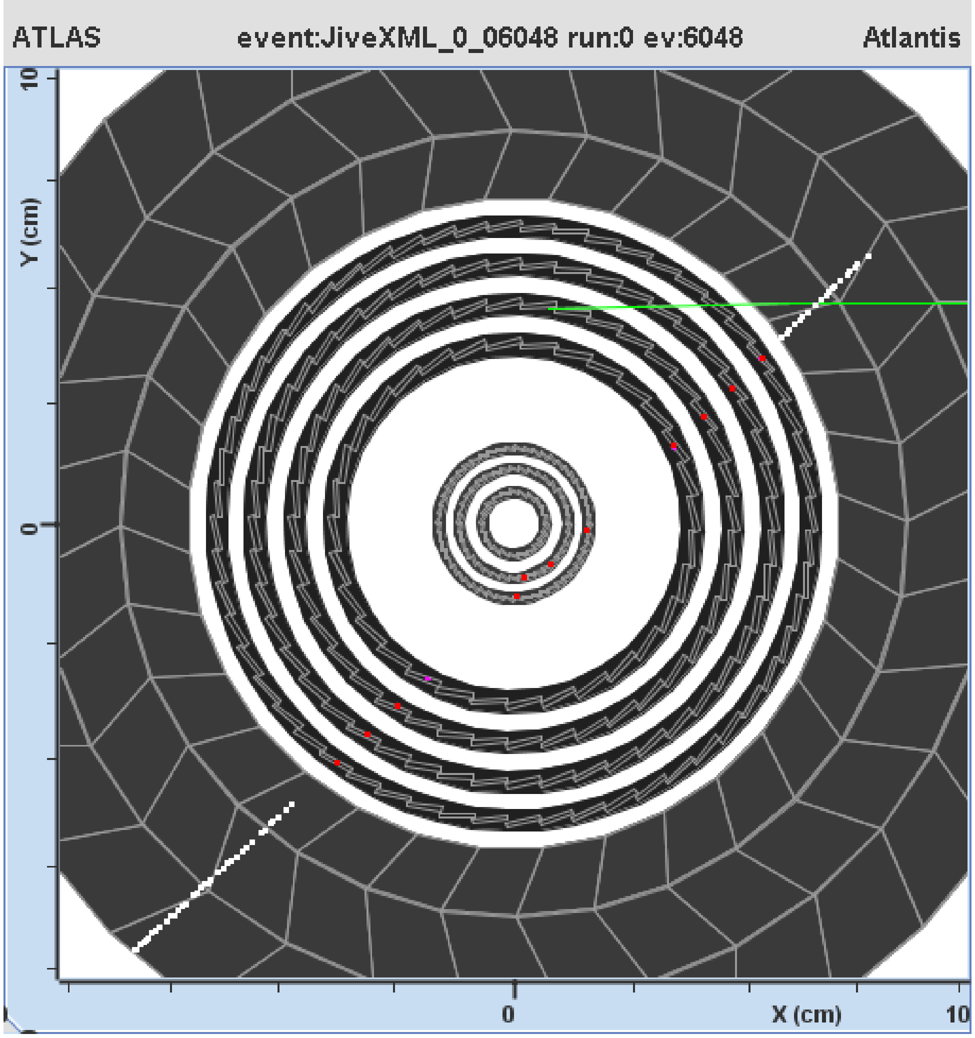

Figure 4.27: Although the trajectory of muon is clearly visible (white and red points), Athena was not able to reconstruct it (green line). Notice also two separated hits in one pixel layer.

To obtain more specific information, we digitized and reconstructed the simulated data. This allowed us also to test the quality of tracking algorithm. The reconstruction showed that the reconstruction software is able to handle cosmic muons without any big changes.

The visualization confirmed our prediction about cosmic muons behaviour. First, only a small portion of tracks in the Inner Detector leave some hit in the SCT or Pixel. In case it does, it is quite often several hits in one layer, because the track direction is often tangent to the detector modules.

The study of tracking ntuple showed, that the reconstruction has good quality - the angle distribution are practically identical with the Monte Carlo. The monitoring showed, that pixel modules and pixels were hit by cosmic muon in almost homogenous fashion, so that we would need much larger statistics to test the behaviour of detectors.

Altogether this study was an important lesson in using Athena, the main ATLAS software tool. Because ATLAS was not designed to be cosmic muon detector, the code had to be tweaked a little to suit our needs. We successfully proved that Athena software chain works and gives meaningful results for cosmic muons.

The results from reconstruction indicates that testing by cosmic muons is possible (the

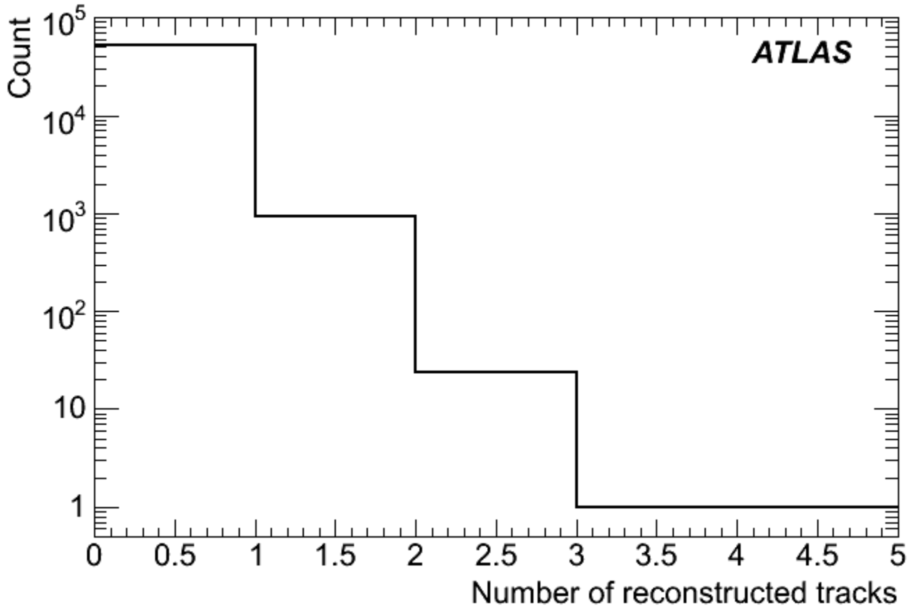

Figure 4.28: The distribution of the number of reconstructed tracks per event.

reconstruction is working) and for TRT and SCT it could be (and in fact is) very helpful. In Pixels, however, the rate is too small so that it is not clear if there will be time to collect enough statistics before the beam is injected into ATLAS. Nevertheless, it is still possible to collect cosmics in between the beam fills and in this way do an "online" calibration.

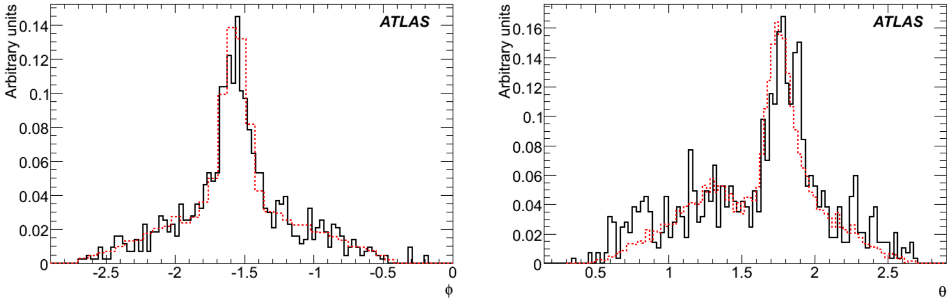

(a) (b)

Figure 4.29: The comparison of the reconstruction (black solid line) with the Monte Carlo data (red dashed line) for (a) ϕ and (b) θ.

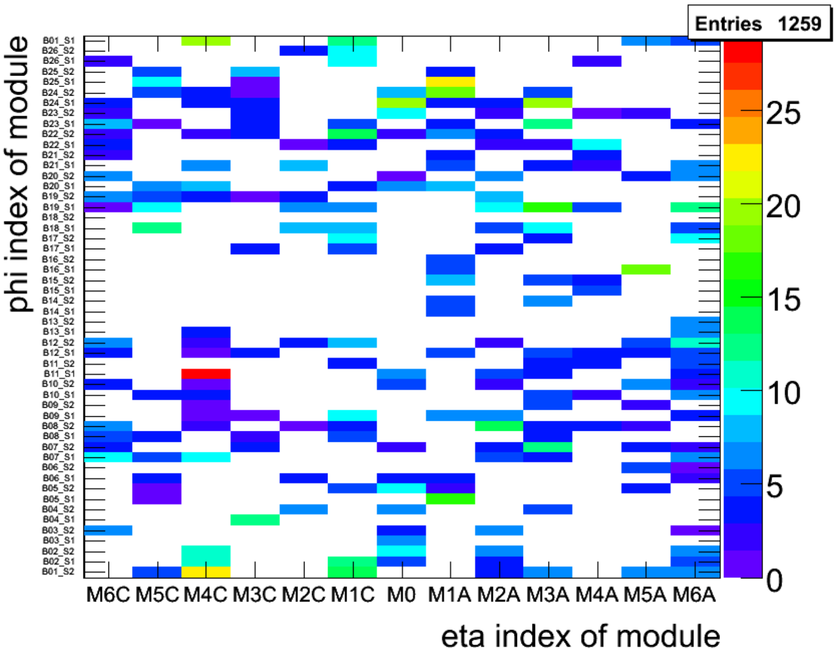

Figure 4.30: The occupancy of the modules in the outermost Pixel layer after ca. 30 minutes of data taking. Every rectangle is one module.

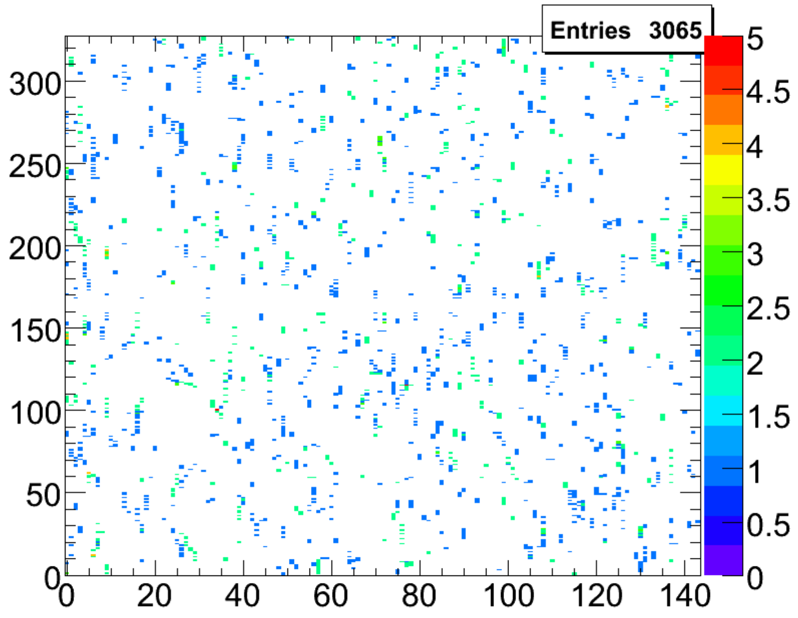

Figure 4.31: The occupancy of the single pixels integrated over all modules after ca. 30 minutes of data taking. Mostly there is about one or two hits per pixel, but in the left there is also cluster of pixels with about 4 hits.

Chapter 5

Thesis Summary

Standard Model (SM) is now, after forty years of existence, a well established theory. It passed all experimental tests and some of its predictions were proven to an extraordinary degree of precision by the experiments in 1990s and 2000s. The success of the Standard Model is in extremely economical packaging of basic principles which gives rise to nearly all observable particle phenomenology.

However, Standard Model has also some weak spots, both from theoretical and experimental point of view. First, the assignment of elementary particles to the five different representations of the underlying gauge group and their hypercharge values may seem somewhat haphazard. This could be solved by introducing new simple gauge group which can encompass the SM gauge group. These efforts are called Grand Unification Theories (GUT). The simplest of them however fails to pass experimental tests on proton lifetime - its predictions are too low. Also the exact calculation of the coupling strengths at unification scale (10^{15} GeV) shows that there is no unification of interactions, contrary to what the name suggests.

Remedy is brought with the anticipation of the Supersymmetry (SUSY). With this, GUT's predictions on proton lifetime are no longer in conflict with the experiment. Equally important, the unification scale is ten times higher and the unification of the interaction strengths indeed happens there. Also, assuming Supersymmetry, we can deal with quadratic divergences in SM scalar boson (Higgs) self-energy.

Exact Supersymmetry is excluded experimentally, nevertheless, calculations suggest that all above mentioned effects take place even if the SUSY is broken, assuming the mass difference between supersymmetric partners is not larger than several hundreds GeV. This leads to the high expectations for LHC, because its particle mass reach covers exactly the area where supersymmetric partners of ordinary particles should exist, if SUSY is to cure GUT and divergences in Higgs boson self-energy.

Probably the largest theoretical problem of the Standard Model is the correct description of the neutrino sector. Contrary to SM predictions, experiments found that neutrinos have masses and oscillate among several mass eigenstates. Nevertheless, SM cannot give mass to neutrinos in the same way as it does for other particles, because only left-handed neutrinos have been observed. This led to a prediction of another elementary particle, superheavy right-handed neutrino which should give mass to its left-handed counterpart via so-called seesaw mechanism (the heavier right-handed neutrino, the lighter left-handed one).

On the other hand, one key prediction of the Standard Model has not been proved yet: the existence of the spontaneous symmetry breaking (SSB). The first step should be the discovery of the scalar boson which is responsible for the SSB (Higgs boson). There are numerous way of observing and identifying Higgs at LHC, depending on its mass. But if Standard Model predictions are correct, the LHC would be a true Higgs factory.

The second step in proving SM right is much more difficult. The Higgs properties must be carefully measured to prove that the new particle is indeed a scalar boson (this require precise measurements of Higgs angular distributions) and that there is Higgs cubic and quartic coupling. Monte Carlo suggests that LHC should be able to exclude the possibility that there is no Higgs cubic coupling and that together with ILC it will be even able to measure the cubic coupling value. Unfortunately, this cannot be done for the quartic coupling and the few studies which have been done on this topic agreed that with present knowledge and technology we would never be able to even exclude the possibility that Higgs quartic coupling does not exist.

Also, it may happen that LHC discovers SUSY. In this case we should observe several Higgs bosons. The theory suggests that we should discover at least one of them, regardless of their mass. But if we are lucky enough we can discover all five Higgs bosons which are predicted by minimal SUSY.

From all the reasons above and several others (like expectations from cosmology and heavy ion physics), the LHC is eagerly awaited by whole particle physics community. The commissioning has finally started about a month ago and the first beam is anticipated in June 2008. Almost the same schedule is valid for the largest of LHC experiments: ATLAS. It should be completed by the end of May, so now all detector groups are busy with commissioning of ATLAS.

Integral part of the ATLAS experiment is the computing which can be divided into two parts. One is online computing which reads, filters and stores events from the detector as well as monitor the physical state of the experimental environment. The second part is offline computing which reconstructs events from the detector data and then analyzes them to find any traces of the new physics. To promote collaboration, (nearly) all ATLAS offline software is included in a common framework called Athena.

The equivalent of detector commissioning for Athena is called Full Dress Rehearsal (FDR). Instead of single physics channels, the complete output of proton-proton collisions at 14 TeV is simulated and this data are sent in real time to the reconstruction facility to test whether it is able to cope with the realistic data flow. The FDR data are also good exercise for analysis, because they contain a lot of various signals and backgrounds. Purposely, they contain no Monte Carlo information, so that the analysis is realistic in sense that physics teams do not know in advance what is included in data.

The effects we can observe in our detector as soon as it is commissioned are called "early physics". This includes cosmic rays, beam gas events (collisions of the beam protons with the remnants of gas in the beampipe) and beam halo - particles going in direction of beam outside the beam pipe.

From these especially the cosmic rays can be very useful in calibration of the detector, because we know very well what to expect, so that we can tweak settings of the detector to obtain desired cosmic muon distribution.

The Pixel Detector was tested for the first time by cosmic muons on surface in the end of 2006 and this exercise was a big success. It helped to discover malfunctioning pixels (either noisy or dead), but thanks to the very large statistics it also helped to align the pixel modules, which were shifted from their nominal positions by several dozens μm.

This study was however done only for endcap disks, so that the collaboration was interested whether it was possible to repeat it for pixel barrel which had been already lowered to the experimental cavern. Therefore several groups (us among them) started Geant4 simulation of cosmic muons in the pit to find their hit rate and distribution. Our results were presented to the collaboration on several meetings [61–67] and were highly appreciated because they confirmed the results from the "official" large scale simulation.

Our results are included in the section 4.2.1 and show that that the rate of cosmic muons in Pixel Detector is about 0.8 Hz which is about 0.3 % of the muons which enters the Inner detector. Their angular distribution is heavily affected by the existence of access shafts through which comes most of the cosmic muons. The special text output which was produced by our simulation also showed that there will be plenty of tangent tracks, something the detector was not constructed for.

To find what we would be really able to get from the Pixel Detector in the pit, we digitized the simulated hits and ran the standard Athena cosmic reconstruction algorithm on them. The results from the complete software chain are presented in section 4.2.2.

Carefully tuned dedicated cosmic reconstruction algorithm was able to find some cosmic tracks, but the efficiency was rather poor (about 10 % of cosmic tracks were successfully reconstructed), while the fake rate was quite high - about 10 % of all reconstructed tracks were fakes. This is caused by the unusual direction of cosmic tracks - they very rarely go close to the interaction point and they are tangent rather than perpendicular to the SCT and TRT modules.

The reconstruction of simulated Geant4 data shows what we should get from the detector in reality. We showed that although the ATLAS was not designed to measure cosmic rays, it is able to detect them. Moreover, the reconstruction algorithm was able to recover the overwhelming effect of access shafts on angular distribution that was observed in Geant4 simulation.

Our results suggest that it would take few hours to obtain hit in every module of the outermost Pixel layer and probably about a day to be sure we have at least one hit in all pixel barrel modules.

This means that if there would be enough time, the pixel modules could be tested using just cosmics to find noise pixel maps as was done during surface tests. While looking for noise pixel maps is at least theoretically possible, the alignment of pixel barrel by cosmic muons in the fashion of the surface tests will be impossible, at least before the first beam starts circulating in LHC.

To sum up, cosmic muons can be efficiently used to test pixel noise before the LHC will start operation. However, now we should find whether the cosmic muons can be used with sufficient efficiency during the beam period. Recent study [57] suggests that we can measure cosmic muons not only during LHC shutdowns, but also along the physics runs as there are several empty bunch crossings. This study is, however, only in the initial phase and will need input from real data taking to test its hypotheses.

Bibliography

[1] M. E. Peskin, D. V. Schroeder, *Introduction to quantum field theory*, Westview Press, 1995

[2] L. H. Ryder, *Quantum Field Theory*, 2nd edition, Cambridge University Press, 1996

[3] J. Hořejší, *Fundamentals of Electroweak Theory*, Karolinum Press, 2002

[4] J. Chýla, *Quarks, partons and Quantum Chromodynamics*, lecture notes, `http://www-hep2.fzu.cz/Theory/notes/text.pdf`

[5] Y. Dokshitzer, V. Khoze, A. Mueller and S. Troyan, *Basics of QCD*, Gif-sur-Yvette, France: Ed. Frontieres, 1991

[6] W.-M. Yao et al., Journal of Physics G 33, 1 (2006)

[7] F. Wilczek, *Beyond the Standard Model: An Answer and Twenty Questions*, hep-ph/9802400v1

[8] C. Q. Geng, R. E. Marshak, Phys. Rev. D 39, 693 (1989)

[9] J. A. Minahan, P. Ramond, and R. C. Warner, Phys. Rev. D 41, 715 (1990)

[10] Super-Kamiokande Collaboration, Phys. Rev. Lett. 81, 1562 (1998), hep-ex/9807003

[11] The LEP Collaborations, *A Combination of Preliminary Electroweak Measurements and Constraints on the Standard Model*, hep-ex/0612034v2

[12] H. Georgi, S. Glashow, Phys. Rev. Lett. 32, 438 (1974)

[13] H. Georgi, H. Quinn, S. Weinberg, Phys. Rev. Lett. 33, 451 (1974)

[14] G. Weiglein, *Supersymmetry*, lecture notes, `http://www.ippp.dur.ac.uk/~georg/ss/`

[15] M. Drees, *An Introduction to Supersymmetry*,hep-ph/9611409

[16] Phys. Rev. 159, 1251 - 1256 (1967)

[17] J. Wess and J. Bagger, *Supersymmetry and Supergravity*, Princeton Univ. Press, 1992

[18] F. A. Berezin, *The Method of Second Quantization*, New York, 1966

[19] S. Braibant, *SUSY searches at LEP*, hep-ex/0305058v1

[20] T. Mannel, lectures at CERN-JINR summer school 2007 in Třešť

[21] R. T. Klauber, *The Seesaw Mechanism*, `http://www.quantumfieldtheory.info/TheSeesawMechanism.htm`

[22] M. R. Buckley, H. Murayama, *How can we test seesaw experimentally?*, hep-ph/0606088v1

[23] O. Piguet, *Introduction to Supersymmetric Gauge Theories*, hep-th/9710095

[24] E. Gross, A. Klier, *Higgs Statistics for Pedestrians*, hep-ex/0211058.

[25] S. Brandt, *Statistical and Computational Methods in Data Analysis*, Springer, New York, 1998

[26] G. Cowan, *Lectures on Statictical Data Analysis*, `http://www.pp.rhul.ac.uk/~cowan/stat_course.html`

[27] ATLAS collaboration, *Effects of Misalignment on Flavour Tagging*, ATLAS note in preparation

[28] D. Rainwater, *Searching for the Higgs boson*, hep-ph/0702124v1

[29] J. Cammin, Ph.D. Thesis [ATLAS], BONN-IR-2004-06

[30] S. Asai et al., Eur. Phys. J. C 32S2, 19 (2004).

[31] Hardware commissioning coordinates, `http://hcc.web.cern.ch/hcc/`

[32] P. Jenni, *Introduction*, ATLAS week 7-11 April 2008, CERN, `http://indico.cern.ch/conferenceDisplay.py?confId=20537`

[33] `http://commons.wikimedia.org/wiki/Image:LHC_octants.png`

[34] CMS Outreach, `http://cmsinfo.cern.ch/`

[35] ALICE experiment: Panorama of ALICE, `http://aliceinfo.cern.ch/Public/panorama/`

[36] LHCb public pages, `http://lhcb-new.web.cern.ch/`

[37] LHC machine Outreach, `http://lhc-machine-outreach.web.cern.ch/lhc-machine-outreach/`

[38] ATLAS experiment public pages, `http://atlas.ch/`

[39] O. S. Brüning *et al.*, *LHC Design Report v.1*, CERN-2004-003-V-1,

[40] F. Wilczek, *Higgs Portal into Hidden Sectors*, talk given at CERN on May 31, 2007; `http://indico.cern.ch/conferenceDisplay.py?confId=a07117`

[41] ATLAS collaboration, *ATLAS Technical Proposal for a General-Purpose pp Experiment at the Large Hadron Collider at CERN*, 2nd edition, CERN, 1994

[42] ATLAS Computing Workbook, `https://twiki.cern.ch/twiki/bin/view/Atlas/WorkBook`

[43] Atlantis event display homepage, `http://www.hep.ucl.ac.uk/atlas/atlantis/`

[44] The LXR Cross-Referencer, `http://alxr.usatlas.bnl.gov/lxr/source`

[45] ATLAS Twiki homepage, `https://twiki.cern.ch/twiki/bin/view/Atlas/`

[46] Static ATLAS Offline software pages, `http://atlas-computing.web.cern.ch/atlas-computing/computing.php`

[47] Athena code Doxygen documentation, `https://twiki.cern.ch/twiki/bin/view/Atlas/DoxygenDocumentation`

[48] CERN hypernews, `https://hypernews.cern.ch/`

[49] ROOT framework homepage, `http://root.cern.ch/`

[50] Web interface to ATLAS offline software repository ViewCVS, `http://atlas-sw.cern.ch/cgi-bin/viewcvs-atlas.cgi/offline/`

[51] R. Moles, *Alignment using Cosmic Ray Data from the M6*, talk on 2nd ID workshop in Ringberg, 16/4/08, `http://indico.cern.ch/contributionDisplay.py?contribId=28&sessionId=5&confId=23706`

[52] ATLAS collaboration, *Pixel Offline Analysis for EndcapA Cosmic Data*, ATL-INDET-PUB-2008-003

[53] V. Kartvelishvili, *Low p_T ID monitoring wirh J/ψ and υ*, talk on 2nd ID workshop in Ringberg, 17/4/08, `http://indico.cern.ch/contributionDisplay.py?contribId=7&sessionId=8&confId=23706`

[54] M.Boonekamp et al., *Cosmic Ray, Beam-Halo and Beam-Gas Rate Studies for ATLAS Commissioning*, ATL-GEN-2004-001

[55] LHC commissioning web page, `http://lhc-commissioning.web.cern.ch/lhc-commissioning/`

[56] J. Schieck, *Alignment using tracks from off-IP interactions and beam-gas events*, 2nd Ringberg ID workshop 18/04/2008, `http://indico.cern.ch/materialDisplay.py?contribId=27&sessionId=5&materialId=slides&confId=23706`

[57] T. Loddenkötter, *Taking cosmic muons for ID alignment during physics runs*, 2nd Ringberg ID workshop, `http://indico.cern.ch/contributionDisplay.py?contribId=26&sessionId=5&confId=23706`

[58] Allkofer et al, Phys. Lett. 36B (1971), 425

[59] ATLAS detector simulation, online manual, `http://atlas-computing.web.cern.ch/atlas-computing/packages/simulation/geant4/geant4.html`

[60] ATLAS Geometry Tags, `https://twiki.cern.ch/twiki/bin/view/Atlas/AtlasGeomDBTags`

[61] P. Jež, *Towards cosmics with the Pixel Detector in the ATLAS cavern*, Pixel Offline Software Meeting, June 04, 2007, `http://indico.cern.ch/conferenceDisplay.py?confId=16452`

[62] P. Jež, *Cosmics*, Pixel Offline Software Meeting, June 18, 2007, `http://indico.cern.ch/conferenceDisplay.py?confId=17691`

[63] P. Jež, M. Marčišovský, *Calculation of the cosmic muon rate going through the Pixel Detector in the pit*, Pixel Offline Software Meeting, July 30, 2007, `http://indico.cern.ch/conferenceDisplay.py?confId=19451`

[64] P. Jež, M. Marčišovský, *Cosmic muon rate through Pixel Detector and muon distributions in the pit*, Pixel Offline Software Meeting, August 13, 2007, `http://indico.cern.ch/conferenceDisplay.py?confId=19596`

[65] M. Zeman, *Commissioning activities*, Pixel Offline Software Meeting, August 27, 2007, `http://indico.cern.ch/conferenceDisplay.py?confId=20224`

[66] P. Jež, *Cosmics rate in the pit*, ID week, October 2, 2007, `http://indico.cern.ch/sessionDisplay.py?sessionId=14&confId=9663`

[67] P. Jež, *Pixel cosmic rate studies*, ID week, October 4, 2007, `http://indico.cern.ch/sessionDisplay.py?sessionId=1&confId=9663`